Deepest Serendipitous Survey of the Intermediate Galactic Latitude from XMM-Newton

By

Larkin Michelle Duelge

A Thesis Submitted to
Saint Mary's University, Halifax, Nova Scotia
in Partial Fulfillment of the Requirements for
the Degree of Masters of Science in Astronomy

3 August 2011, Halifax, Nova Scotia

Approved: Dr. Luigi Gallo
Supervisor

Approved: Dr. Ian Short
Examiner

Approved: Dr. Robert Deupree
Examiner

Date: 23 August 2011

Your file Votre référence
ISBN: 978-0-494-80943-3
Our file Notre référence
ISBN: 978-0-494-80943-3

Contents

List of Figures

List of Tables

Acknowledgments

First, thank you to Dr. Luigi Gallo for the guidance and patience. Thank you also to Dr. Robert Dupree and Dr. Ian Short for participating in the committee. A special thank you to Florence and Elfrie for their friendship and secretarial expertise. Thank you to all the Astronomy and Physics Department.

To Jason, Diego, Jon, Fernando, Anneya, Andy, Kathleen, Dave, Chris, Mike, Michael, Fernando, and Dan for bring and accepting me into the department. Thank you to James, Pascal, and Liz for your friendship and help in both work and play.

Thank you to my parents, Dixie and Denny. Their support through this long educational journey has been needed and appreciated.

Abstract

Deepest Serendipitous Survey of the Intermediate Galactic Latitude from XMM-Newton

By Larkin Michelle Duelge

The *XMM-Newton Observatory* has conducted many observations of the type I active galactic nucleus 1H0707-495. The 0.7 deg^2 field of view around the AGN was observed over the course of $\sim$10 years with a total exposure time of 3.75 Ms, allowing for the deepest ever serendipitous survey of intermediate galactic latitude. Combined data from the *European Photon Imaging Camera (EPIC)* gives the first X-ray "real-colour" image of this field with a limiting flux of 6.72×10^{-16}, 2.94×10^{-15}, and 1.14×10^{-14} ergs/cm^2/sec in the 0.5-2, 2-4.5, and 4.5-12 keV, respectively. A total of 128 sources were detected with a photon count ≥ 50 not including one arcmin surrounding 1H0707-495. The log(N)-log(S) relation in two bands show consistent slopes with previous surveys and models. Spectra are created and analyzed for the 30 brightest sources and an additional source of interest. Colour-colour diagrams were made using hardness ratios to examine the nature of sources that were too dim to study spectroscopically.

23 August 2011

Chapter 1

Introduction

1.1 X-rays, the Cosmic X-ray Background, and AGN

X-rays cover the 0.1 to 500 keV range of the electromagnetic spectrum. X-ray radiation is emitted from astronomical objects containing extremely hot gas and/or very high-energy particles moving at relativistic speeds. Several astronomical objects emit X-rays such as galaxy clusters, supernova remnants, active galactic nuclei (AGN), and compact binary systems containing a white dwarf, neutron star, or black hole. The terms "soft X-ray" and "hard X-ray" are used to describe the penetrating ability and are relative terms that change depending on the context being used. For this work, "soft" will be from 0.5-2 keV and "hard" will be from 2-12 keV.

The cosmic X-ray background (CXRB) was discovered by Giacconi et al. (1962) during a rocket flight to observe X-rays from the moon. Giacconi found diffuse and constant X-ray emissions coming from all directions that were not attributed to the observing instrument. Two options for the origin of this CXRB were proposed. It was either a superposition of many discrete sources (Setti & Woltjer, 1973) or it was an optically thin, hot intergalactic medium (Marshall et al., 1980). Since then, surveys performed on the CXRB have found it to be the former, a superposition of many point sources. Optical spectroscopy identified the majority of these sources to be AGN (McHardy et al., 1998; Schmidt et al., 1998; Zamorani et al., 1999).

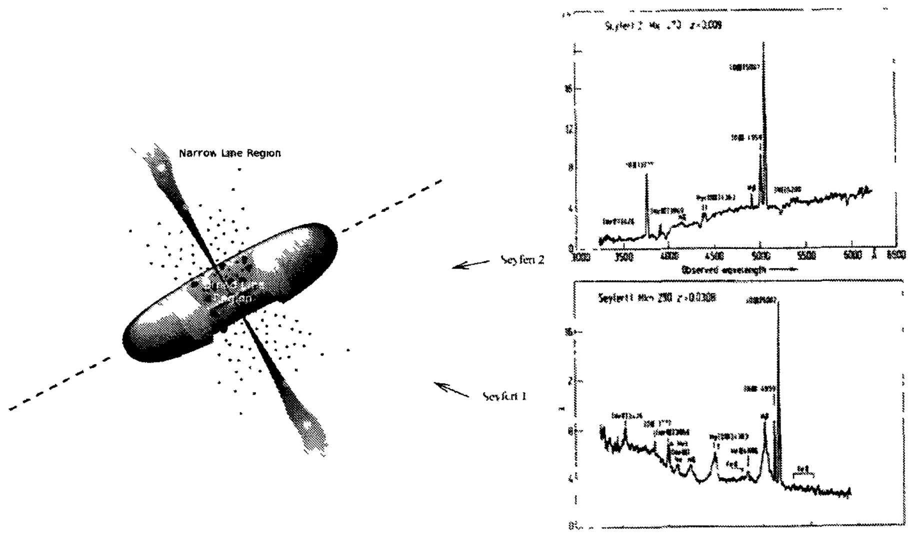

Figure 1.1: Left: The Unification Model showing the viewing angles of the type I and type II Seyfert galaxies (Torres & Anchordoqui, 2004). Right: Spectra of a type II AGN (top) and a type I AGN (bottom) (Netzer, 1990). The horizontal axis for both spectra are the same.

AGN have been broken down into groups: Seyfert galaxies, quasars, radio galaxies, blazars, and low-ionization nuclear-emission-line regions (LINERS) (Melia, 2009). Each of those groups can again be subdivided but the majority of this work will be concentrated on Seyfert type I and type II galaxies. The AGN Unification Model (Antonucci & Miller, 1985; Antonucci, 1993) is the theory suggesting both type I and type II Seyfert galaxies are the same object viewed from different orientations. Fig 1.1 on the right shows how the viewing angle is proposed to change from a type I to a type II AGN. The narrow line region (NLR) and broad line region (BLR) are named for the shape of the emission lines each region contributes to the optical spectra. In a type II AGN, a dusty torus hides the BLR from view leaving only the NLR represented in the spectrum (Fig 1.1 top). In a type I AGN, the NLR *and* BLR are visible and therefore both contribute to the spectrum (Fig 1.1 bottom). The X-ray continuum of an AGN spectrum follows a power law of the form $F_\nu = \nu^{-\Gamma}$ where Γ is referred to as the photon index.

1.2 Deep vs Wide Surveys

Extragalactic surveys have been useful tools for finding information about the formation and evolution of galaxies, clusters/groups of galaxies, large-scale structures, and supermassive black holes (Brandt & Hasinger, 2005). The deeper the survey, the fainter and more distant the objects detected. These objects represent earlier epochs and can be used to probe galaxy structure and formation. Deep surveys are important to study the populations of X-ray sources at the faintest levels possible and help constrain the faint-end population distribution of the CXRB. Such studies have resulted in the measurements of AGN evolution, growth of super massive black holes, constrained the physics of high-redshift AGN, performed populations counts of AGN, and improved understanding of the AGN content of galaxies (Brandt & Hasinger, 2005). On the other hand, wide surveys (Caccianiga et al., 2008; Hasinger et al., 2007) cover a much larger area and have much higher counting statistics in order to perform detailed analysis on a larger number of X-ray sources. However, wide surveys are typically shallow and are unable to represent the faintest X-ray sources that represent the majority of the CXRB.

Using the observations from surveys, models of the CXRB can be synthesized. These models have many possible parameters and therefore many models have been proposed. Some models are based on the unification theory of AGN, luminosity functions, and cosmological evolution (Comastri et al., 1995) while others use source counts, redshift distributions, absorptions distributions, and the geometry of the Universe (Gilli et al., 2001). These are only a few of the parameters that can be taken into account when modeling the CXRB.

1.3 Remaining Questions

There are questions that can still be answered with further X-ray surveys, particularly from deep surveys.

The CXRB is resolved at ≈80-95% below 6 keV, but drops to ≈60% at higher energies (Brandt, 2007) suggesting many high energy X-ray sources are still being missed. Selection incompleteness has limited our understanding of AGN and increasing the number of faint sources studied will allow a better population sample. An example of the limitations caused by incompleteness demonstrated by Hasinger et al. (2005) who showed that moderate-luminosity AGN peak later in cosmic evolution than high-luminosity AGN, contrary to initial intuition. Additional deep surveys can confirm or deny this unexpected result in the number density of AGN.

How much each source contributes to the CXRB needs to be further constrained. This can help to form models to find the origin of the CXRB (Comastri et al., 1995). Within these models there are parameters that can help describe many important properties of the Universe; the make-up of the CXRB, AGN formation/evolution rate, galaxy evolution through time, and the cosmological evolution of the universe.

The evolution of the spectral energy distribution of AGN requires further investigation. The evolution of AGN with high redshift and luminosity can only be studied with deep observations. These are just a few examples of the questions that can be answered with additional deep observations and multi-wavelength data.

1.4 Focus of This Work

1H0707-495

The type I AGN 1H0707-495 has been given substantial time by high-energy astronomers in the past because of its spectral complexity. 1H0707-495 is a popular target for X-ray observations because of the high variability and broad iron K and L emission lines (Fabian et al., 2009a). Although different models have been made to explain the properties of 1H0707-495, most fail to explain all features (Zoghbi et al., 2010). In total, over 3.75 Ms (1.25 Ms_{pn} + 1.25 Ms_{MOS1} + 1.25 Ms_{MOS2}) of exposure time has been taken with *XMM-Newton* in order to study this complex AGN. As a result, the field around 1H0707-495 is one of the deepest fields available from *XMM-Newton*. Substantial information can be taken from this existing data to analyze faint X-ray sources surrounding this AGN.

Our Work

Some of the deepest surveys performed, such as *Chandra Deep Field South* (Giacconi et al., 2001; Rosati et al., 2002; Giacconi et al., 2002), *Chandra Deep Field North* (Giacconi et al., 2002; Brandt et al., 2001), and *The XMM Lockman Hole* survey (Hasinger et al., 2001), encompass only high galactic latitude regions ($|b| \geq 27°$). Other surveys, such as those performed by *ROSAT* (Motch et al., 1998; Morley et al., 2001), include only the galactic plane. That makes this serendipitous survey important in order to collect data from a mixture of source types with low flux limits at intermediate galactic latitude ($|b| \simeq 17°$) in a wide range of energy bands. These energy bands allow both hard energy and soft energy sources to be sampled.

The focus of this thesis will be to locate and identify the X-ray sources of the deep field circumambient 1H0707-495. This thesis will present a X-ray survey of 128 sources over 0.7 deg^2 field of view, excluding one arcmin containing the AGN 1H0707-495. Chapter 2 will discuss the *XMM-Newton Observatory* and the specifications of the instruments. Chapter 3 will give details in extracting and reducing the data as well as the formulas used in the processing. Chapter 4 will give the source count distribution and the log(N)-log(S) relation. Spectra will be analyzed in chapter 5 using four models in identification of the brightest 30 sources and one additional source of interest. Chapter 6 will give the hardness ratios of each source displayed with a model webbing of absorbed power laws. In chapter 7 we will summarize our results and discuss avenues for future work.

Chapter 2

The XMM-Newton Observatory

2.1 Overview

The X-ray Spectroscopy Multi-Mirror Mission (XMM) is three 58 shell, Wolter-I telescopes built by the European Space Agency (ESA). It was launched in December of 1999 to perform high throughput spectroscopy of cosmic X-ray sources over a broad band of energies from 0.1-15 keV (Jansen et al., 2001). At the focal plane of the three nested X-ray Mirror Modules are the two Reflection Grating Spectrometer (RGS) readout cameras and an European Photon Imaging Camera (EPIC) with one pn semi-conductor detector and two metal-oxide semi-conductors (MOS) imaging detectors. Also included on the observatory are the Optical Monitor (OM) instrument and star trackers (Jansen et al., 2001). Fig 2.1[1] shows the configuration for *XMM-Newton.*

2.2 European Photon Imaging Camera (EPIC)

For this survey, the primary detectors used were the EPIC image detectors equipped with one pn and two MOS cameras. These cameras perform sensitive imaging observations over a 30 arcmin field of view (FOV) for energy ranges from 0.15 to 15 keV with a moderate spectral resolution ($E/\Delta E \sim 20 - 50$) and an angular resolution full width half maximum (FWHM) of six arcsec. The performance of the telescopes is based on how effective the mirrors are in collecting photons of different energies.

[1] http://heasarc.nasa.gov/docs/xmm/about_overview.html

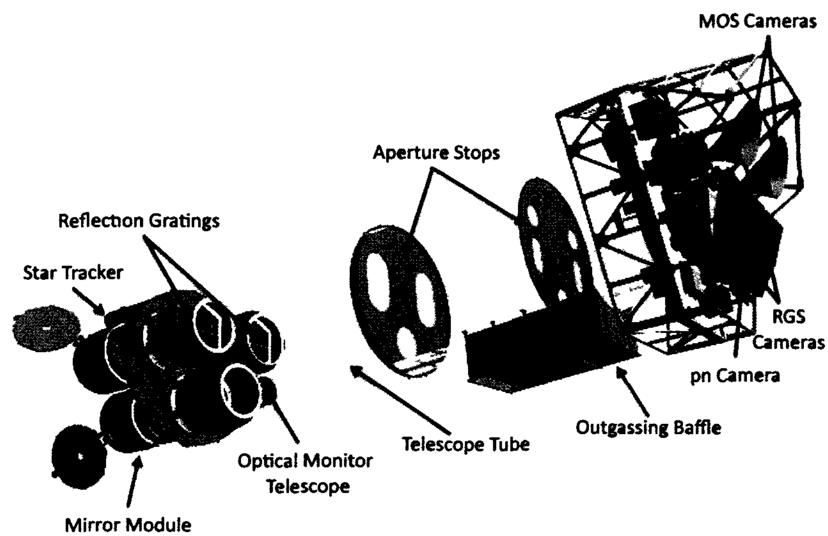

Figure 2.1: *XMM-Newton* observatory system

This is the effective area of the cameras and can be seen in Fig 2.2. As of 2008, *XMM-Newton* has not shown any important long-term change in the behaviour of the background from the EPIC cameras (Rodríguez-Pascual & González-Riestra, 2008).

2.2.1 pn Camera

The pn-CCD is named for the pn junction of the semiconductors used in the configuration of the camera. The angular resolution of the telescope in front of the pn camera is 15 arcsec (0.004 deg) half energy width (HEW) between 1.5 and 8 keV. The pixel size is 4.1 arcsec (.001 deg) with a position resolution of 120 μm giving angular resolving capability of 3.3 arcsec (9.17×10^{-4} deg)(Strüder et al., 2001).

There are four operating modes of the pn camera seen in Fig 2.4: full frame/extended full frame mode, large window mode, small window mode, and timing mode. The

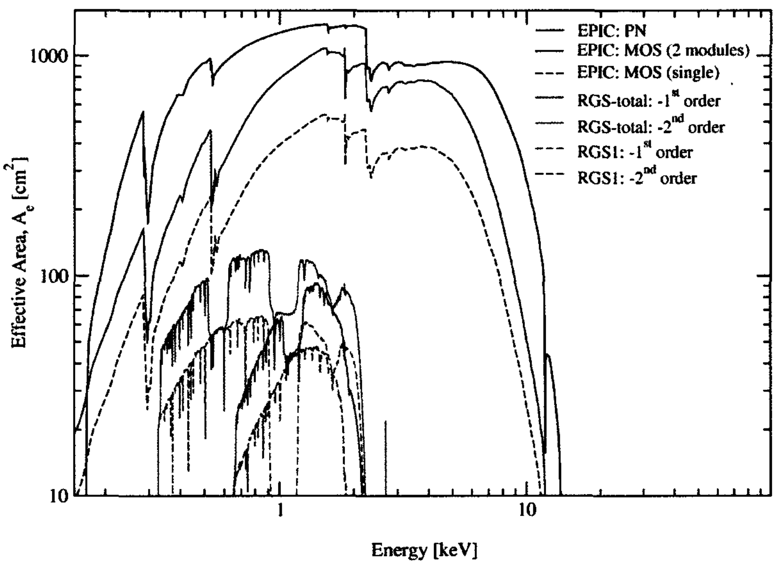

Figure 2.2: *XMM-Newton* EPIC and RGS net effective area (ESA: XMM-Newton SOC, 2010)

choice of observing mode is determined by finding the best way to maximize the FOV and camera "live-time" while minimizing the out-of-time event (OoT) and pile-up. An event is characterized by a photon hitting the detector and being read out. This gives the photons position on the detector, the energy, arrival time, shape (used to separate X-rays from particles such as cosmic rays), and the CCD number. An event list is the accumulation of many of these events. If an event is recorded during the time the CCD is readout, an OoT is created and will need to be taken into account. When more than one X-ray photon arrives in one camera pixel or in an adjacent pixel before a read out, there is pile-up. Full frame mode is best for the use of dim extended sources with a readout cycle taking 73.3 ms, 4.6 ms for reading out and 68.7 ms for the integration of the image. For brighter sources, the FOV is reduced to decrease the number of OoT events, to improve the time resolution, and to increase the pile-up limit. In the large window mode, only the inner half of the CCD is used for imaging, seen in Fig 2.4. The read out in large window mode is 720 ns per CCD line and the

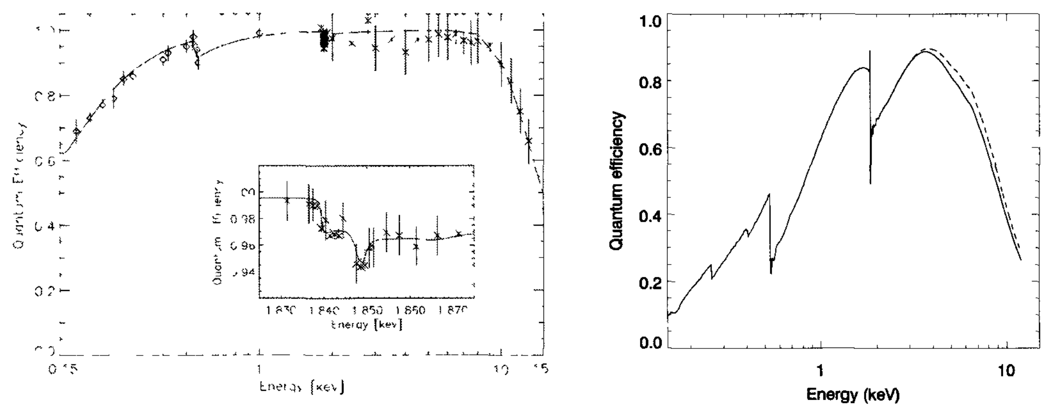

(a) (b)

Figure 2.3: **a)** Quantum Efficiency of the pn-CCD with fully depleted thickness of $300 \mu m$ (Strüder et al., 2001). **b)** Quantum Efficiency of the two MOS CCDs. MOS1 is the solid line while MOS2 is the dotted line. (ESA: XMM-Newton SOC, 2010)

time resolution is 47.7 ms, dropping the of OoT events to below 0.2%.

The quantum efficiency (QE) is the efficiency of the telescope's ability to collect light, is shown in Fig 2.3 (ESA: XMM-Newton SOC, 2010). Although efficient between 0.1-15 keV, the cameras are only reliably calibrated between 0.3-12 keV. In this work, data will only be considered between 0.3-12 keV unless otherwise specified.

2.2.2 Metal Oxide Semi-conductor Cameras (MOS)

The imaging area for the MOS camera is $\sim$2.5 cm^2, so that a mosaic of seven CCDs cover the focal plane 62 mm or 28.4 arcmin in diameter. The imaging section has 600×600 pixel grid, each pixel covering 1.1×1.1 arcsec of the FOV (Turner et al., 2001).

The four modes available for the MOS cameras seen in Fig 2.4 are: large window mode, small window mode, timing mode, and full frame mode. Large window mode is 300 X 300 pixels with 0.9 s integration and small window mode is 100×100 pixels with 0.3 s integration time. Full frame mode requires a 0.2 s readout time. The overall cycle time of the MOS cameras is 2.6 s (Turner et al., 2001). The readout is split into two sections that can be used separately or together to half the readout time. The QE of the MOS cameras can be seen in Fig 2.3. The QE of the MOS chips limit the energy bandpass at the high end as opposed to the pn that has an efficiency up to 15 keV.

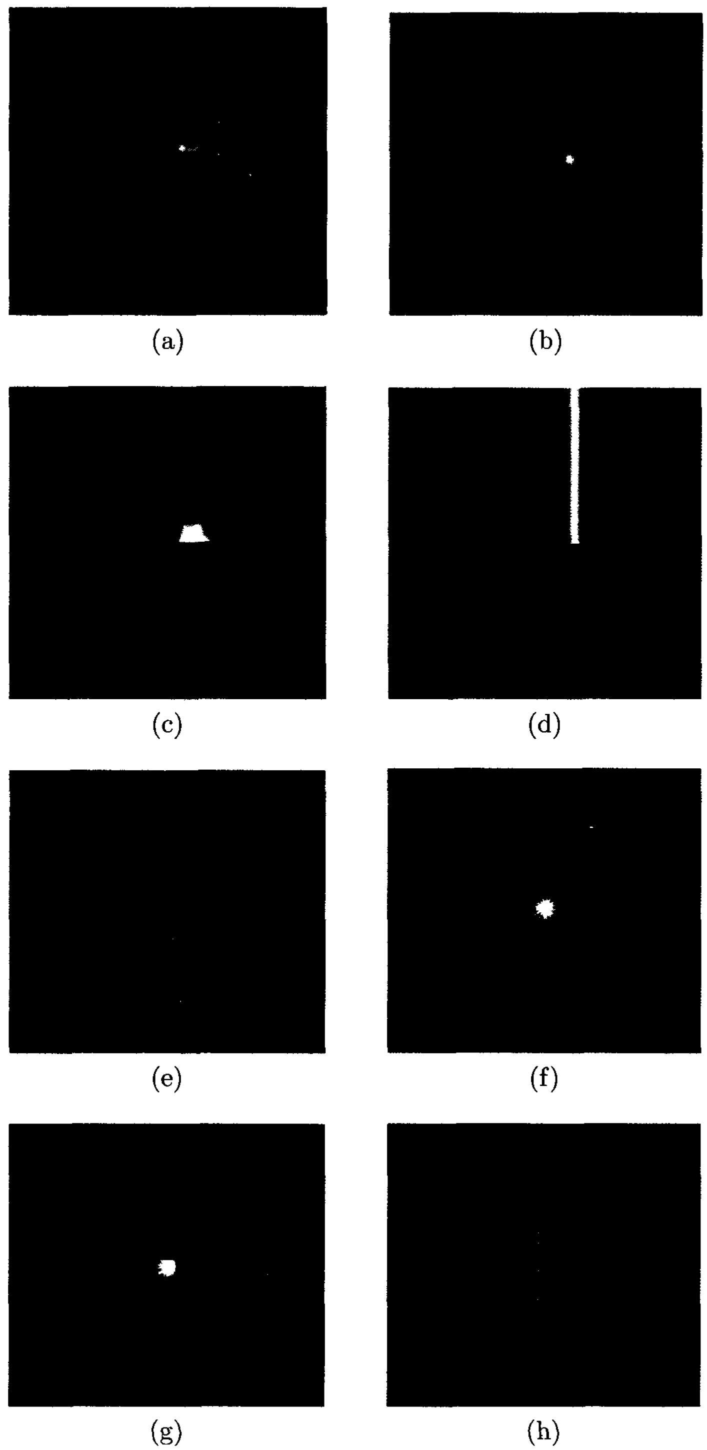

Figure 2.4: Operating mode of the pn camera in **a)** Full frame/extended full frame mode, **b)** Large window mode, **c)** Small window mode **d)** Timing mode(ESA: XMM-Newton SOC, 2010). Operating mode of the MOS camera: **e)** Full frame mode, **f)** Large window mode, **g)** Small window mode **h)** Timing mode.

Chapter 3

X-ray Observations & Data Reduction

3.1 Observations

The Narrow Line Seyfert Galaxy 1H0707-495 is centered at RA 7 h:8 m:41.0 s and Dec −49 h:33 m:6.0 s with galactic coordinates $\ell = 260.^{\circ}169$ and $b = -17.^{\circ}672$. *XMM-Newton* has made thirteen pointed observations during thirteen different revolutions (159, 521, 1360, 1361, 1387, 1491, 1492, 1493, 1494, 1971, 1972, 1973, 1974) from 21 October 2000 through 20 September 2010 for a net exposure of ~3.75 Ms (1.25 Ms_{pn} + 1.25 Ms_{MOS1} + 1.25 Ms_{MOS2}). A summary of the observations can be seen in Table 3.1. All but four of the observations were obtained from the *XMM-Newton Science Archive (XSA)*[1] through ESA. Observations from revolutions 1971 through 1974 were proprietary to N. Schartel who offered them with conditions. The medium filter was used for all EPIC cameras during all observations. The first two observations (revolution 159 and 521) were done with the pn camera in full window mode and the MOS cameras in large window mode. The remaining observations were done with the pn and MOS cameras in large window mode and small window mode, respectively.

[1]http://xmm.esac.esa.int/xsa/index.shtml

Revolution	Observation	Date		Time		Duration	Exposure: GTI		
	ID	Start	Stop	Start[UTC]	Stop[UTC]	[s]	pn [s]	MOS1[s]	MOS2[s]
159	110890201	2000-10-21	2000-10-21	01:27:57	12:46:20	46018	40703	43149	43148
521	148010301	2002-10-12	2002-10-12	11:33:30	09:14:18	79953	78048	79671	79673
1360	506200201	2007-05-16	2007-05-16	06:37:32	17:22:04	40910	38700	40611	40615
1361	506200301	2007-05-14	2007-05-14	02:48:37	13:33:07	40953	38670	40610	40613
1387	506200401	2007-07-06	2007-07-06	11:09:06	22:26:13	42866	40627	42564	42570
1491	511580101	2008-01-29	2008-01-31	18:57:12	04:43:44	123815	121592	123513	123516
1492	511580201	2008-01-31	2008-02-01	18:49:30	23:11:31	176235	102121	102038	102041
1493	511580301	2008-02-02	2008-02-04	20:19:16	01:15:58	122504	104202	94159	94153
1494	511580401	2008-02-04	2008-02-06	22:15:57	02:33:16	121922	101839	102939	102946
1971	653510301	2010-09-13	2010-09-14	01:01:21	08:39:47	116575	113906	114823	114832
1972	653510401	2010-09-15	2010-09-16	01:03:22	12:00:57	128200	125855	123689	123695
1973	653510501	2010-09-17	2010-09-18	01:05:51	09:36:36	127601	117045	118474	118485
1974	653510601	2010-09-19	2010-09-20	01:04:46	10:18:29	129001	119623	121067	121069

Table 3.1: Observing Log. The *XMM-Newton* revolution is given in column 1. Column 2 gives the observations ID. Column 3, 4, and 5 gives start and stop dates, times, and duration of each observation, receptively. Columns 6, 7, and 8 give the GTI exposure time of the pn, MOS1, and MOS2 cameras, respectively.

3.2 Data Reduction

XMM-Newton data was downloaded from the *XMM-Newton Science Archive (XSA)*[2] and processed with version 9.0 of *XMM-Newton Scientific Analysis System (SAS)*[3]. SAS is a collection of tasks, scripts, and libraries specifically designed to reduce and analyze data collected by the *XMM-Newton* observatory. HEASARC's FTOOLS[4] (Blackburn, 1995) routines were used to process Flexible Image Transport System (FITS) files. FTOOLS is a collection of utility programs to create, examine, or modify data files in this format. The SAS task `cifbuild` was used to build calibration index files (CIF) by scanning a list of directories of current calibration files (CCF) from ESA. To create new files containing additional information regarding instrumental housekeeping and calibration, the task `odfingest` was performed to create observation data files (ODF). Reprocessing was done to take full advantage of the latest developments of software and calibration. To do this, `epchain` was performed for each CCD on the pn camera and `emchain` was performed for each CCD on each of the two MOS cameras. A flow chart for the MOS processing is given in Fig 3.1. `Epchain` performed similar tasks as `emchain` for the pn CCD and is performed twice: once in standard mode and once for creating OoT event lists. The OoT events were then subtracted from the source event list. The results of OoT subtraction to a figure can be seen in Fig. 3.2.

[2]http://xmm.esac.esa.int/xsa/index.shtml
[3]http://xmm.esac.esa.int/sas
[4]http://heasarc.gsfc.nasa.gov/ftools/

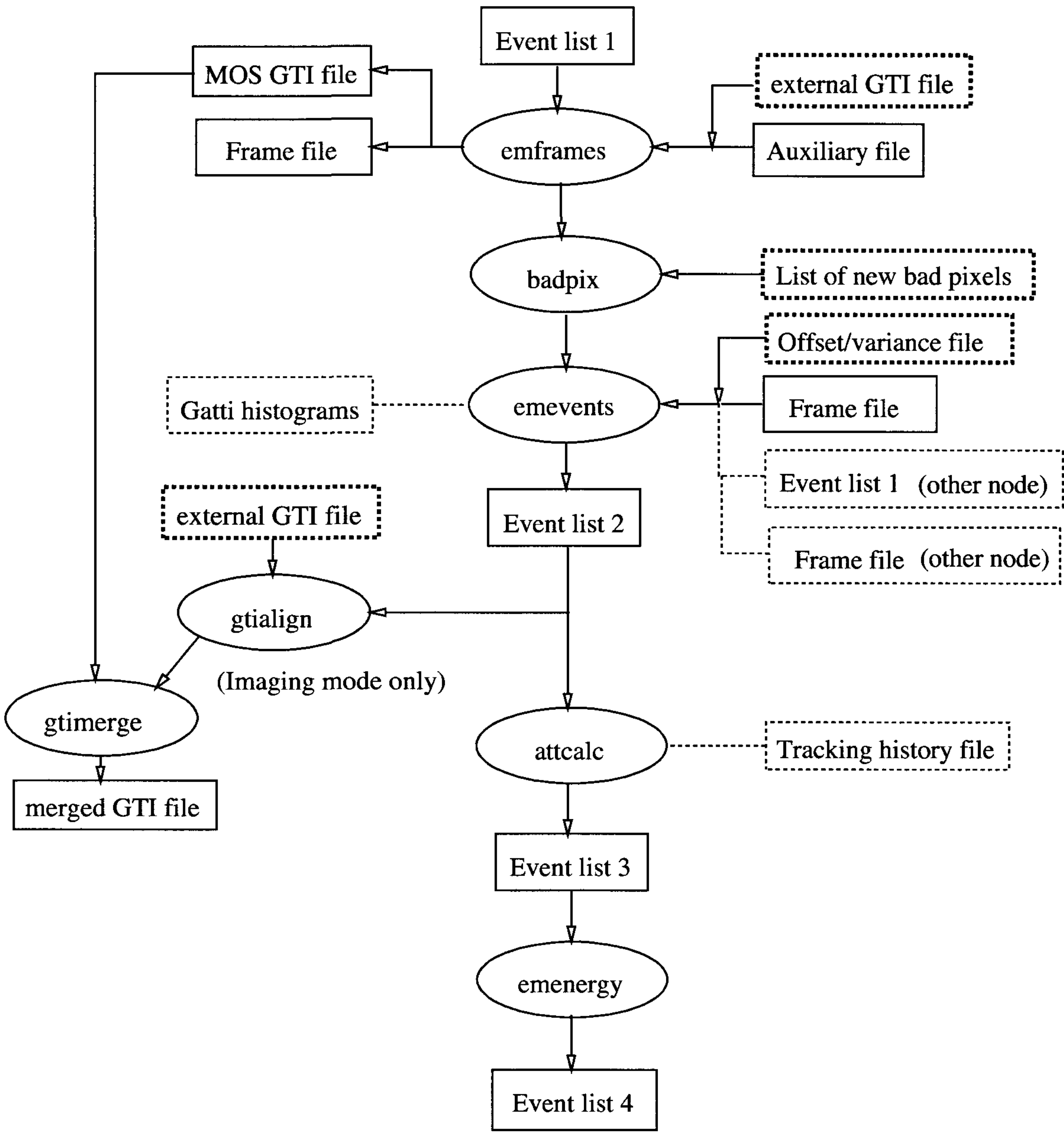

Figure 3.1: Organization of the EPIC MOS event list being combined. The files in boldly dashed boxes are used (or produced) if they exist. The files in simply dashed boxes are options of the individual tasks not used in the current chain. A similar routine occurs for the pn processing. (I. de la Calle, 2011)

(a) (b) (c)

Figure 3.2: **a)** Image with Out-of-Time event. **b)** Out-of-Time event. **c)** Cleaned image with Out-of-Time event removed.

Data were processed in the four energy bands 0.5-1, 1-2, 2-4.5, and 4.5-12 keV, through a pipeline processing described in chapter 3.3. Histograms of counts were made and energies greater than 12 keV were eliminated as background became dominant and reliable calibration is lost. A good time interval (GTI) is a time interval where an event list is collected and it is important in the calculation of exposure times or removing high particle background time periods. GTI are were made by filtering the high energy background to a threshold of 2 counts/armin^2/ks for the MOS and 10 counts/armin^2/ks for the pn cameras using `tabgtigen`. Event lists were made from the GTI using `evselect` that were then used to create images for all energy bands and cameras. Fig 3.3a and b show X-ray images of the pn camera and the combined MOS1 and MOS2 cameras, respectively, summed over all observations and energies. Bin size for the pn and MOS cameras was set to 4.1 arcsec and 1.1 arcsec, respectively for source detection. Finally all images were combined taking into account different energy bands. Fig 3.4 shows the X-ray "real-colour" image of the FOV. The standard convention of energy/colour was used: red from 0.5-2 keV, green from 2-4.5 keV, and blue from 4.5-12 keV.

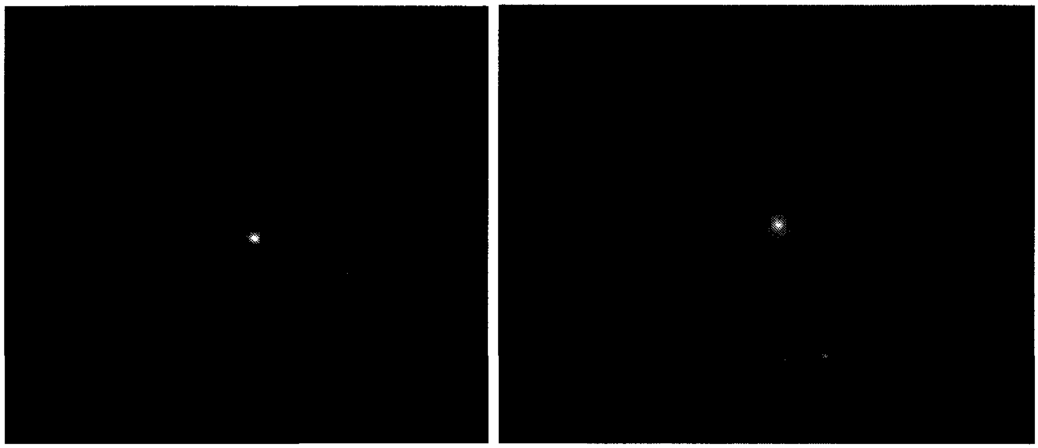

(a) (b)

Figure 3.3: **a)** Combined X-ray image from all observations for the pn cameras. **b)** Combined X-ray image from all observations for the MOS camera.

3.3 Source Detection

Source detection was used with the "*`edetect_chain` Work-Around*" in the energy bands 0.5-1, 1-2, 2-4.5, and 4.5-12 keV. This work around split up the meta task `edetect_chain` into its constituent parts so that additional parameters could be included. A common practice of creating a 2-10 keV band was not included because of the large energy range that may lead to inaccuracies in the estimates of QE, mirror vignetting, and FOV. Instead, the 2-4.5 and 4.5-12 keV final products were combined.

The corresponding exposure maps for each image were created using the task `eexmap` accounting for the latest calibration information on the mirror vignetting, QE, and filter transmission. Because of the serendipitous nature of the survey, not all areas of the field of view were equally sampled. The combined exposure map from all observations can be seen in Fig 3.5 and the difference in exposure in each area can be seen. The maps were then corrected for bad pixels, bad columns, and CCD gaps. Detection masks were created for the pn, MOS1, and MOS2 cameras with `emask` to define the area of each detector with exposure area at least 50% of the maximum

Figure 3.4: X-ray "real-colour" image of combined observations. The colour refers to different energy bands: red, green, and blue correspond to 0.5-2, 2-4.5, and 4.5-12 keV respectively. Smoothing is done using a 2 arcsec Gaussian kernel.

exposure.

The *SAS* command `eboxdetect` was performed on each camera/energy in *local mode* to construct a sliding box detection (5×5 pixels) creating a preliminary source list. Any detection with likelihood above eight was included in the preliminary list, as suggested by the XMM-Newton Handbook (2010). Likelihood is the likelihood that a source being detected is a spurious detection, $\mathcal{L} = -ln\, p$, where p is the probability of the detection occurring by chance. For a $\mathcal{L} = 8$, a $p = 3.35 \times 10^{-4}$. Detection likelihoods were then transformed into equivalent likelihoods ($\mathcal{L}_2$):

$$\mathcal{L}_2 = -ln(1 - P(\frac{\nu}{2}, \mathcal{L}')), \text{where } \mathcal{L}' = \sum_{i=1}^{n} \mathcal{L}_i$$

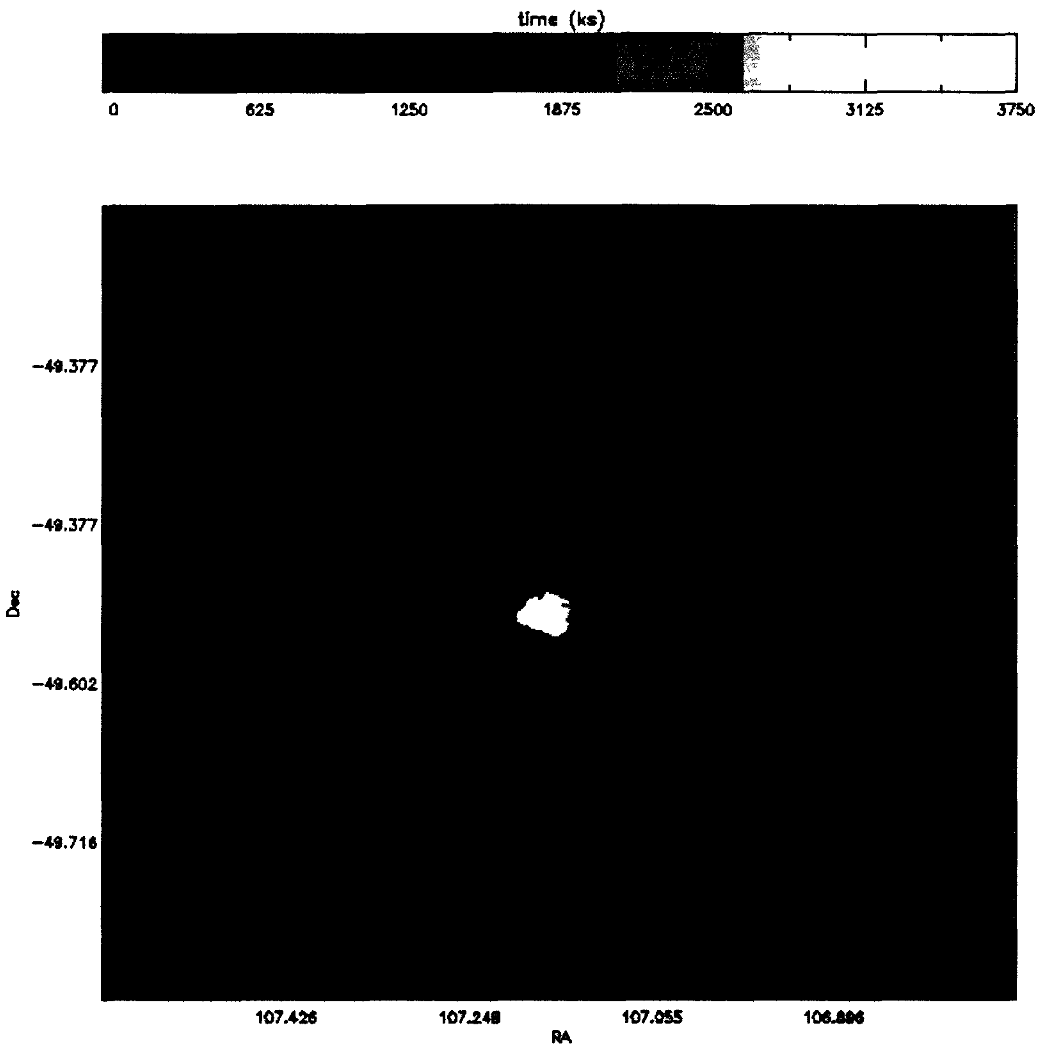

Figure 3.5: Colour coded vignetting corrected exposure map. The maximum effective depth is shown in white at 3.75 Ms. RA and Dec are in units of degrees.

where P is the incomplete Gamma function, n is the energy band, $\nu = 2 + n$, $\mathcal{L}_i = \frac{C_i}{2}$ with C defined by the *C statistic* used for binned data at low count rates. The *C statistic* was developed for a parameterization estimation where the probability need not be a Gaussian (Cash, 1979).

From the original image, the command `esplinemap` removed all preliminary sources found by `eboxdetect` to create a background map. Fig 3.6 is the 1-2 keV background map of observation 110890201 for the pn camera, thus any detected source from 1-2

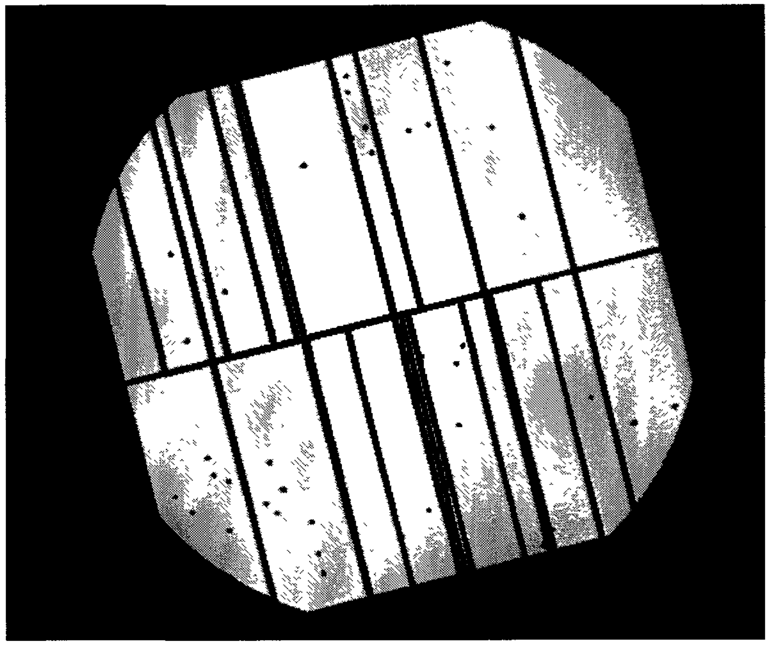

Figure 3.6: *Cheesed* background map made from `esplinemap` of observation 110890201 for the pn camera. All sources detected in this observation within the energy range of 1-2 keV have been eliminated.

keV has been removed from the image. This spline image has been termed a *cheesed* spline background map because of the Swiss cheese appearance from the removed sources. This *cheesed* background map is divided by the exposure map to remove spatial variations. Again `eboxdetect` was performed, this time in *map mode*, for each camera and energy taking into account the background map and made a final source detection list. The task `emldetect` used these sources and simultaneously applied a point spread functions (PSF) and Gaussian model of each source for all cameras/energies. This constrained the same best-fit value in all energy bands of each camera for each source. `Emldetect` used the exposure maps to correct the count rates for vignetting and losses because of inter-chip gaps, bad pixels, and OoT events. Source counts (S) and uncertainties (σ_S) are defined as:

$$S = \frac{counts_{img} - counts_{bkg}}{PSF}, \qquad \sigma_S = \frac{1 + \sqrt{counts_{img} + 0.75}}{PSF}$$

where $counts_{img}$ are the image and background counts and $counts_{bkg}$ are just the background counts. The count rate (CR) is then

$$CR = \frac{S}{T_{pn} + T_{MOS1} + T_{MOS2}}$$

where T_{pn} , T_{MOS1}, T_{MOS2} are the exposure times of the three instruments computed from the exposure maps. The count rate-to-flux energy conversion factors (ECF) are calculated using the latest response matrices assuming a power-law with an X-ray Galactic absorption $N_H = 3 \times 10^{20}\text{cm}^{-2}$ † and photon index $\Gamma = 1.7$. The Galactic absorption is because it is an observed flux from within our Galaxy and there is intergalactic extinction of X-rays due to absorption of the photons between the source and the observation. The reason for $\Gamma = 1.7$ will be explained in chapter 4.3. This model has been shown to provide a reasonable representation of the bulk of X-ray sources (Watson et al., 2009). The total conversion factor was computed using the overall exposure times of the pn, MOS1, and MOS2 cameras, ECF_{pn}, ECF_{MOS1}, ECF_{MOS2}.

$$\frac{T_{tot}}{ECF_{tot}} = \frac{T_{pn}}{ECF_{pn}} + \frac{T_{MOS1}}{ECF_{MOS1}} + \frac{T_{MOS2}}{ECF_{MOS2}},$$

where $T_{tot} = (T_{pn} + T_{MOS1} + T_{MOS2})$. The ECF for each instrument and energy band can be seen in Table 3.2. The source flux (F_X) is then calculated as

$$F_X = ECF \times CR.$$

Each source, the probability (p) that counts originate from a background fluctuation was calculated from the Poisson function:

†xmm.vilspa.esa.es/docs/documents/CAL-TN-0023-2-1.ps.gz

Camera	Energy [keV]	ECF $[10^{-11} counts\ cm^2/erg]^2$
pn-CCD	0.5-1	7.83782
	1-2	5.7827
	2-4.5	1.90529
	4.5-12	0.554529
MOS1	.5-1	1.82853
	1-2	2.01594
	2-4.5	0.737800
	4.5-12	0.143131
MOS2	.5-1	1.83088
	1-2	2.01594
	2-4.5	0.741687
	4.5-12	0.150560

Table 3.2: Energy Conversion Factor table for the medium filter

$$\sum_{n=counts_{img}}^{\infty} e^{-counts_{bkg}} \frac{counts_{bkg}}{n!} > p$$

Using $count_{img} = 50$ and $count_{bkg} = 6.5$, a $p = 2 \times 10^{-4}$ was calculated. A sensitivity map providing a point source detection upper limit for each image pixel was created using `esensmap` for each camera/energy and combined to create a single sensitivity map. Images were combined using `emosaic`.

For a source to be included in the final source list, it had to be detected by two or more cameras from any of the observations. Source counts have been weighted by exposure times. The order of brightness was determined by taking the highest weighted source count from each source. The AGN 1H0707-495 and the surrounding one arcmin were removed because of contamination and source confusion from the bright AGN. While this did not remove all light from the AGN, it removed enough so that a source could be detected within the threshold. The final source list can be seen in A.1. According to SIMBAD Astronomical Database[¶] two possible sources could have been identified prior to this survey. Sources 13 and 128 each had one identified object in the database within 0.01 deg. The separation needed for *XMM-Newton* to resolve between two sources is 0.0055 deg. I used a high estimate of 0.01 degrees to take into account the angular resolution of the observatory with the fact the right ascension and declination of the sources will not be exact between my values and catalogue's. Source 13 has been listed as or close to a galaxy in the *6-degree Field Galaxy Survey* and *2Micron ALl-Sky Survey, Extended source catalogue.* Source 128 has been listed to be or be close by to a radio source in the *Parkes-MIT-NRAO, Molonglo Catalog (Radio)*, and the *Sydney University Molonglo Sky Survey.* No X-ray sources were previously identified.

[¶]SIMBAD database operated at CDS

Chapter 4

Discrete Source Contribution to the CXRB

It has been shown that the CXRB originates from the superposition of many unresolved, faint X-ray sources (McHardy et al., 1998; Schmidt et al., 1998; Zamorani et al., 1999). Spectroscopic analysis has shown the predominant objects to be AGN (as will be seen in chapter 5), the highest fraction consisting of type II Seyfert (i.e. absorbed) followed by type I Seyfert galaxies (i.e. unabsorbed)(Brandt, 2007). To estimate the contribution of each extragalactic X-ray source to the CXRB, it is necessary to estimate each source's "luminosity function" and extrapolate to larger distances. One means of evaluating the contribution of each source to the CXRB is the "log(N)-log(S)" analysis.

4.1 Sky Coverage

Taking all source fluxes and distributing them evenly over the 0.7 deg^2 FOV, Fig 4.1 shows the distribution of the fluxes with a solid angle starting at 0.0 deg^2 and increasing to the full FOV. Soft sources (red solid line) have the majority of fluxes and have a higher detection threshold, while hard source (blue dotted line) are much less in number and have a lower detection threshold. The sky coverage was computed using the sensitivity maps at a given flux. The area of the sky where the sensitivity maps have values below a specified flux is summed. For each band, a sky area at

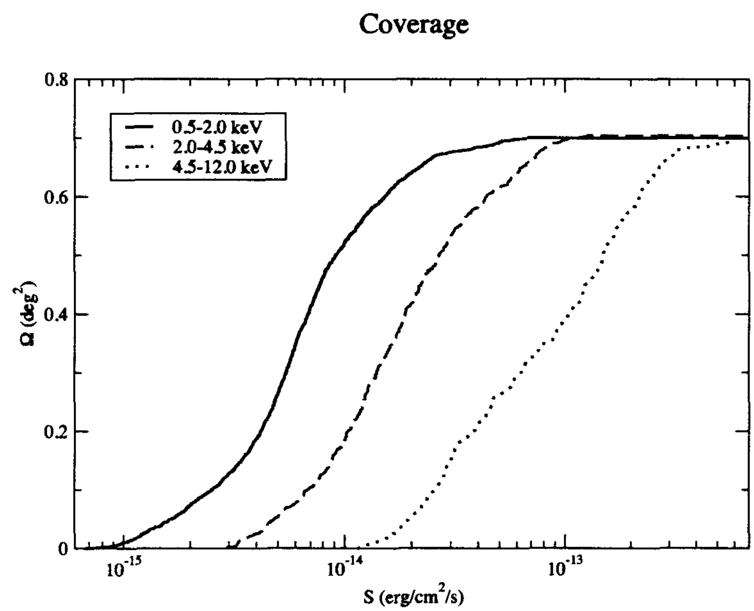

Figure 4.1: Sky coverage as a function of flux for energies 0.5-2 (red solid line), 2-4.5 (green dashed line), and 4.5-12 (blue dotted line) keV

each flux was calculated. The sky coverage in the 0.5-2, 2-4.5, and 4.5-12 keV energy ranges were computed by summing the contribution from all fields following Baldi et al. (2002).

4.2 Calculating Source Count Distributions

In X-ray astronomy it is customary to use the integral source counts to show the shape of the source count distribution. The number of sources per unit sky area with a flux higher than a predetermined minimum flux is defined as

$$N(>S) = \sum_{S_i > S} \frac{1}{\Omega_i},$$

where $N(>S)$ is the surface number density of sources with a flux (S) higher than a minimum flux (S_i) of the i^{th} source, and Ω_i is the solid angle in deg^2 as calculated by the sky coverage (Fig 4.1). The minimum threshold for the flux detected for each energy band was 6.72×10^{-16}, 2.94×10^{-15}, and 1.14×10^{-14} ergs/cm^2/sec in the 0.5-2, 2-4.5, and 4.5-12 keV respectively. In the remainder of this chapter, the 2-4.5 and 4.5-12 keV bands will be combined. The variance of the source number counts is then

$$\sigma^2 = \sum_{S_i > S} \left(\frac{1}{\Omega_i}\right)^2 .$$

4.3 log(N)-log(S)

Extragalactic count distributions are dependent on the cosmological and statistical properties of X-ray sources and provide a direct method to investigate the underlying source population. By constraining the extragalactic source count distributions over a range of fluxes and energy bands, one can test if the predictions of synthesis models of the CXRB agree with the observed constraints provided by X-ray surveys (Mateos et al., 2008). Within these models, there are parameters that can help describe what the CXRB is composed of and why it follows the trend it does. These models also can include many important properties of the Universe. Observations and models differ for the soft energy and the hard energy sources.

The cumulative log(N)-log(S) for the soft energy band of 0.5 - 2 keV can be seen in Fig 4.2. The red diamonds are *XMM-Newton Large scale survey* (Mateos et al., 2008), the green squares are the *XMM-COSMOS field* (Cappelluti et al., 2007), and the purple flags are the *XMM-Newton middle latitude serendipitous survey* (Novara et al., 2006). The two solid lines are from Baldi et al. (2002) for log(N)-log(S) for higher galactic latitudes ($|b| > 27°$). Included are the upper and lower limits of the log(N)-log(S) using the Poisson's formula discussed in chapter 3. The default $p = 2 \times 10^{-4}$ was used for the upper limit and $p = 2 \times 10^{-5}$ with a larger extraction radius was used for the lower limit accounting for any systematic errors in the *XMM-Newton* calibrations. The dashed blue line in Fig 4.2 - 4.3 is the predicted model of the contribution of AGN to the X-ray background (Comastri et al., 1995). This model is based on the unification schemes of AGN and its related X-ray spectral properties. This model predicts the distribution based on the possible reprocessing of X-ray radiation by cold matter now called the "reflection mode" (Comastri et al., 1995).

Fig 4.2a shows data with the converted count rate to flux using a photon index of $\Gamma = 1.7$. This led to a power law index of -2.74 ± 0.16 compared to Mateos' -1.29 ± 0.04 and Cappelluti's -1.16 ± 0.04 who used a photon index of $\Gamma = 2.0$. The 2-10 keV band has been studied vigorously in the past 30 years and it has been found that most AGN spectra follow a the power law with $\sim \Gamma = 1.7$. This is because of the photons from the accretion disc undergoing Comptonization in the hot corona (Nardini et al., 2011). In the mid-1980s, observations using the Einstein Imaging Proportional Counter (IPC) showed X-rays from 0.1-2 keV followed a much steeper index (Pravdo & Marshall, 1984; Elvis et al., 1985). This steepening between the soft and hard X-rays is called the "soft excess". Over the years, it was found that reflection from the photo-ionized accretion disc being blurred by relativistic effects successfully reproduce the spectral shape of the soft excess (Nardini et al., 2011). When we apply the higher photon index in the lower energy bands to the data, we find the slopes are comparable with a power law index $= -1.37 \pm 0.08$ as seen in Fig 4.2b.

My data lie close to Novara et al. (2006) middle latitude survey and above the predicted values. Novara et al. (2009) reason for the data above the upper limit set by Baldi et al. (2002) is that their survey detected a large sample of galactic

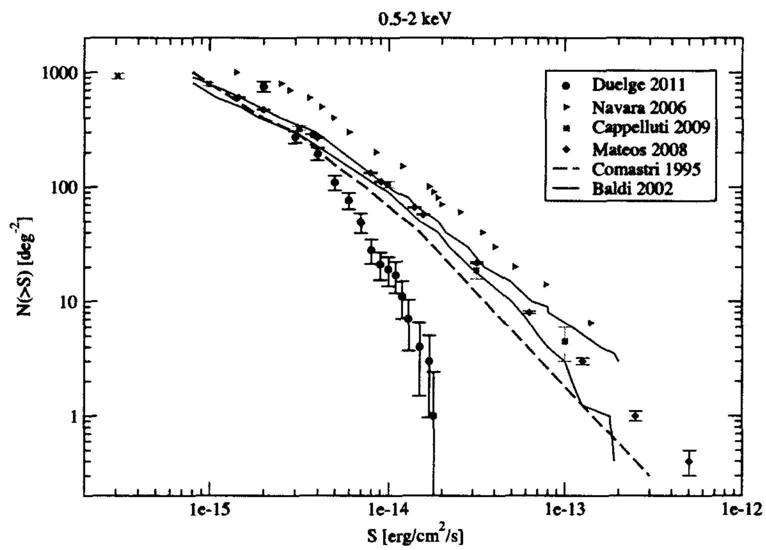

(a)

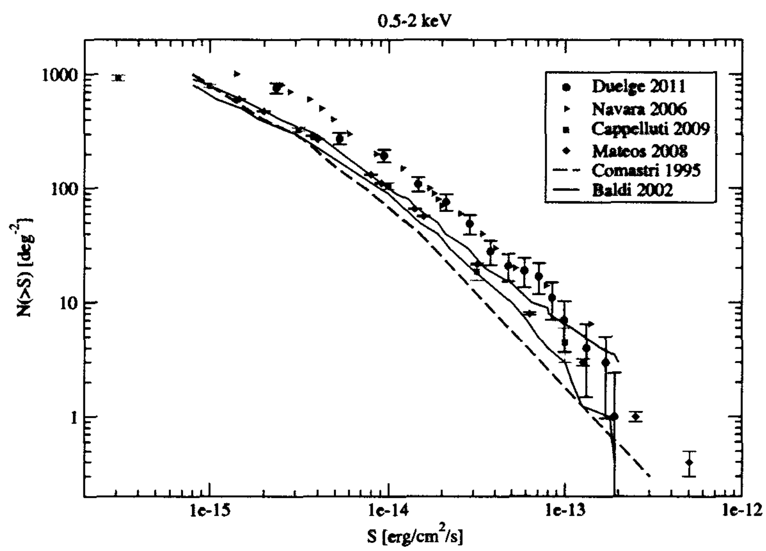

(b)

Figure 4.2: **a)** The 0.5-2 keV log(N)-log(S) of this serendipitous survey (black circles) as compared to *XMM-Newton Large scale survey* (Mateos et al. 2008, red diamonds), the XMM-COSMOS (Cappelluti et al. 2007, green squares), and the *XMM-Newton* middle-latitude serendipitous survey (Novara et al. 2006, purple flags). The dashed blue line represents the model by Comastri et al. (1995). The slope is much steeper than the comparisons because of using the default photon index $\Gamma = 1.7$. **b)** The slope compared once we changed the photon index $\Gamma = 2$ for the soft excess to compare results.

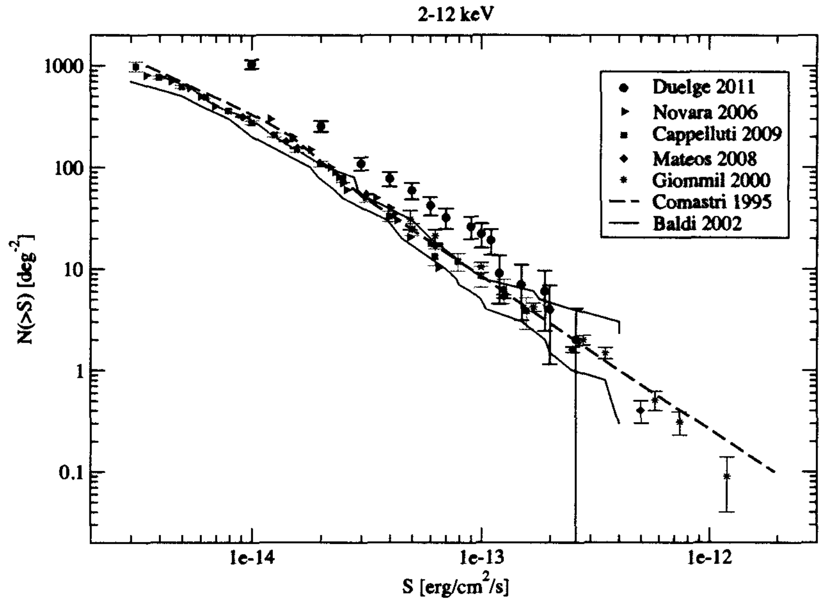

Figure 4.3: The 2-12 keV log(N)-log(S) of my serendipitous survey (black circles) as compared to *XMM-Newton Large Scale survey* (Mateos et al. 2008, red diamonds), the XMM-COSMOS (Cappelluti et al. 2007, green squares), the *XMM-Newton* Middle-Latitude Serendipitous survey (Novara et al. 2006, purple flags), and BeppoSAX survey (Giommi et al. 2000, blue asterisks). The dashed blue line represents the model by Comastri et al. (1995). The slope is comparable to both the model and slope of other works.

sources missed at higher latitudes and in the Galactic plane because of high amounts of interstellar absorption. I do not believe this to be the case in this survey because of the majority of source spectra fitting extra-galactic sources, as will be seen in chapter 5.

The cumulative log(N)-log(S) for the hard energy band of 2-12 keV can be seen in Fig 4.3. Again, the red diamonds are *XMM-Newton Large scale survey* (Mateos et al., 2008), the green squares are the XMM-COSMOS field (Cappelluti et al., 2007), and purple flags are the *XMM-Newton* middle latitude survey (Novara et al., 2006). The blue asterisks are the BeppoSAX survey (Giommi et al., 2000). My data fit a power law index of -1.80 ± 0.07. The power law index for *XMM-Newton Large scale survey*, XMM-COSMOS, and BeppoSAX are -1.66 ± 0.04, -1.59 ± 0.04, and -1.76 ± 0.06

respectively. It should be noted that other works are from 2-10 keV and this survey was performed from 2-12 keV, however the power law slope is constant from 2-12 keV at $\Gamma = 1.7$ so the data will not be effected by the larger range of the energy band.

For the hard energy band, this survey shows results higher than other previous surveys. This result maybe because of this survey being substantially deeper than the afore mentioned surveys with Mateos et al. (2008) at ~7 ks, XMM-COSMOS at ~68 ks, *XMM-Newton* middle-latitude serendipitous survey at ~260 ks, and BeppoSAX at < 10 ks. This makes this survey more susceptible to bias effects at the threshold fluxes. This suggests that the source count distributions are strongly affected by source detection bias.

There are three main sources for the source detection bias; source confusion, spurious detections, and Eddington bias. Source confusion occurs when two or more sources fall in a single resolution element of the detector. For *XMM-Newton* the source confusion is reached at about $< 10^{16}$ erg/cm^2/s (Loaring et al., 2005), just above the flux limits reached for this survey. Thus the effect of source confusion in the source count distribution may be seen, especially in the lowest fluxes. Also, because of the deep nature of this survey, a high threshold of detection likelihood was used ($\mathcal{L} = 8$). This will cause the fraction of spurious detections in the sample to be slightly higher than that of other surveys (i.e. Mateos et al. (2008) used $\mathcal{L} \geq 15$). A detection likelihood of $\mathcal{L} = 10$ can correspond to a ~2.6% fraction of spurious detections in the 5-10 keV band (Loaring et al., 2005). This means the expected number of spurious sources per *XMM-Newton* pointing in this energy band is ~1.1, with this survey having 13 pointings. Eddington bias (Eddington, 1913, 1940) is because of the statistical uncertainties in the photon counting. The fluxes are statistically over estimated because there are more faint sources than bright sources. Thus more sources are "up-scattered" to a given flux measurement than those that are "down-scattered"

(Wang, 2004; Loaring et al., 2005). The severity of this effect depends on statistical errors in the measured flux values and the intrinsic slope of the $N(S)$. This effect will cause more faint sources to be detected than are actually present. For $\mathcal{L} = 6 - 7$, the Eddington bias can generate up to ~23% at the faintest fluxes. Thus the Eddington bias will affect this survey's results the most. This bias is even more prevalent in the harder energy band because of the background being greater causing a greater statistical error for a source at a given flux, seen in Fig 4.3.

Due to possible error because of bias, the log(N)-log(S) relation in the two bands show slightly higher slopes that previous surveys and models. This would be consistent with Eddington bias having a higher number of faint sources than bright sources. The higher values for the over all surface number density could be due to the high threshold detection set for the likelihood. This value could raise the surface number density as high as 23%.

Chapter 5

Spectral Analysis

5.1 Spectra Creation

Spectra for each point source and a corresponding background were extracted using `evselect` for all observations and cameras. The right ascension and declination for the brightest 30 sources were converted to (x, y) coordinates using `eregionanalys`. The angular resolution of *XMM-Newton* of 0.0055 degrees was used as a radius. The background was extracted from an off source region directly above each source with a radius of 0.060 degrees. The task `backscale` was performed on both the source and the background in order to scale the area of each region taking into account CCD boundaries and bad pixels. The task `rmfgen` was used to create a redistribution matrix file (RMF) that reformatted the detector and energy bounds information from the calibration of each instrument and uses the information to correct for instrumental effects. An ancillary response file (ARF) was created using `arfgen` that calibrated information to perform necessary corrections for instrumental factors (i.e. effective area, quantum efficiency, bad pixel correction, OoT). The longest eight exposures (revolutions 1491-1494, 1971-1974) were stacked using `mathpha`. Only the exposures where the source was within the FOV during that observation were included.

Fig 5.1 shows how the response matrices effect the shape of the final spectrum. All ancillary and response matrix files from all observations for each source and camera were combined using `addarf` and `addrmf`. To prepare for spectral fitting the FTOOLS task `grppha` was used for all cameras, sources, and background. This grouped the

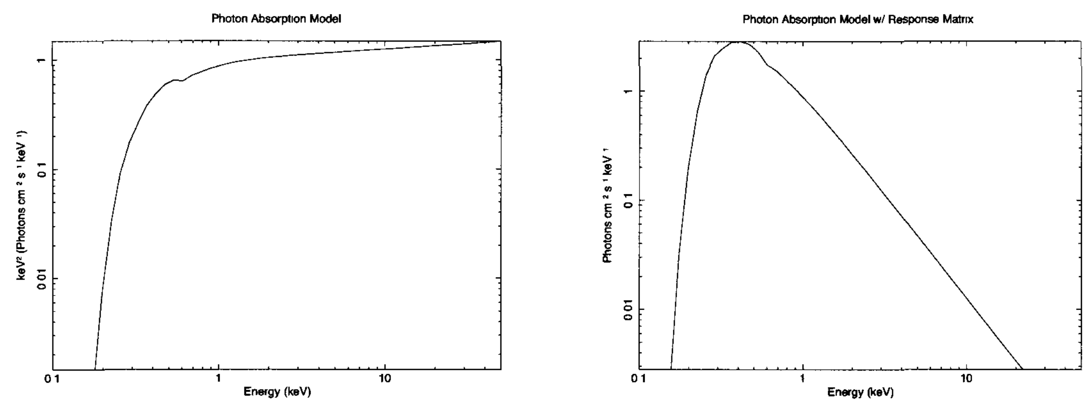

(a) (b)

Figure 5.1: **a)** Absorbed Power Law Model. **b)**Absorbed Power Law Model once the response matrices are included.

data, subtracted the background, and associated the ancillary and redistribution matrix files to the spectra. At this time, the background count rate was rescaled using the ratio of the source and background areas.

Some features appearing in the spectra that are a result of the camera's intrinsic background electronic noise (Freyberg et al., 2004). Fig 5.2 shows examples of the spectral line responses for the pn camera. The spectrum is taken when an observation was performed with the filter wheel closed. No radiation was recorded in this time so the spectrum is from the CCD instrumentation itself. The strength of these lines vary across the detector and are spatially inhomogeneous and therefore cannot be completely removed in processing. The most prominent lines that are visible in the spectra are the Al-Kα line and Cu-Kα.

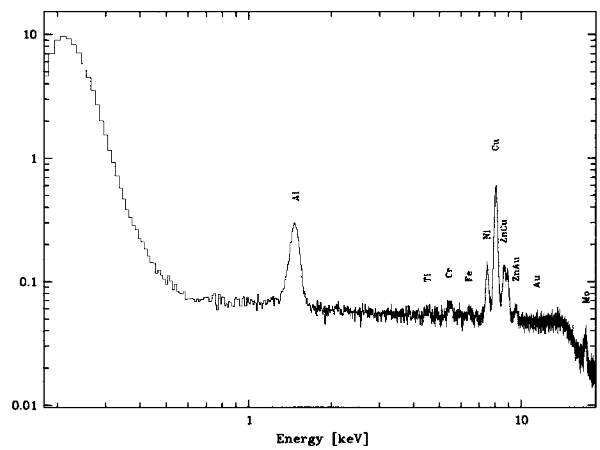

Figure 5.2: EPIC pn background spectrum in the 0.2 – 18keV range showing the prominent Al-Kα, Ni-Kα, and Cu-Kα lines at 1.5, 8.5, and 7.5 keV respectively (Freyberg et al., 2004).

5.2 Models

The X-ray spectral-fitting program *Xspec* (Arnaud et al., 2010)[1] was used for spectral fitting. The spectrum, having both background and response matrices included, was given a model with parameters that can be used to describe that spectrum. For each spectrum, a predicted spectrum is calculated and compared to the observed data. The fitting statistic is computed from the comparison between the predicted model and the actual spectra. A local (as opposed to global) fitting algorithm was used that was based on calculating the second derivative of the fitting statistic with respect to the the model parameters. The fitting statistic used was the reduced Chi-Squared (χ^2_ν) statistic with the degrees of freedom defined as the number of channels minus the number of model parameters (Arnaud et al., 2010). The model parameters were then varied to find the values that had given the best χ^2_ν statistic. If the $\chi^2_\nu > 1$, the model is considered a poor fit. If the $\chi^2_\nu < 1$, the errors on the data have been over-estimated. A $\chi^2_\nu = 1$ means a perfect fit. The confidence interval for a parameter

[1]http://heasarc.nasa.gov/xanadu/xspec/

Model	# of free parameters	free parameter
Photon Absorption Power Law	3	Column Density Photon Index Normalization
Mekal	4	Column Density Temperature [kt] Normalization Redshift
Blackbody	2	Temperature [kt] Normalization
Blackbody + Power Law	4	Temperature [kt] Normalization Photon Index Normalization

Table 5.1: Model Free Parameters. The normalization appears below the parameter to which it applies and it scales with flux.

is computed by varying the χ^2_ν until it has increased above the best-fit value.

All models used a Galactic absorption for the Milky Way starting at N_H=0.01 $\times 10^{22}$ cm^{-2} and photon index = 1.9 and then allowed to vary for the model fit. If an acceptable spectrum from both pn and MOS cameras were available, the models were fit to the combined spectrum. When using a combined pn and MOS spectrum, simultaneous fitting was done by linking the parameters and only allowing the cross-normalization to vary to account for the cameras different efficiency. All model fits for pn, combined MOS, and combined cameras for each source are shown in appendix C.

Four models were chosen for preliminary spectra fitting of all sources in a uniform way; a power law with photo-electric absorption model, the Mewe-Kaastra-Liedahl (Mekal) thermal plasma model, a blackbody spectrum model, and a combination of the power law and black body law model. The models can be seen in Fig 5.3 with free parameters in seen in Table 5.1.

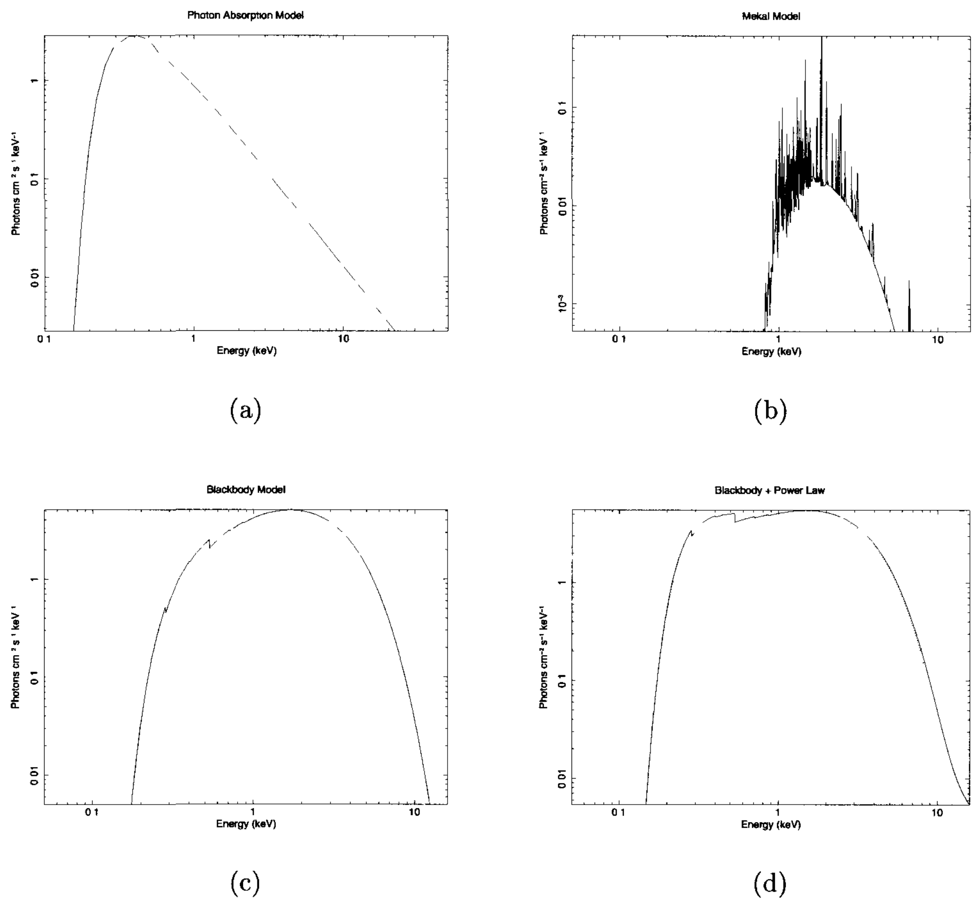

Figure 5.3: Models used for source fitting. All models used a fixed Galactic absorption for the Milky Way as N_H=0.0431$\times10^{22}$ cm^{-2}. The starting value of the intrinsic column density was set to N_H=0.01 $\times10^{22}$ cm^{-2} and the starting value of the photon index was set to Γ= 1.9 then allowed to vary for the model fit. Free parameters can bee seen in Table 5.1. **a)** Absorbed power law model. **b)** Mekal model. **c)** Blackbody model with starting temperature [kT] at 3 keV. **d)** Blackbody + Power Law model.

The power law ($F_\nu = \nu^{-\Gamma}$) with photo-electric absorption (N_H) model is shown in Fig 5.3a. This model fits most AGN because of the photons from the accretion disc being up scattered in the corona via the inverse Compton effect. The added absorption accounted for the column density within the AGN.

The Mewe-Kaastra-Liedahl (Mekal) thermal plasma model is the emission spectrum from a hot diffuse gas based on the calculations of Kaastra with Fe L calculations

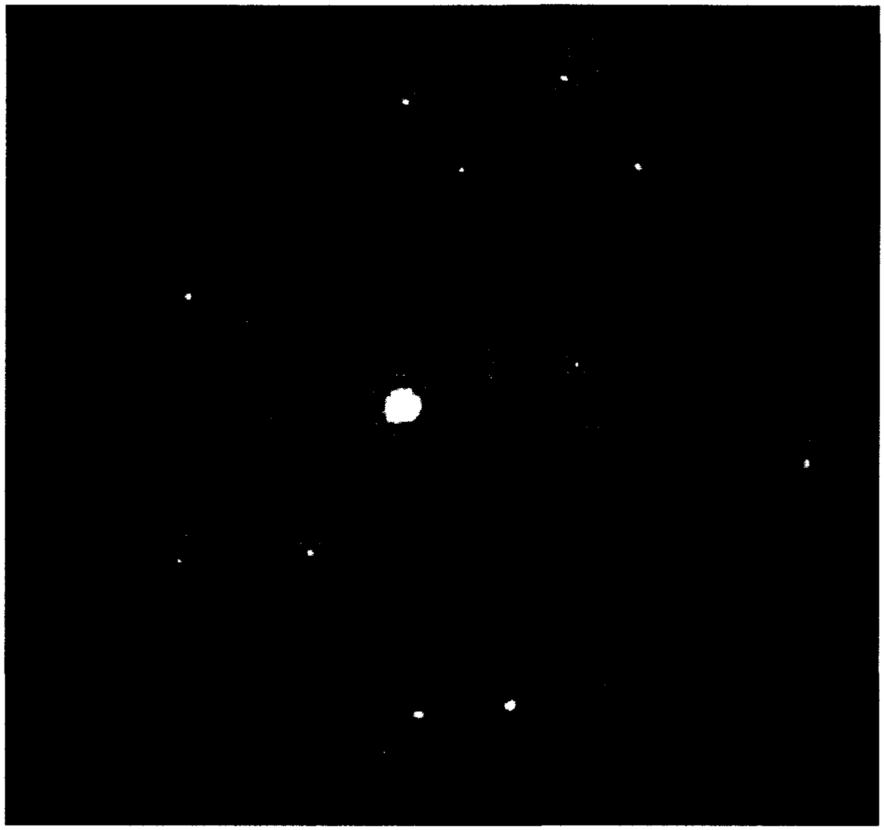

Figure 5.4: The 30 + 1 sources with a weighted source count > 650 used for spectral analysis. Source 6 is out of the field of view used for this image.

by Liedahl (Mewe et al., 1985, 1986; Kaastra, J.S., 1992). It has a bremsstrahlung continuum with various emission lines through out as seen in Fig 5.3b. This is most often found in the inter-cluster medium of galaxy clusters.

A blackbody spectrum model is a standard blackbody seen in Fig 5.3c. These spectra are usually found in globular clusters or X-ray binaries and are usually "super-soft".

The final modes is the blackbody plus power law model, which can also describes Type I AGN spectra well. It is a phenomenological model that has been shown describes type I AGN spectra. The nature of this model and why it fits type I AGN is debated [e.g. Gierliński & Done (2006), Ross & Fabian (2005)].

We generated spectra for sources with more than 650 weighted counts to ensure good statistics for model fitting. Thirty sources with weighted counts of $\gtrsim$ 650 appear in the FOV. Despite source 37 having $\ll$ 650 counts, its very blue colour was of interest and therefore analyzed. Fig 5.4 shows the location of the $30 + 1$ sources. Appendix B.2 shows a table of the best-fit model(s) for sources.

Fig 5.5a shows source 1, the AGN 1H0707-495. This is a complex spectrum and has many studies performed on it. More information of this AGN can be found in Gallo et al. (2004) and Zoghbi et al. (2010). Fig 5.5b shows source 2, the second brightest source in the FOV and the first source this work investigated. The combined pn (black) and MOS (red) spectrum shows a good fit with an absorbed power law. Source 2 is most likely a type I AGN. Hardness ratios (as will be discussed in chapter 6) also show characteristics of a type I AGN. Using source 2 as the calibration for a standard spectrum for a type I AGN, Fig 5.6 shows how the residuals looked when other models were used.

There were 16 X-ray sources fit the power law model within acceptable parameters,

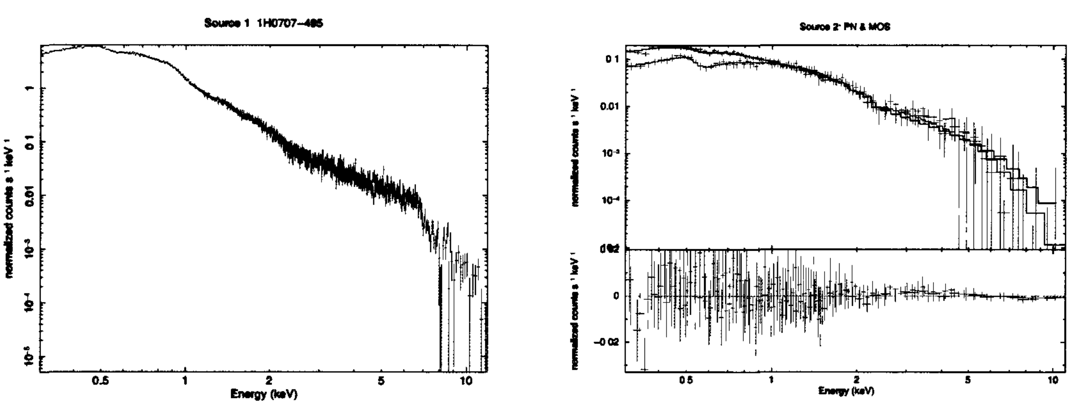

(a) (b)

Figure 5.5: **a)**Complex spectrum of 1H0707-495 (Fabian et al., 2009b). **b)**Source 2 pn (black) and MOS (red) spectra with photo-electric absorption power law including residuals seen in lower panel.

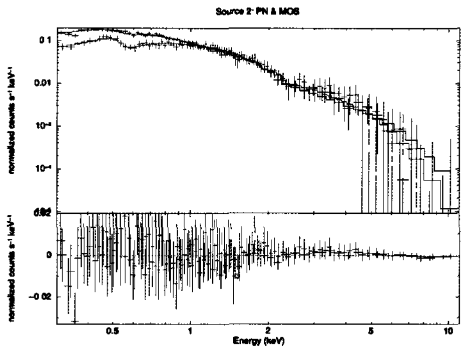

(a)

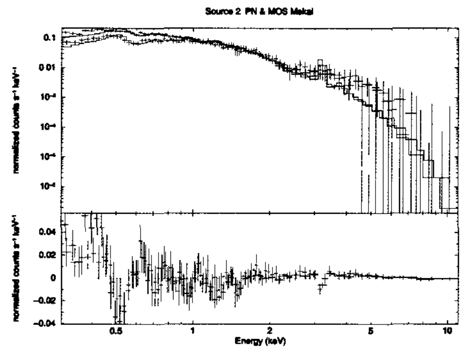

(b)

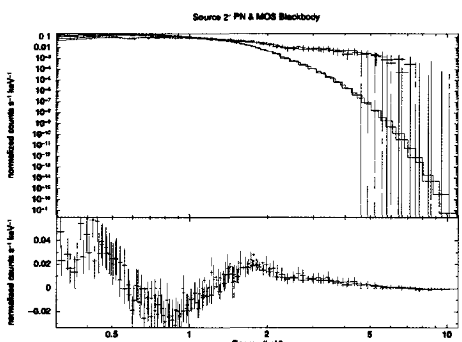

(c)

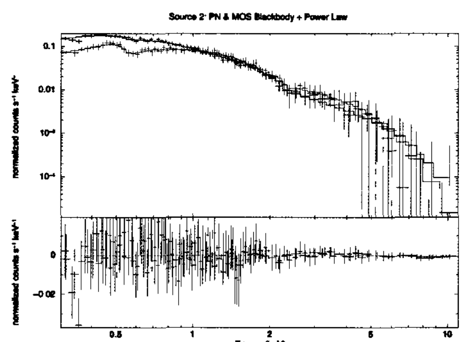

(d)

Figure 5.6: Residuals of source 2 for models of: **a**)Absorbed power law. **b**)Mekal. **c**)Blackbody. **d**)Blackbody + Power Law.

though some sources did show better fits with other models. Most sources that had an acceptable fit to the absorbed power law had $\Gamma \approx 1.5 - 2.3$ with errors ranging from $0.009 - 1.5$. The few that did not fall within that range mostly had another model with a better fit. Only five show the blackbody or Mekal model fitting well with four having fitting the blackbody + power law model. Four sources did not fit any of the four standard models used here and will be investigated in section 5.3. In most cases it is impossible to determine, with greater certainty, which model fits best because of comparable statistics. In many cases, the hard energy above 2 keV has error bars much too large and the source most likely background dominated. Sources

3, 9, 10, 20, and possibly 29 show a very steep slope before 2 keV. Because this is seen only with spectra from the pn camera, it may be a systematic phenomenon. These sources are spread out through the FOV, so one CCD cannot be responsible for the break. Most other sources have data beyond 2 keV showing it *is* possible to have data above the 2 keV energy. Looking at the "real-colour" image Fig 3.4, Sources 9 and 10 are predominately red (soft), while the others are green or blue (hard), suggesting that energy band selection effects are not present.

5.3 Anomalous Sources

A number of X-ray sources had spectra not well described by the four standard models. These sources required further investigation with additional models. Taking these characteristics into account, we could start to look into possible identification. Without additional information (e.g. optical or infrared data) these sources cannot be identified with certainty.

5.3.1 Source 22

The spectrum of source 22 (Fig 5.7a) appears different from most other sources. Most of the source spectra slope downward or flatten at low energies because of absorption within our own Galaxy as seen in Fig 5.7b. Source 22 has a strong soft excess and low absorption, suggesting the possibility it is Galactic. The four standard model used were not a good fit and can be seen in Fig C.23. Two possible identities of this source are considered.

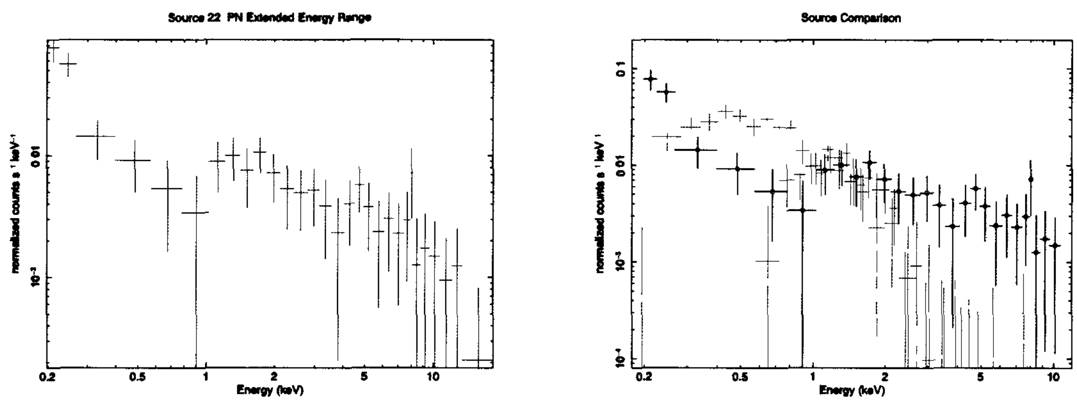

(a) (b)

Figure 5.7: **a)** Source 22 spectrum. **b)**Source 22 (black w/ circles) compared with source 2 (green), source 4 (red), and source 14 (blue).

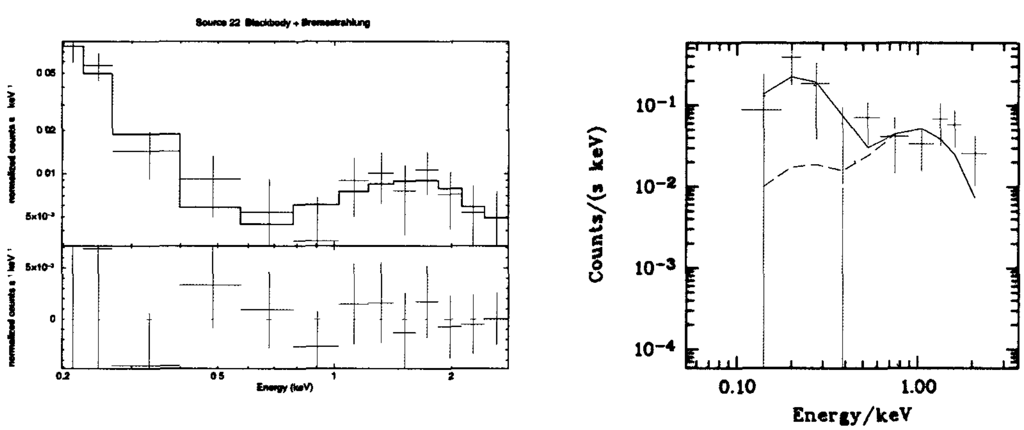

(a) (b)

Figure 5.8: **a)** The 0.2-3 keV range of source 22. **b)**AM Her J0704.2+6203 (Tovmassian et al., 2001). The similarities comparing source 22 to AM Her RX J0704.2+6203 can been seen.

A possible AM Her object

A model with a soft blackbody and hard bremsstrahlung was used and found to fit well (Fig 5.9a). This is the standard model for a polar cataclysmic variable (CV), or AM Her system seen in Fig 5.8b. AM Her systems are binary systems where one companion is a white dwarf with a high magnetic field that prevents an accretion disc from forming. Instead, the material from the companion star is directed to the poles by the magnetic field until it impacts on the surface at substantial velocities. The collision generates a shock wave giving rise to the hard X-ray portion of the spectrum. The hard X-rays heat the local area around the pole enough for the pole to become a source of intense soft X-rays[2]. A search of the SIMBAD Astronomical Database shows no counterpart within two arcmin.

While this model showed low residuals, there was a double hump in the harder energy ranges that was not accounted for. To include this into the model, a Gaussian absorption line (Fig 5.9b) and a cyclotron absorption line (Fig 5.9c) at 3.8 keV was used. The Gaussian absorption line reaches deeper into the absorption and reaches higher on the second hump; however there is no identifiable source for the line. Adding the cyclotron absorption line does not reach as deep into the line and does not reach the apex of the secondary hump but, if it is a CV, cyclotron effects are more likely. The models for AM Her systems show a blackbody temperature (kT) $\sim$20 eV and a bremsstrahlung temperature (kT) $\sim$10-40 keV. With this model of blackbody and bremsstrahlung, source 22 shows a blackbody temperature (kT) of 1.16 ± 0.38 keV and bremsstrahlung temperature (kT) of $6.27 \pm 0.66 \times 10^{-2}$ keV. This is inconsistent with a AM Her system. Furthermore, RX J0704.2+6203 has an unabsorbed luminosity of 3.4×10^{31} erg/s while source 22 models an unabsorbed luminosity of 4.26×10^{42} erg/s, much higher than AM Her systems.

A possible Low-ionization nuclear emission line region (LINER)

LINERs are galactic nuclei having high emission lines because of low ionization of some atomic species such as O^0, S^+, and N^+ (Heckman, 1980). There are two debates

[2]http://heasarc.gsfc.nasa.gov/docs/objects/cvs/cvstext.html#resources

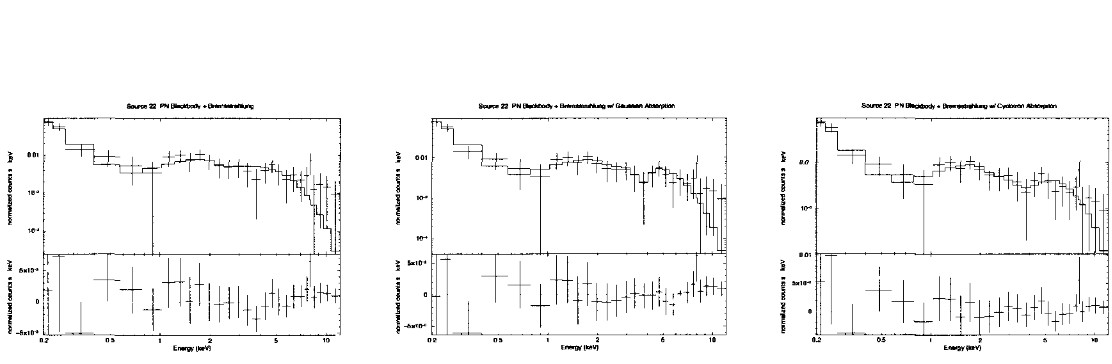

(a) (b) (c)

Figure 5.9: Source 22 with the **a)** blackbody + bremsstrahlung model, **b)**blackbody + bremsstrahlung with a Gaussian absorption line profile, and **c)**blackbody + bremsstrahlung with a cyclotron absorption line profile.

on LINERs: the source of the energy and how the ions are excited. The initial and still held belief is that LINERs are a transformation from normal galaxies to Seyfert galaxies (Heckman, 1980; Ho et al., 1993), while others believe LINERs are because of violent star formation activity and high metal abundances (Terlevich & Melnick, 1985; Shields, 1992). Ion excitation is equally debated and is not necessarily mutually exclusive to energy source beliefs. The one thought is that shocks drive the nuclear gas (Heckman, 1980) and the other is that photoionization, either stellar (Terlevich & Melnick, 1985; Shields, 1992) or AGN (Ho et al., 1993), causes the excitation.

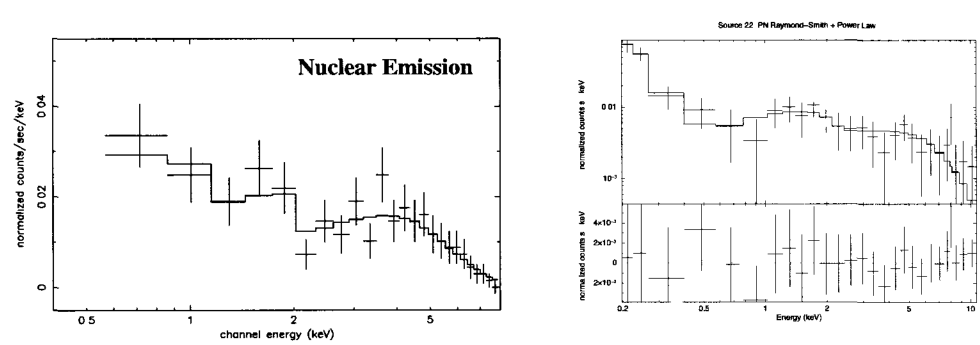

(a) (b)

Figure 5.10: **a)**Spectrum of LINER galaxy NGC 1052 assuming nuclear emission (Kadler et al., 2004). **b)** Source 22 showing an absorbed Raymond-Smith thermal plasma + power law model with residuals.

Assuming AGN energy source and excited ions via shocks, Fig 5.10a shows the spectrum of the nucleus of LINER galaxy NGC 1052. An absorbed Raymond-Smith thermal plasma combined with a power law model was used. The Raymond-Smith model shows emission spectra from hot, diffuse gas from several different elements ranging from 0.008 - 80 keV (Raymond & Smith, 1977). A power law type X-ray spectrum of the central X-ray source and a thermal plasma spectrum for the soft excess was assumed (Kadler et al., 2004). Compare that to the spectrum of source 22 in Fig 5.10b fit with the same model. The similarities are easily seen though the fit does not account for the deeper absorption like features at 0.9 and 4 keV. Standard redshift for a LINER is $z \approx 0.8 - 0.9$ (Lemaux et al., 2010), the *Xspec* Raymond-Smith + power law model for source 22 gave a redshift of $z = 1.26 \pm 0.35$ assuming a NCG 1052-type spectrum for a LINER. X-ray luminosity of a LINER has been found to be $L_x \sim 10^{42} - 10^{43}$ erg/s (Brightman & Nandra, 2011). Using a conservative redshift of $z = 1.00$, source 22 was found to have a X-ray luminosity $L_x \approx 6.83 \times 10^{44}$ erg/s, very high any current values for a LINER.

Of the two possible objects described above, the more likely appears to be a LINER. While the spectrum is a good fit to the model used for AM Her systems, the numbers from that model are several orders of magnitude away from accepted values. The numbers from the LINER model are not a perfect fit to accepted values, however they are much closer that the AM Her systems numbers. Any confirmation of a LINER nature for source 22 would require additional optical and/or near infrared observations.

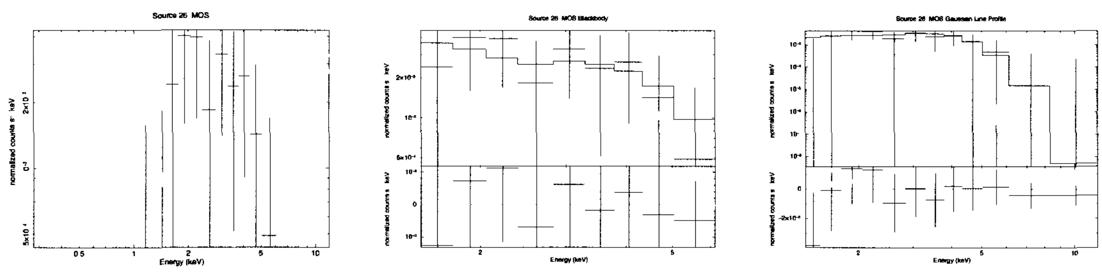

(a) (b) (c)

Figure 5.11: **a)** MOS spectrum of source 26. Model fits and residuals are shown for; **b)**blackbody and **c)**Gaussian line profile.

5.3.2 Source 26

Source number 26 can be seen in Fig 5.11a. It can be seen that the spectral quality has become lower. It can be seen that the peak of the spectrum is at harder energy as well as a sharp drop off on either side of the peak. Fig 5.11b and c show a possible fit with a blackbody and a Gaussian line profile, respectively. If we assume the source is not redshifted, the peak shows an emission line fitting the Gaussian at ~2 keV. Looking at the spectrum, one could consider a peak anywhere between 2-3 keV. Fig 5.12 show some spectral possibilities for source 26. Fig 5.12a shows the spectrum of a type II AGN (Mateos et al., 2005). There is a similar steep rise to the peak at ~2 keV and then a steep drop from the peak, though source 26 does not have the additional component that this type II AGN has at ≥4 keV. Fig 5.12b and c show spectra of high mass X-ray binaries (HMXB) systems. HMXB systems consist of a neutron star or black hole with a high mass stellar companion (Masetti et al., 2010). Both spectra show a peak spanning across the 1-2 keV energy range, but neither of them have the steep rise or drop seen in source 26. A search of the NASA/IPAC Extragalactic Database and SIMBAD Astronomical Database also shows no counterpart or high mass stellar companion within 1.5 arcmin.

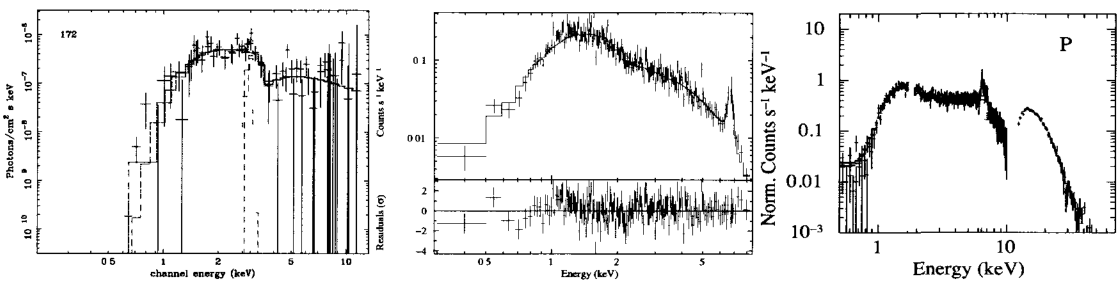

(a) (b) (c)

Figure 5.12: **a)** Spectrum of Mateos et al. (2005) type II AGN "source 172" with an absorption edge at ~7.56 keV. **b)**X-ray spectrum for HMXB 1ES 1210-646 during XRT observation (Masetti et al., 2010). **c)**Time resolved spectrum of HMXB Cen X-3 from *Suzaku* (Naik et al., 2011).

Using the the X-ray photon energy emission lines from Bearden (1967), the possible X-ray emission lines for the Gaussian at ~2 keV are phosphorus Kα and sulfur Kα. Phosphorus Kα has been seen in stellar wind X-rays from OB stars (Waldron & Cassinelli, 2007; Cassinelli et al., 2008) and sulfur Kα has been seen in jets of binary star systems (Kotani et al., 1994). The latter could correspond to the HMXB spectra discussed above, but the narrow energy and low resolution of the spectrum make it implausible to make a positive determination for this source.

5.3.3 Source 27

The spectrum for source 27 can be seen in Fig 5.13a. This consists of a sharp apex at ~0.85 keV and steep drop offs on each side of that peak. The majority of the spectrum is located within 0.5 and 1.5 keV. Fitting the four input models (Appendix C.26) showed the peak distinctively appearing in the residuals. To lessen the residuals of the peak, Gaussian (Fig 5.13b) and Gaussian with blackbody (Fig 5.13c) models were fit with a line energy of ~0.85 keV.

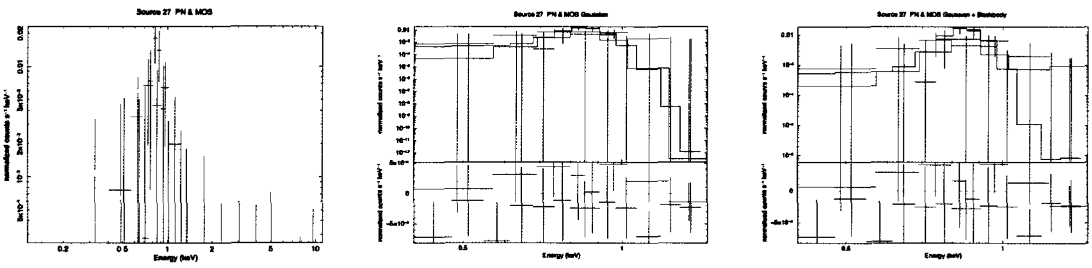

(a) (b) (c)

Figure 5.13: **a)** pn spectrum of source 27. Model fits and residuals are shown for; **b)**Gaussian and **c)**Gaussian + blackbody.

A possible AM Her object

Again, we look at the AM Her CV. Fig 5.14a shows SDSS J1553. It can be seen that compared to J0704.2+6203 from a previous section; there is no hard component to the spectrum of SDSS J1553. The absence of this hard energy shows that accretion shock at the magnetic poles is not present because of a lower accretion rate but warming is still present to cause the soft X-rays (Szkody et al., 2004). This spectrum is fit with a Mekal thermal plasma + blackbody model, Mekal fitting the peak and blackbody fitting the soft excess. Fitting the same model to source 27 gives a relatively good fit (Fig 5.14b). The peak is still present in the residuals and the blackbody portion is not represented because of the absence of spectral energy < 0.5 keV. The fit of SDSS J1553 found the thermal plasma temperature (kT) to be 0.78 keV (Szkody et al., 2004) and source 27 to be 0.89 keV, showing similar numbers and magnitudes. This is merely one example of a low accretion AM Her polar and is not necessarily representative of all such systems.

A possible Herbig Ae/Be Star

A Herbig Ae/Be star are of spectral type A or B with emission lines, luminosity class III-V, and have a infrared excess because of hot or cool circumstellar dust (Waters & Waelkens, 1998). It has only recently been found that X-rays are emitted by these objects via accretion shock.

Fig 5.15a shows the X-ray spectrum of Herbig Ae HD 163296 (from Günther & Schmitt, 2009) and MWC 480 (Grady et al., 2010) fit with an absorbed one temperature (1T), thin-thermal plasma model finding a temperature (kT) of 0.5 and 0.47 keV, respectively. Fitting the same model to source 27 (Fig 5.15b) shows a similar trend with the temperature (kT) being 0.64 keV.

It must be noted that because of the simplistic curve, large error bars, and limited energy range of the spectrum of source 27, both the Mekal thermal plasma and absorbed 1T thin-thermal plasma model look identical and only differ in temperature (kT) by 0.25 keV and flux by 0.024 erg/cm^2/s. With such a limited energy spectrum, identification solely by X-rays will be purely speculative.

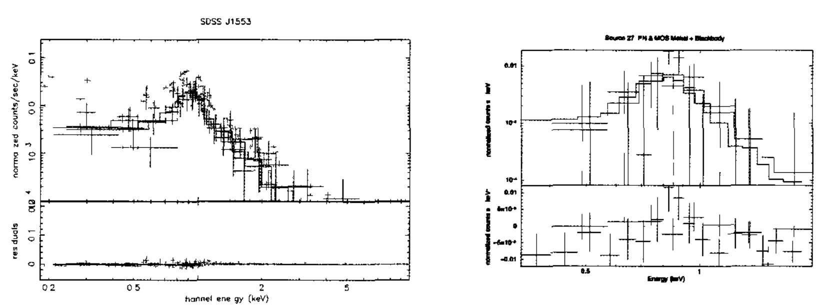

(a) (b)

Figure 5.14: **a)** Spectrum of SDSS J1553 (Szkody et al., 2004). **b)** Source 27 fit with a Mekal + Blackbody model.

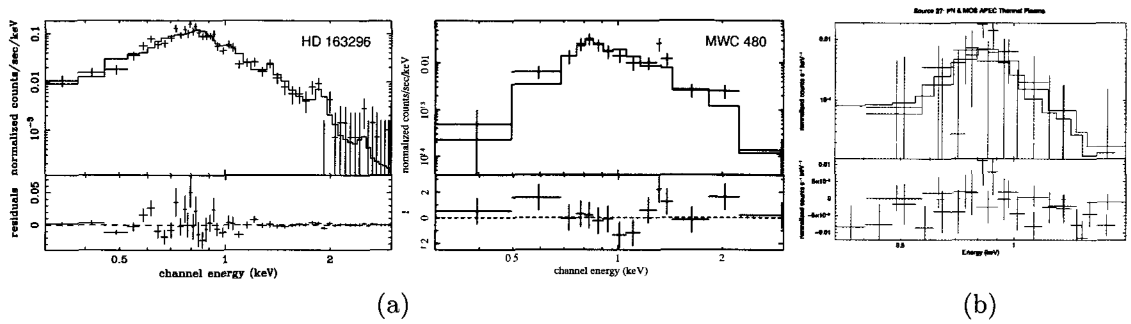

Figure 5.15: **a)** Spectrum of HD 163296 (after Günther & Schmitt, 2009) and MWC 480 (Grady et al., 2010). **b)** Source 27 fit with a APEC thermal plasma model.

5.3.4 Source 37: Big Blue

As mentioned before, it is preferable to have > 650 weighted counts to form a spectrum. While investigating the "real-colour" image, there was one very blue/hard source (labeled "Big Blue" in Fig 5.4) that warranted investigation.

The spectrum seen in Fig 5.16a shows a drastic degradation in quality and resolution compared to the other sources because the count rate is much less than that preferred. Though the quality is lower, a general trend can be obtained from this source. The spectrum is well fit with an absorbed power law and Gaussian line profile where the Gaussian is left to be at an arbitrary energy. The model found the Gaussian peaks at ~5.4 keV. If one assumes the Gaussian profile to be the Fe Kα line normally at 6.4 keV, a redshift can be determined at z=0.17. Assuming this redshift and Galactic N_H of 0.0431×10^{22} cm^{-2}, and a photon index $\Gamma = 1.8$, Big Blue is found to have an unabsorbed X-ray luminosity of 1.09×10^{42} erg/s and a column density of $0.43 \pm 0.31 \times 10^{24}$ cm^{-2} in the 0.5 - 12 keV band, putting it on the lower limits of a mildly Compton thick (CT) source (Maiolino et al., 1998). CT sources are heavily obscured AGN and are only visible via indirect X-rays that are reflected and scattered (Brandt & Hasinger, 2005). Because of the low luminosity, few CT sources

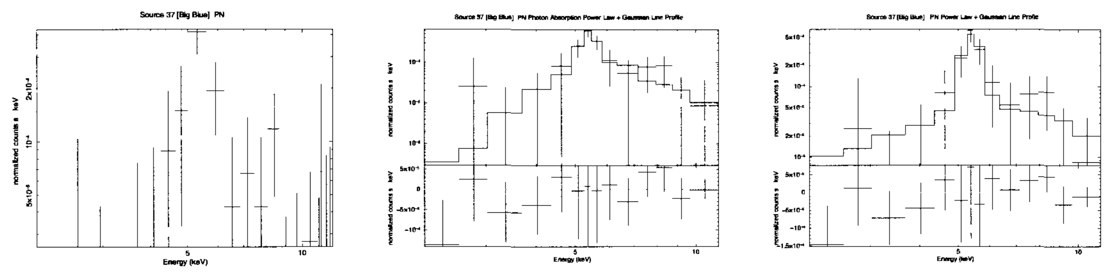

(a) (b) (c)

Figure 5.16: **a)**pn spectrum of source 37 [Big Blue]. Model fits and residuals are shown for; **b)**Absorbed power law + Gaussian and **c)**power law + Gaussian.

have been found though it is thought the population of mildly CT sources make up to a 40% (Comastri, 2004) contribution to synthesis models for the CXRB. These CT source are needed in order to match the peak of the CXRB spectrum at about 30 keV (Treister et al., 2010).

Chapter 6

X-ray Colour-Colour Diagram

Hardness Ratio

X-ray colours, or Hardness Ratios (HR), are commonly used in X-ray astronomy to identify spectral properties of sources when data is insufficient to produce a spectrum of the source. The SAS task `emldetect` used the count rates in the four different energy bands to derive camera-specific hardness ratios. Each hardness ratio is defined as

$$\mathrm{HR} = \frac{CR_{hard} - CR_{soft}}{CR_{hard} + CR_{soft}}$$

where CR_{hard} and CR_{soft} are the count rates in hard and soft energy bands, respectively.

Figure 6.1 and Figure 6.2 show the pn cameras X-ray colour-colour diagram for different colours. Superimposed on the figure is a model grid for absorbed power law spectra. The neutral hydrogen absorption (from the source galaxy) for the models were set with log N_H from 20 to 23 with steps of 0.5, increasing N_H from bottom to top. The photon indices were set to $\Gamma = 0, 1, 2, 3$, increasing to the left. Black dots are those sources with unconstrained uncertainties while the turquoise points show sources with reasonably constrained uncertainties (< 0.1) as shown by the error bars.

Hardness ratios can be seen for the soft energy bands in Fig 6.1. Typical type I AGN are relatively soft with a photon index $\Gamma \approx 1.7 - 2$ and low apparent column densities of log $N_H < 21.5$ cm^{-2} (Hasinger et al., 2001). Fifteen sources with error < 0.1 show type I AGN characteristics in this field. Five sources show with uncertainty

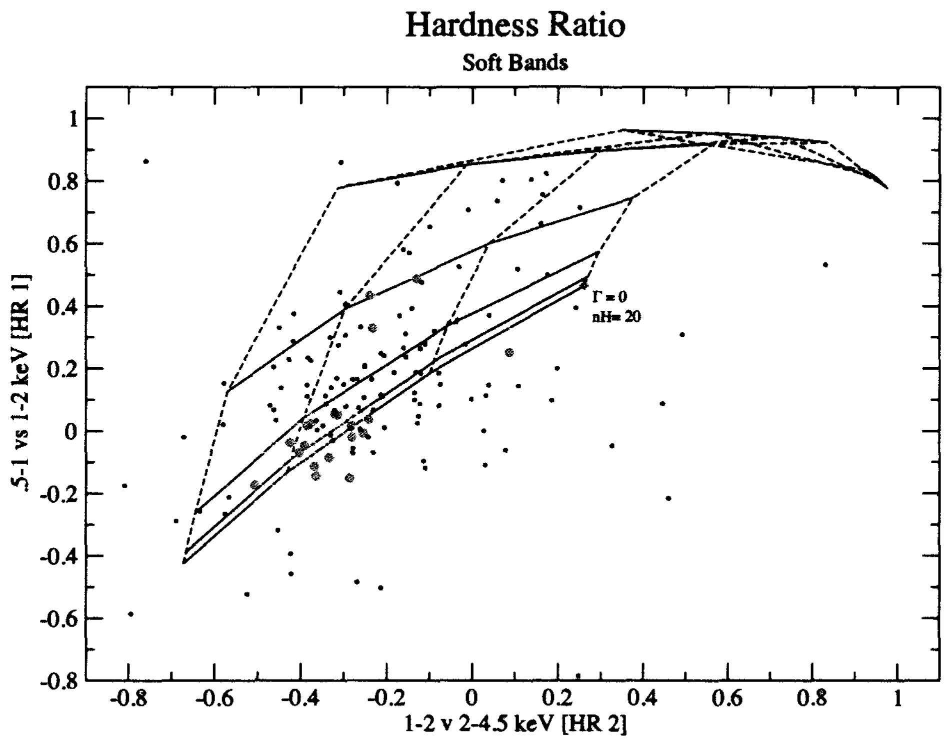

Figure 6.1: Hardness ratios for soft energy bands of 0.5-1 versus 1-2 keV ($HR1$) to 1-2 versus 2-4.5 keV ($HR2$) of the pn camera. The grid gives the expected hardness ratios for the power law models with photon indices $\Gamma = 0$, 1 ,2 and ,3 (dashed lines) and neutral hydrogen absorption of log N_H between 20 and 23 with steps of 0.5 (solid lines). The location of $\Gamma = 0$ and log $N_H = 20$ is marked with a orange diamond. Cyan circles show the hardness ratios of sources with error < 0.1 while the black dots show the hardness ratios with error > 0.1.

< 0.1 are located over a wider area that could be type II AGN or galaxy clusters. A significant portion of the sources are located within $\Gamma \approx 1 - 2$, consistent with the population of X-ray sources. Appendix A.1 shows the pn camera's hardness ratio data for all sources. Sources that had a constrained hardness ratio were consistent with the spectral identification.

Fig 6.2 shows the harder energy band hardness ratios. It is seen that many of the points lie to the right of the model grid. It has been suggested that *XMM-*

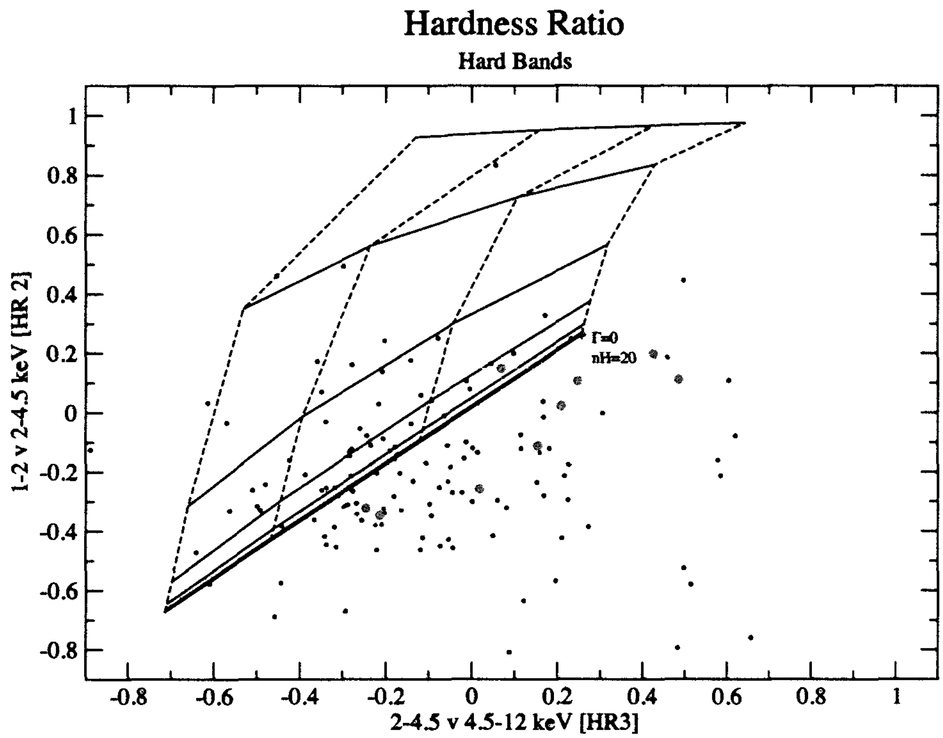

Figure 6.2: Hardness ratios for hard energy bands of 2-4.5 keV ($HR2$) versus 4.5-12 keV ($HR3$) of the pn camera. The grid gives the expected hardness ratios for the photon power law models with photon indices $\Gamma = 0$, 1 ,2 and ,3 (dashed lines) and neutral hydrogen absorption of log N_H between 20 and 23 with steps of 0.5 (solid lines). The location of $\Gamma = 0$ and $N_H = 20$ is marked with a orange diamond. Cyan circles show the hardness ratios of sources with error < 0.1 while the black dots show the hardness ratios with error > 0.1.

Newton tends to characterize points typically harder than previous X-ray observatories because of the wide energy band and sensitivity to the hard band (Hasinger et al., 2001). If this is the case, the points can be considered to be slightly softer and shifted to the left where the hardness ratios are softer. At this time there isn't a way to estimate how much harder *XMM-Newton* may characterize the sources. It is also possible that the sources are background dominant at high energy levels. This would cause a flatter spectrum and an increased hardness ratio.

The hardness ratio analysis for the softer energy bands is consistent with many of sources being type I AGN. Some sources are less constrained and could represent type II AGN or galaxy clusters. The harder energy bands show less continuity with the model webbing. This could be because of instrumental manifestations or the majority of sources being background dominant.

Chapter 7

Summary and Conclusions

The thirteen *XMM-Newton EPIC* observations of the intermediate-latitude field around type I AGN 1H0707-495 were analyzed in order to investigate the properties of the X-ray source population. This survey covers an area of ~0.7 deg^2. A total of 128 sources were detected in the 0.5-12 keV energy band excluding the AGN and surrounding one arcmin. This survey has a limiting flux of 6.72×10^{-16}, 2.94×10^{-15}, and 1.14×10^{-14} ergs/cm^2/sec in the 0.5-2, 2-4.5, and 4.5-12 keV bands, respectively.

Together with the source catalogue, we derived a log(N)-log(S) relation in the flux interval sampled by the survey. The log(N)-log(S) relation in the hard and soft bands show slightly higher slopes then previous surveys and models because of possible bias from the deeper observation. There has also been a shift to a slightly higher value of surface number density for the fluxes.

Spectra were created and analyzed for the 30 brightest sources and one additional source of interest. Many of the sources followed the power law model for type I AGN. Three sources warranted further investigation, however positive identification is not possible without additional wavelength observations. Source 22 spectrum showed resemblances to an AM Her polar system, though the blackbody and bremsstrahlung temperatures did not fit that of an AM Her polar. The possibility of a LINER was also investigated, but the values of redshift and X-ray luminosity was found to be high. Source 26 was compared to the spectrum of a type II AGN and a HMXB, but the spectrum is of limited quality and energy coverage so it is difficult to make a definite determination. Source 27 spectrum showed relations to a low accretion rate AM Her system and a Herbig Ae star, again the limited energy range and low resolution prevented any positive identification. The hard source 37 (Big Blue) was investigated and found to be a possible candidate for a mildly Compton thick source.

Colour-colour diagrams were made using hardness ratios of each source and then superimposed on models for identification. The soft band plot show a clustering of possible type I AGN around $\Gamma \approx 1.7 - 2$ and log $N_H \approx 20 - 21$ cm^{-2} with additional sources located within the model grid. The hard band plot shows sources to be harder than the model grid although *XMM-Newton* characterizing sources harder than previous X-ray observatories.

Future work could be done in order to improve this survey. Source time variability would show any change in X-ray luminosity over time. This would help in identifying sources. For example, AGN and binary systems in outburst will show variation in luminosity over time while clusters of galaxies remain constant. Timing analysis could also be used to detect X-ray transients. Investigation into optical or infrared counterparts or companions will help identify and classify sources. For example, if an optical companion is found for source 22, source 26, or source 27 then there would be further evidence for binary systems. Optical data would allow distance determination as well as AGN classification.

Bibliography

Antonucci, R. 1993, ARA&A, 31, 473

Antonucci, R. R. J., & Miller, J. S. 1985, ApJ, 297, 621

Arnaud, K., Dorman, B., & Gordon, C. 2010, Xspec: An X-Ray Spectral Fitting Package , HEASARC Astrophysics Science Division, NASA/GSFC

Baldi, A., Molendi, S., Comastri, A., Fiore, F., Matt, G., & Vignali, C. 2002, ApJ, 564, 190

Bearden, J. A. 1967, Reviews of Modern Physics, 39, 78

Blackburn, J. K. 1995, in Astronomical Society of the Pacific Conference Series, Vol. 77, Astronomical Data Analysis Software and Systems IV, ed. R. A. Shaw, H. E. Payne, & J. J. E. Hayes, 367

Brandt, W. N. 2007, in Astronomical Society of the Pacific Conference Series, Vol. 380, Deepest Astronomical Surveys, ed. J. Afonso, H. C. Ferguson, B. Mobasher, & R. Norris, 103

Brandt, W. N., et al. 2001, AJ, 122, 2810

Brandt, W. N., & Hasinger, G. 2005, ARA&A, 43, 827

Brightman, M., & Nandra, K. 2011, MNRAS, 414, 3084

Caccianiga, A., et al. 2008, A&A, 477, 735

Cappelluti, N., et al. 2007, ApJS, 172, 341

Cash, W. 1979, ApJ, 228, 939

Cassinelli, J. P., Ignace, R., Waldron, W. L., Cho, J., Murphy, N. A., & Lazarian, A. 2008, ApJ, 683, 1052

Comastri, A. 2004, in Astrophysics and Space Science Library, Vol. 308, Supermassive Black Holes in the Distant Universe, ed. A. J. Barger, 245

Comastri, A., Setti, G., Zamorani, G., & Hasinger, G. 1995, A&A, 296, 1

Della Ceca, R., et al. 2004, A&A, 428, 383

Eddington, A. S. 1913, MNRAS, 73, 359

Eddington, A. S., Sir. 1940, MNRAS, 100, 354

Elvis, M., Wilkes, B. J., & Tananbaum, H. 1985, ApJ, 292, 357

ESA: XMM-Newton SOC. 2010, XMM-Newton Handbook, European Space Agency , XMM-Newton Scientific Operations Centre Team

Fabian, A. C., et al. 2009a, ArXiv e-prints

Fabian, A. C., et al. 2009b, Nature, 459, 540

Freyberg, M. J., et al. 2004, in Presented at the Society of Photo-Optical Instrumentation Engineers (SPIE) Conference, Vol. 5165, Society of Photo-Optical Instrumentation Engineers (SPIE) Conference Series, ed. K. A. Flanagan & O. H. W. Siegmund, 112

Gallo, L. C., Tanaka, Y., Boller, T., Fabian, A. C., Vaughan, S., & Brandt, W. N. 2004, MNRAS, 353, 1064

Giacconi, R., Gursky, H., Paolini, F. R., & Rossi, B. B. 1962, Physical Review Letters, 9, 439

Giacconi, R., et al. 2001, ApJ, 551, 624

Giacconi, R., et al. 2002, ApJS, 139, 369

Gierliński, M., & Done, C. 2006, MNRAS, 371, L16

Gilli, R., Salvati, M., & Hasinger, G. 2001, A&A, 366, 407

Giommi, P., Perri, M., & Fiore, F. 2000, A&A, 362, 799

Grady, C. A., et al. 2010, ApJ, 719, 1565

Günther, H. M., & Schmitt, J. H. M. M. 2009, A&A, 494, 1041

Hasinger, G., et al. 2001, A&A, 365, L45

Hasinger, G., et al. 2007, ApJS, 172, 29

Hasinger, G., Miyaji, T., & Schmidt, M. 2005, A&A, 441, 417

Heckman, T. M. 1980, A&A, 87, 152

Ho, L. C., Filippenko, A. V., & Sargent, W. L. W. 1993, ApJ, 417, 63

I. de la Calle. 2011, User Guide to the XMM-Newton Science Analysis System , European Space Agency

Jansen, F., et al. 2001, A&A, 365, L1

Kaastra, J.S. 1992, An X-Ray Spectral Code for Optically Thin Plasmas: Internal SRON-Leiden report v2.0, Internal SRON-Leiden

Kadler, M., Kerp, J., Ros, E., Falcke, H., Pogge, R. W., & Zensus, J. A. 2004, A&A, 420, 467

Kotani, T., et al. 1994, PASJ, 46, L147

Lemaux, B., Lubin, L. M., Shapley, A., Kocevski, D., Gal, R. R., & Squires, G. 2010, in Bulletin of the American Astronomical Society, Vol. 42, American Astronomical Society Meeting Abstracts #215, 330.07

Loaring, N. S., et al. 2005, MNRAS, 362, 1371

Maiolino, R., Salvati, M., Bassani, L., Dadina, M., della Ceca, R., Matt, G., Risaliti, G., & Zamorani, G. 1998, A&A, 338, 781

Marshall, F. E., Boldt, E. A., Holt, S. S., Miller, R. B., Mushotzky, R. F., Rose, L. A., Rothschild, R. E., & Serlemitsos, P. J. 1980, ApJ, 235, 4

Masetti, N., et al. 2010, A&A, 511, A48

Mateos, S., Barcons, X., Carrera, F. J., Ceballos, M. T., Hasinger, G., Lehmann, I., Fabian, A. C., & Streblyanska, A. 2005, A&A, 444, 79

Mateos, S., et al. 2008, A&A, 492, 51

McHardy, I. M., et al. 1998, MNRAS, 295, 641

Melia, F. 2009, High-Energy Astrophysics (Princeton University Press)

Mewe, R., Gronenschild, E. H. B. M., & van den Oord, G. H. J. 1985, A&AS, 62, 197

Mewe, R., Lemen, J. R., & van den Oord, G. H. J. 1986, A&AS, 65, 511

Morley, J. E., Briggs, K. R., Pye, J. P., Favata, F., Micela, G., & Sciortino, S. 2001, MNRAS, 326, 1161

Motch, C., et al. 1998, A&AS, 132, 341

Naik, S., Paul, B., & Ali, Z. 2011, ArXiv e-prints

Nardini, E., Fabian, A. C., Reis, R. C., & Walton, D. J. 2011, MNRAS, 410, 1251

Netzer, H. 1990, in Active Galactic Nuclei, ed. R. D. Blandford, H. Netzer, L. Woltjer, T. J.-L. Courvoisier, & M. Mayor, 57

Novara, G., La Palombara, N., Carangelo, N., de Luca, A., Caraveo, P. A., Mignani, R. P., & Bignami, G. F. 2006, A&A, 448, 93

Novara, G., La Palombara, N., Mignani, R. P., Hatziminaoglou, E., Schirmer, M., de Luca, A., & Caraveo, P. A. 2009, A&A, 501, 103

Pravdo, S. H., & Marshall, F. E. 1984, ApJ, 281, 570

Raymond, J. C., & Smith, B. W. 1977, ApJS, 35, 419

Rodríguez-Pascual, P., & González-Riestra, R. 2008, The Behavior of the XMMNewton Background: From the beginning of the mission until January 2008 , XMMSOC User Support Group

Rosati, P., et al. 2002, ApJ, 566, 667

Ross, R. R., & Fabian, A. C. 2005, MNRAS, 358, 211

Schmidt, M., et al. 1998, A&A, 329, 495

Setti, G., & Woltjer, L. 1973, in IAU Symposium, Vol. 55, X- and Gamma-Ray Astronomy, ed. H. Bradt & R. Giacconi, 208

Shields, J. C. 1992, ApJ, 399, L27

Strüder, L., et al. 2001, A&A, 365, L18

Szkody, P., et al. 2004, AJ, 128, 2443

Terlevich, R., & Melnick, J. 1985, MNRAS, 213, 841

Torres, D. F., & Anchordoqui, L. A. 2004, Reports on Progress in Physics, 67, 1663

Tovmassian, G. H., et al. 2001, A&A, 379, 199

Treister, E., Urry, M., Cardamone, C., Virani, S., Schawinski, K., & Gawiser, E. 2010, Twelfth International Solar Wind Conference, 1248, 381

Turner, M. J. L., et al. 2001, A&A, 365, L27

Waldron, W. L., & Cassinelli, J. P. 2007, ApJ, 668, 456

Wang, Q. D. 2004, ApJ, 612, 159

Waters, L. B. F. M., & Waelkens, C. 1998, ARA&A, 36, 233

Watson, M. G., et al. 2009, A&A, 493, 339

Zamorani, G., et al. 1999, A&A, 346, 731

Zoghbi, A., Fabian, A. C., Uttley, P., Miniutti, G., Gallo, L. C., Reynolds, C. S., Miller, J. M., & Ponti, G. 2010, MNRAS, 401, 2419

Appendix A

Source Catalogue

Table A.1 lists the sources from brightest to dimmest. The convention used to determine order was taking the brightest weighted source count. The right accession and declination is shown in units of degrees. All harness ratios and errors are shown.

Table A.1: Source Catalogue

Source	RA [Deg]	Dec [Deg]	Weighted Source Counts	HR_1	HR_1 error	HR_2	HR_2 error	HR_3	HR_3 error
2	107 083081	-49 7141847	5930	0 0746	0 2757	-0 2655	0 2805	-0 2770	0 9000
3	107 248772	-49 6327011	2048	0 1159	0 2256	-0 2143	0 2492	-0 2814	0 3707
4	106 836170	-49 5842872	1772	0 5242	0 3028	-0 0306	0 2823	-0 3390	0 5306
5	107 158768	-49 7193053	1714	0 5699	0 2213	-0 1469	0 2489	-0 2831	0 4142
6	107 194975	-49 3046673	1461	0 0787	0 1878	-0 2945	0 2858	0 2244	1 3643
7	107 178871	-49 6641354	1421	0 0037	0 2577	-0 3612	0 3501	-0 3658	1 4273
8	107 281495	-49 5594501	1388	0 3920	0 2064	-0 1414	0 1650	-0 1726	2 4463
9	107 027674	-49 5301892	1383	0 2088	0 2133	-0 2522	0 2156	-0 3179	0 4761
10	107 105355	-49 6307968	1374	0 0155	0 1366	-0 3780	0 1463	-0 2241	1 2289
11	107 170849	-49 3874060	1252	0 1125	0 2493	-0 3425	0 2789	-0 2668	1 7859
12	107 349161	-49 4928735	1233	0 2267	0 2463	-0 3767	0 2711	-0 2096	0 6710
13	107 124982	-49 4242479	1230	0 1644	0 2535	-0 2800	0 2948	-0 3103	15 7886
14	107 342340	-49 3685220	1188	-0 0305	0 2626	-0 3243	0 3262	-0 2051	4 3029
15	107 103414	-49 5405571	1166	0 0059	0 1412	-0 2616	0 1727	-0 5101	0 5344
16	107 000761	-49 7180398	1155	0 3329	0 2814	-0 2609	0 3079	-0 3492	4 0132
17	107 295322	-49 5157529	1129	0 0067	0 1195	-0 2833	0 1482	-0 1812	0 2854
18	107 101911	-49 5222032	1069	-0 0125	0 1096	-0 3298	0 1306	-0 4912	0 3172
19	107 356237	-49 6363473	1033	0 1464	0 2571	-0 3850	0 2787	-0 3187	0 9027
20	107 300157	-49 5065693	934	0 0173	0 1662	-0 3474	0 2210	-0 0936	0 3728
21	107 038688	-49 3749904	890	0 0869	0 2640	-0 3404	0 2896	-0 2034	0 6319
22	107 114739	-49 3880160	886	0 8031	0 3156	0 1374	0 2730	-0 2084	0 4457
23	107 187694	-49 7402256	872	0 0339	0 2392	-0 3632	0 2857	-0 2562	0 7600
24	107 012156	-49 3623631	838	0 2872	0 2682	-0 4171	0 2894	-0 3418	0 9031

cont

Table A 1

Source	RA [Deg]	Dec [Deg]	Weighted Source Counts	HR_1	HR_1 error	HR_2	HR_2 error	HR_3	HR_3 error
25	107 014483	-49 5670380	771	0 0669	0 2542	-0 3212	0 3221	0 0811	1 3251
26	107 456573	-49 6405722	762	0 7138	0 6777	0 2504	0 2485	-0 0775	0 3226
27	106 892247	-49 6357357	752	-0 2114	0 2707	-0 5662	0 5081	0 1956	8 6761
28	107 307766	-49 6296876	708	0 3060	0 2451	-0 2956	0 2729	-0 3288	0 6944
29	106 913233	-49 6750313	627	-0 2564	0 2548	-0 6345	1 5920	0 1208	1 4202
30	107 107413	-49 5321284	616	-0 0203	0 2147	-0 2425	0 2476	0 4794	0 9011
31	107 400028	-49 6042995	615	0 0814	0 2806	-0 4712	0 3152	-0 6403	38 1139
32	107 047397	-49 5810711	605	-0 4580	0 1379	-0 4221	0 3588	-0 1136	0 9980
33	107 172551	-49 6813855	601	0 1016	0 2930	-0 0021	0 3248	0 3053	0 3727
34	107 055947	-49 5510321	584	0 7552	0 2619	0 1640	0 1460	0 0449	0 1681
35	107 348027	-49 4220585	570	0 2361	0 2706	-0 1543	0 3085	-0 0173	0 8091
36	107 078048	-49 6603585	569	0 5805	0 2846	-0 1612	0 2680	-0 4231	0 7801
37	107 2039121	-49 46863651	502	0 0867	0 2863	-0 1230	0 3183	-0 2783	3 3451
38	107 257388	-49 4338548	498	0 0978	0 3047	0 1853	0 2748	0 4586	0 1942
39	107 474705	-49 5498484	495	0 6631	0 3301	0 1606	0 2772	-0 2787	0 4218
40	107 352334	-49 4440796	493	0 7354	0 4288	0 0585	0 3147	-0 1182	0 4396
41	107 248484	-49 4414658	481	-0 1089	0 2010	0 0303	0 2668	0 0136	1 4984
42	107 144946	-49 6841879	474	0 1468	0 3166	0 0381	0 2874	0 1663	0 5390
43	107 202510	-49 4202052	470	0 1062	0 2716	-0 2535	0 3362	-0 3385	0 8566
44	106 981307	-49 4198100	470	0 2401	0 3071	-0 2049	0 3096	-0 2215	0 6494
45	106 963710	-49 5169105	467	0 0105	0 4604	-0 2051	0 3431	-0 1677	0 9090
46	107 421194	-49 4343036	465	0 1494	0 3295	-0 3003	0 3547	0 0008	0 9133
47	107 213174	-49 4240109	456	0 3114	0 3119	-0 1561	0 3253	-0 1787	0 6206
48	107 351757	-49 6084572	456	-0 5862	0 1921	-0 7936	0 6909	0 4830	40 8717

cont

Table A 1

Source	RA [Deg]	Dec [Deg]	Weighted Source Counts	HR_1	HR_1 error	HR_2	HR_2 error	HR_3	HR_3 error
49	107 412668	-49 4921120	445	-0 3933	0 2652	-0 4235	0 4877	0 2107	2 5046
50	107 272969	-49 4531653	427	0 2655	0 3846	-0 1606	0 3154	0 5796	0 3635
51	106 808847	-49 6246738	417	0 1449	0 4165	0 1083	0 4173	0 6040	0 1702
52	107 206729	-49 4480411	416	0 2771	0 3142	-0 0149	0 2930	0 1671	0 3017
53	107 458463	-49 5260339	413	0 0999	0 2881	-0 1352	0 3663	0 0141	0 5722
54	107 036805	-49 4942171	410	0 0344	0 2243	-0 4571	0 3733	-0 0435	0 9185
55	107 237923	-49 5040959	409	0 0671	0 1938	-0 4622	0 3035	-0 1186	1 8187
56	106 907481	-49 3867297	400	-0 2883	0 2728	-0 6887	0 3994	-0 4585	37 5096
57	107 040739	-49 5345594	395	0 0210	0 1912	-0 5791	0 3764	0 5140	95 6746
58	106 991222	-49 5741208	389	0 7063	0 3483	-0 0098	0 2509	-0 0635	0 4496
59	107 108696	-49 6728244	365	0 4755	0 3584	-0 1195	0 3670	0 0024	0 4950
60	107 256840	-49 6024525	359	0 1885	0 2463	-0 1326	0 2501	-0 2833	0 6376
61	107 265893	-49 4683099	358	-0 0459	0 2800	0 3271	0 3034	0 1715	0 2881
62	107 303437	-49 3352696	357	0 4447	0 3130	-0 3089	0 3064	-0 0978	0 6994
63	107 080274	-49 5866241	357	0 0555	0 1868	-0 3182	0 2427	-0 2961	0 4794
64	107 003887	-49 5740283	347	0 0010	0 3885	0 0283	0 3275	-0 2166	0 9615
65	107 383812	-49 5903539	344	-0 1746	0 2415	-0 8090	0 3400	0 0878	110 5190
66	107 074405	-49 7096030	343	0 3699	0 4259	0 0400	0 3176	-0 0933	0 5569
67	107 071880	-49 5446207	325	0 3447	0 3060	-0 0541	0 2637	-0 2601	0 5352
68	107 394802	-49 4073014	322	0 2784	0 3570	-0 1097	0 3352	-0 0562	1 2401
69	107 279452	-49 5851374	321	-0 3177	0 1866	-0 4527	0 3964	-0 3143	4 2371
70	107 232454	-49 5909462	317	0 1382	0 1964	-0 4454	0 3050	-0 3374	1 2242
71	106 928072	-49 4900249	315	0 2048	0 2775	-0 4633	0 2828	-0 2208	0 7297
72	107 393237	-49 6189815	314	0 1657	0 3456	-0 2703	0 4692	-0 0450	0 9647

cont

Table A 1

Source	RA [Deg]	Dec [Deg]	Weighted Source Counts	HR_1	HR_1 error	HR_2	HR_2 error	HR_3	HR_3 error
73	107 162457	-49 4692742	309	0 5183	0 4882	0 1059	0 2805	-0 0132	0 3019
74	107 360221	-49 4845674	301	0 3479	0 3372	-0 0377	0 3245	-0 1406	0 5182
75	107 104692	-49 4279490	300	0 2000	0 5902	0 1981	0 3687	0 0984	0 4123
76	107 371581	-49 4354736	298	-0 1177	0 2625	-0 1108	0 3420	-0 2343	0 8750
77	107 259193	-49 3835255	295	-0 0704	0 3650	-0 2795	0 4272	0 1678	4 1095
78	107 026041	-49 3961538	290	-0 2646	0 2540	-0 5753	0 5281	-0 4445	5 1381
79	107 033099	-49 6046158	286	0 2344	0 1882	-0 3822	0 2452	-0 4411	0 7530
80	107 385363	-49 4326744	284	-0 5222	0 2964	-0 5242	1 2769	0 4984	3 5187
81	107 083560	-49 4032289	283	0 3212	0 3024	-0 0884	0 2985	-0 2058	0 5486
82	107 142563	-49 7569272	277	0 1391	0 2918	-0 3285	0 3453	-0 1634	1 1894
83	107 460472	-49 6222647	273	0 2748	0 2927	-0 3114	0 3359	-0 2875	1 9311
84	107 449104	-49 4433517	270	-0 0690	0 3150	-0 2319	1 1345	-0 0562	0 8293
85	107 258915	-49 6518586	263	0 1846	0 3077	-0 1214	0 3844	0 1158	0 4426
86	107 348069	-49 5689305	262	0 3303	0 2397	-0 4494	0 3195	-0 0731	1 0349
87	107 448787	-49 4639019	259	0 6540	0 2869	-0 0997	0 2930	-0 0130	0 4394
88	106 987406	-49 5917839	258	0 0877	0 4111	0 4455	0 6391	0 4963	0 2446
89	107 274700	-49 7115792	256	0 2044	0 3261	-0 2524	0 3748	-0 0758	2 1349
90	106 902322	-49 6066684	252	-0 4840	0 2832	-0 2694	1 1163	-0 0230	5 2936
91	107 083455	-49 7318201	246	0 1226	0 3410	-0 1352	0 3548	0 1576	0 6410
92	107 186495	-49 7590959	242	-0 2151	0 4178	0 4598	0 3292	-0 4535	0 5445
93	107 334477	-49 3373234	228	0 3551	0 3487	-0 0345	0 3366	-0 5690	0 9923
94	107 120131	-49 5060559	227	0 1134	0 4292	0 0326	0 2772	-0 6142	0 6685
95	107 353521	-49 4631100	220	0 3940	0 5283	0 2411	0 3238	-0 2020	0 4805
96	107 272352	-49 6620477	219	0 1093	0 3411	-0 2097	0 4542	-0 3878	0 9095

cont

Table A 1

Source	RA [Deg]	Dec [Deg]	Weighted Source Counts	HR_1	HR_1 error	HR_2	HR_2 error	HR_3	HR_3 error
97	107 201547	-49 7236562	208	0 1696	1 3521	-0 3165	1 0530	-0 4989	1 5758
98	107 474175	-49 4294780	208	0 4996	0 4969	0 1754	0 3711	-0 1423	0 4938
99	107 185866	-49 6102316	203	0 0810	0 2784	-0 0776	0 2878	-0 2440	0 5465
100	107 374805	-49 4084686	197	0 1486	0 3445	-0 0747	0 3726	0 1147	0 5765
101	107 431906	-49 4676746	195	-0 0612	0 4830	0 0784	0 4971	-0 0052	0 5492
102	106 998468	-49 6262241	191	0 1870	0 3294	-0 1836	0 4493	-0 0496	0 8962
103	107 126957	-49 3679953	183	-0 0198	0 2813	-0 6709	0 3314	-0 2928	2 8029
104	107 259498	-49 3869492	179	0 2478	0 3342	-0 2130	0 5940	0 5847	0 4154
105	107 104304	-49 5986956	177	0 0482	0 2544	-0 1254	0 2867	-0 8873	1 4138
106	107 345403	-49 5603907	176	0 2632	0 6828	-0 1211	0 3744	0 1818	0 6585
107	107 433168	-49 4365032	171	0 2996	0 3485	-0 3309	0 3403	-0 5631	1 0137
108	107 409175	-49 7347362	167	0 3684	0 2946	-0 1702	0 3355	-0 1061	0 6786
109	107 378794	-49 6627794	167	0 0671	0 3784	-0 2313	0 3594	-0 1370	0 5437
110	107 274871	-49 3218707	164	-0 0955	0 4753	-0 1151	0 3766	-0 1778	1 4821
111	107 500615	-49 4997731	162	0 8015	0 2668	0 0701	0 3162	-0 3492	0 5127
112	107 385252	-49 6340683	161	0 2285	0 2963	-0 4269	0 3208	-0 0535	0 5708
113	107 414893	-49 6233085	159	0 8224	0 2556	0 1728	0 3229	-0 3595	0 4706
114	107 146518	-49 7601385	158	0 3747	0 3341	-0 4156	0 3830	0 0495	0 9015
115	107 401468	-49 6833973	150	0 0253	0 3363	-0 1282	0 4066	-0 1895	1 3970
116	106 858097	-49 4987047	145	0 1836	1 0400	-0 0783	0 5994	0 6198	0 1942
117	107 279217	-49 4057774	144	0 4061	0 3567	-0 2962	0 3384	0 0598	0 6306
118	107 363142	-49 7026593	124	0 7929	0 2518	-0 1760	0 4347	0 2260	0 6068
119	107 084921	-49 3187051	124	0 8638	0 1456	-0 7592	0 1993	0 6569	0 3299
120	106 964169	-49 4273139	120	-0 5033	0 2988	-0 2137	0 7651	0 2155	1 0432

cont

Table A.1

Source	RA [Deg]	Dec [Deg]	Weighted Source Counts	HR_1	HR_1 error	HR_2	HR_2 error	HR_3	HR_3 error
121	107.381413	-49.3661123	103	0.1530	0.3066	-0.5784	0.6191	-0.6103	28.9297
122	107.205511	-49.7337116	101	0.5322	0.5129	0.8308	0.3659	0.0558	0.3962
123	107.357720	-49.6730857	99	0.1645	0.2861	-0.2355	0.4104	0.1519	0.7713
124	107.053066	-49.6392736	99	-0.7847	0.3557	0.2473	0.6669	0.2326	0.7392
125	107.315047	-49.7132402	91	0.8603	0.1187	-0.3064	0.3430	-0.2680	0.8354
126	107.054485	-49.6354384	91	0.1115	0.4224	-0.3850	0.8521	0.2726	0.4248
127	107.424717	-49.6640634	89	-0.0558	0.3694	-0.2772	0.4503	-1.0000	1.8858
128	107.136895	-49.4207405	88	0.3090	0.5675	0.4927	0.4120	-0.2978	0.6763

Appendix B

Source Best Fit Models

In Table B.2 we show the best fit models of the brightest 30 sources. The columns are as follows: Column 1 shows the *XMM-Newton* source number from the *XMM-Newton* Science Archive[1]. All have the prefix "2XMM". Column 2 is the source number used for this work. Columns 3 - 4 show the source right accession and declination in degrees, respectively. Column 5 shows the source weighted counts in energy range 0.5-12 keV. Column 6 shows the best-fit model(s) with * indicating multiplication. All models include Galactic $N_H = 0.0431 \times 10^{22}$ cm^{-2} unless marked with †. If marked with "none", an acceptable spectrum was unable to be produced. The *Xspec* terms are defined in Table B.1. Column 7 shows the model(s) best-fit reduced chi-squared. Column 8 shows the degrees of freedom defined as the number of channels minus the number of model parameters (Arnaud et al., 2010). Columns 9 and 10 show the total flux for the 0.5-12 keV energy range for the pn and MOS cameras, respectively.

Model	*Xspec* Term
Photon Absorption	phabs
Power Law	po
Mekal	mekal
Blackbody	bb
Bremsstrahlung	brem
Gaussian	gaus
Ionized Absorber	absorbi
Gaussian Absorption Line	gabs
Cyclotron Absorption Line	cyclabs

Table B.1: *Xspec* Terms

[1] http://xmm.esac.esa.int/xsa/

Table B.2: Source Models

(1)	(2)	(3)	(4)	(5)	(6)	(7)	(8)	(9)	(10)
XMM-Newton Source Name	Source	RA [Deg]	DEC [Deg]	Weighted Counts	Model	χ^2_ν	dof	pn Flux $\times10^{-14}$ [erg/cm^2/s]	MOS Flux $\times10^{-14}$ [erg/cm^2/s]
J070820.1-494251	2	107.08308	-49.71418	5930	phabs*po	0.3458	154	15.500	18.3900
J070859.8-493754	3	107.24877	-49.63270	2048	phabs*po	0.2980	24	2.9979	–
J070859.8-493754	4	106.83617	-49.58429	1772	phabs*po	0.8132	40	2.8747	3.9362
					bb	0.7422	41	2.5714	3.7079
J070720.7-493454	5	107.15877	-49.71931	1714	phabs*po	0.1490	27	–	5.9180
					phabs*mekal	0.1310	26	–	3.8610
	6	107.19497	-49.30467	1461	none	–		–	–
J070843.0-493950	7	107.17887	-49.66414	1421	phabs*po	0.0752	16	–	1.2005
					bb+po	0.0749	15	–	4.0407
J070907.3-493333	8	107.28150	-49.55945	1388	none	–		–	–
J070907.3-493333	9	107.02767	-49.53019	1383	phabs*po	0.1100	6	0.2739	–
					bb	0.1200	7	0.2555	–
J070806.6-493148	10	107.10536	-49.63080	1374	phabs*po	0.4646	29	0.6520	–
J070825.2-493751	11	107.17085	-49.38741	1252	phabs*po	0.3930	16	4.0965	–

cont

Table B.2

(1) XMM-Newton Source Name	(2) Source #	(3) RA [Deg]	(4) DEC [Deg]	(5) Weighted Counts	(6) Model	(7) χ^2_ν	(8) dof	(9) pn Flux $\times 10^{-14}$ [erg/cm^2/s]	(10) MOS Flux $\times 10^{-14}$ [erg/cm^2/s]
J070841.0-492314	12	107.34916	-49.49287	1233	phabs*po	1.9170	33	0.4447	0.8726
					bb	1.8490	34	0.4733	0.8533
J070923.8-492934	13	107.12498	-49.42425	1230	phabs*po	0.1500	11	2.3111	–
					bb+po	0.2000	10	3.0269	–
J070922.0-492207	14	107.34234	-49.36852	1188	phabs*po	0.4292	24	5.1678	1.6265
					phabs*mekal	0.4391	23	4.6688	1.6036
					bb+po	0.5023	22	6.5133	2.2540
J070922.0-492207	15	107.10341	-49.54056	1166	none	–		–	–
J070824.9-493224	16	107.00076	-49.71804	1155	none	–		–	–
J080800.2-494303	17	107.29532	-49.51575	1129	none	–		–	–
J070910.8-493056	18	107.10191	-49.52220	1069	none	–		–	–
J070923.7-493810	19	107.35624	-49.63635	1033	phabs*po	0.1480	12	–	2.1285
					bb+po	0.1820	11	–	2.8027
J070923.7-493810	20	107.30016	-49.50657	934	phabs*po	0.3610	6	0.3515	–
					phabs*mekal	0.7870	5	0.7363	–

cont

Table B.2

(1) XMM-Newton Source Name	(2) Source #	(3) RA [Deg]	(4) DEC [Deg]	(5) Weighted Counts	(6) Model	(7) χ^2_ν	(8) dof	(9) pn Flux $\times10^{-14}$ [erg/cm^2/s]	(10) MOS Flux $\times10^{-14}$ [erg/cm^2/s]
J070809.3-492230	21	107.03869	-49.37499	890	none	–		–	–
J070809.3-492230	22	107.11474	-49.38802	886	bb	0.5447	23	22.0660	–
					†absori*(bb+po)	0.3520	19	55.2240	–
					†gabs*(bb+brem)	0.4943	21	27.0270	–
					†cyclab*(bb+brem)	0.425	22	36.8590	–
J070827.6-492317	23	107.18769	-49.74023	838	none	–		–	–
J070845.0-494424	24	107.01216	-49.36236	872	phabs*po	0.1300	6	55.8930	–
					phabs*mekal	0.1300	5	52.9690	–
J070802.8-492147	25	107.01448	-49.56704	771	none	–		–	–
J070803.7-493402	26	107.45657	-49.64057	762	bb	0.1480	7	–	8.3948
					†gaus	0.3290	9	–	3.5816
J070949.6-493826	27	106.89225	-49.63574	752	†gaus	0.6461	16	11.9650	15.7670
					†gaus+bb	0.7938	13	13.9250	13.0910
J070913.90493747	28	107.30777	-49.62969	708	phabs*po	0.0930	10	–	0.6103
					phabs*mekal	0.0930	9	–	0.8023

cont

Table B.2

(1) *XMM-Newton* Source Name	(2) Source #	(3) RA [Deg]	(4) DEC [Deg]	(5) Weighted Counts	(6) Model	(7) χ^2_ν	(8) dof	(9) pn Flux $\times 10^{-14}$ [erg/cm^2/s]	(10) MOS Flux $\times 10^{-14}$ [erg/cm^2/s]
J070913.90493747	29	106.91323	-49.67503	627	phabs*po	1.1400	6	–	0.7000
					phabs*mekal	1.0000	5	–	0.6435
J070739.3-494029	30	107.10741	-49.53213	616	none	–		–	–
J070825.5-493157	37	107.20391	-49.46864	502	phabs*po+gaus	0.494	9	3.3312	–
					†po*gaus	0.577	9	4.5887	–

Appendix C

Source Spectra

All combined pn and MOS spectra have pn as black and MOS as red.

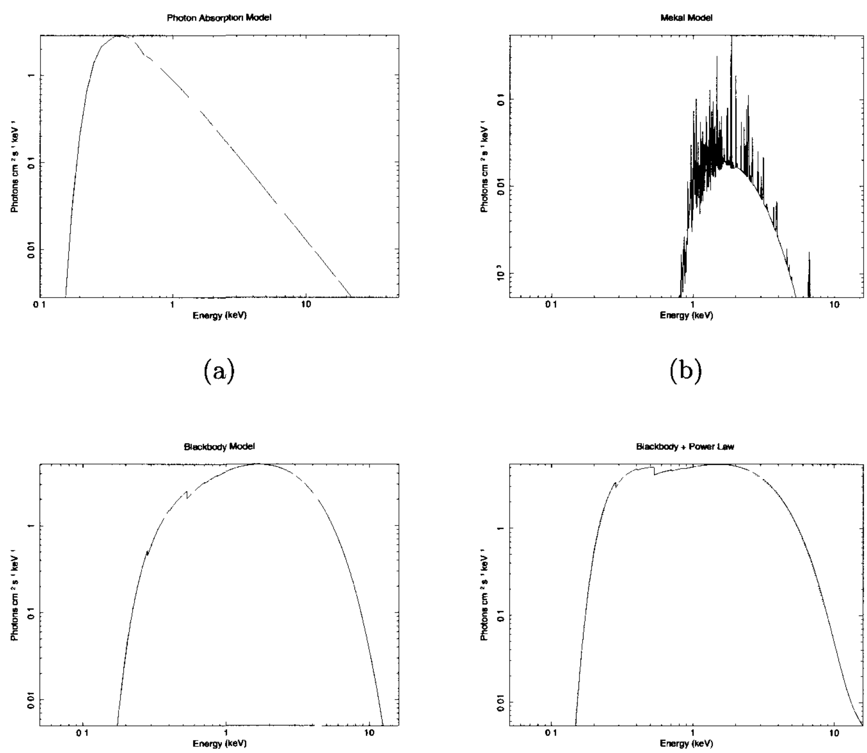

(a) (b) (c) (d)

Figure C.1: Models used for source fitting. All models used a fixed galactic absorption N_H=0.0431$\times 10^{22}$ cm^{-2} and a starting column density of N_H=.01 $\times 10^{22}$ cm^{-2} and photon index = 1.9 then left as a free parameter. **a)** Absorbed power law model. **b)** Mekal model with redshift left as a free parameter and abundance held at the solar value. **c)** Blackbody model with starting kT at 3keV. **d)** Blackbody + Power Law model with the parameters as defined in the initial power law and blackbody models.

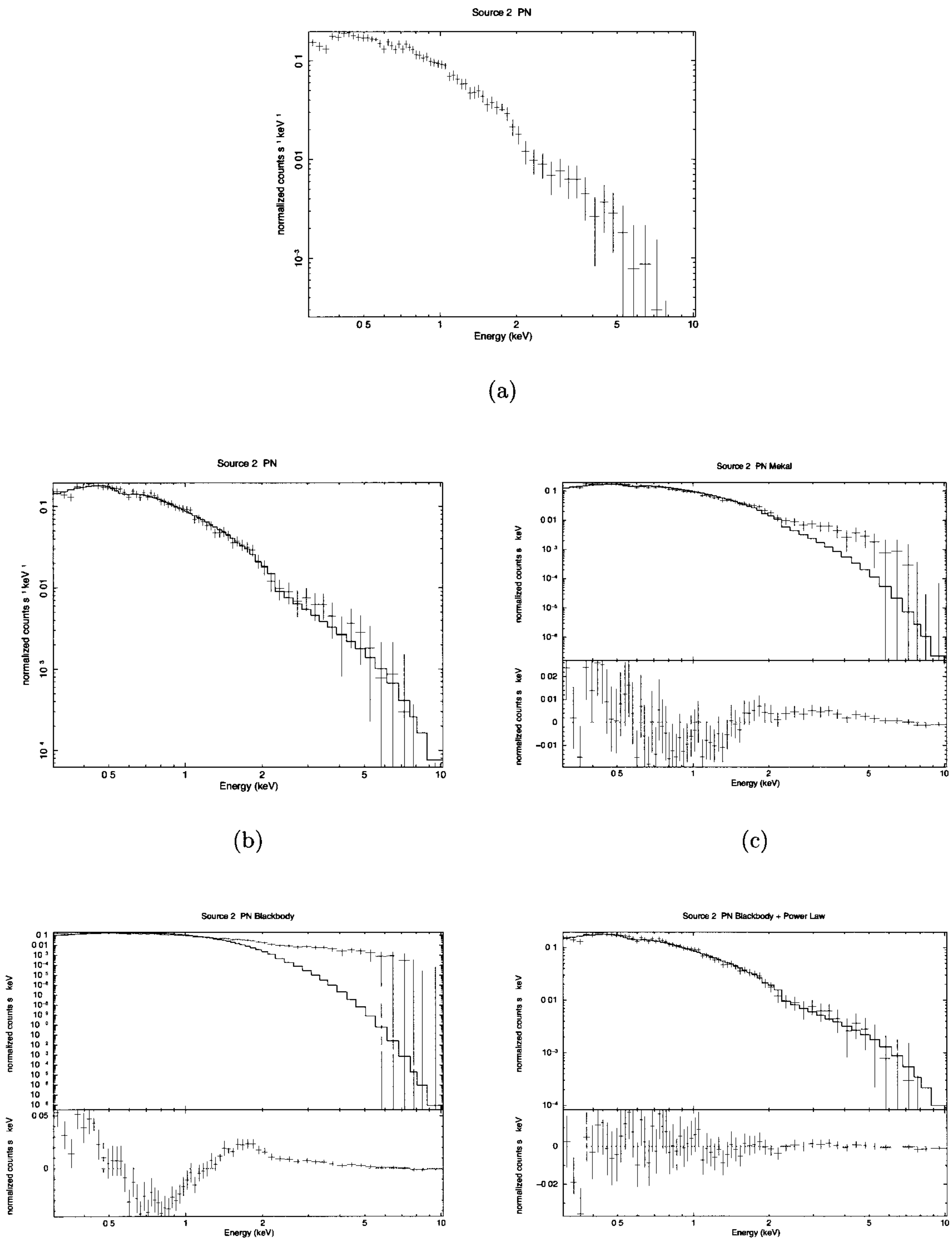

(a) (b) (c) (d) (e)

Figure C.2: **a)** pn spectrum of source 2 w/o models. **b)**Absorbed power law. **c)**Mekal. **d)**Blackbody. **e)**Blackbody + Power Law.

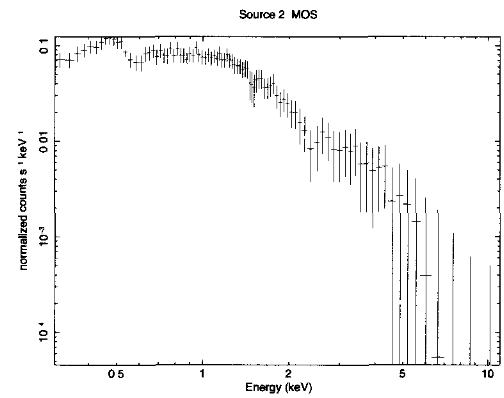

(a)

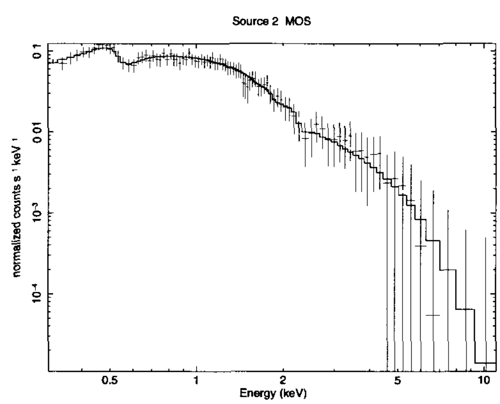

(b)

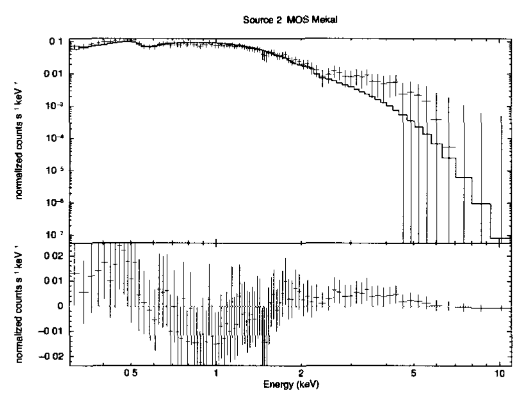

(c)

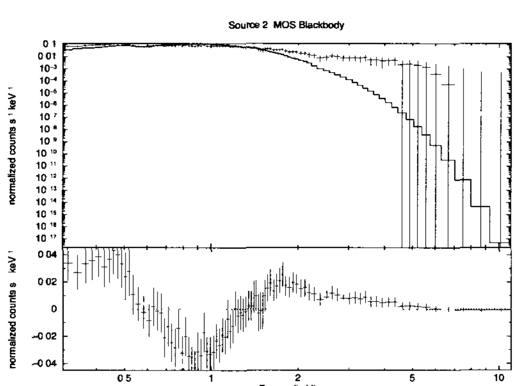

(d)

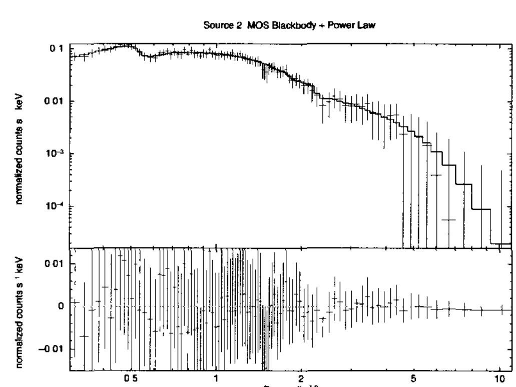

(e)

Figure C.3: **a)** MOS spectrum of source 2 w/o models. **b)**Absorbed power law. **c)**Mekal. **d)**Blackbody. **e)**Blackbody + Power Law.

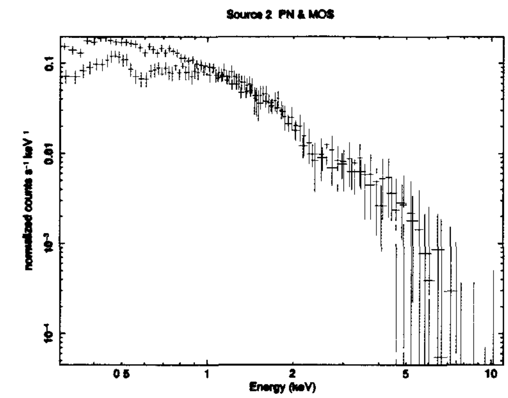

(a)

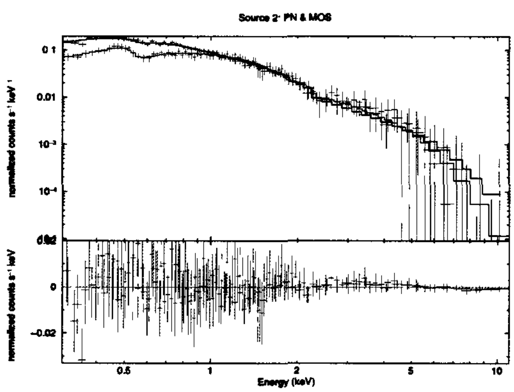

(b)

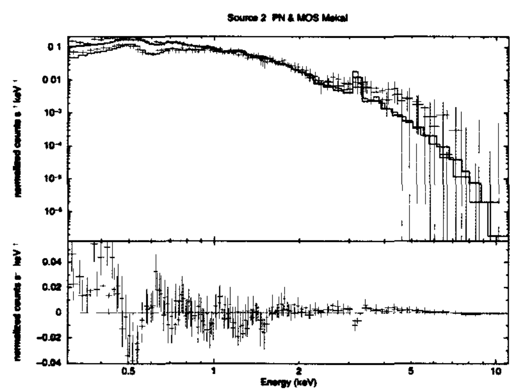

(c)

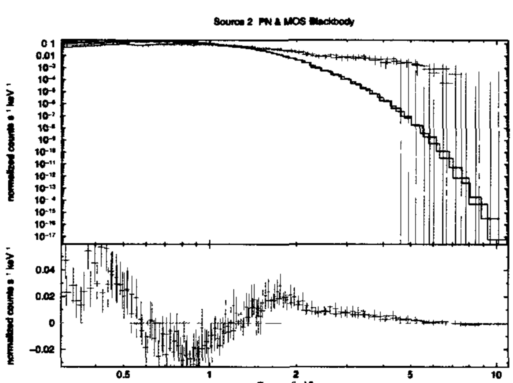

(d)

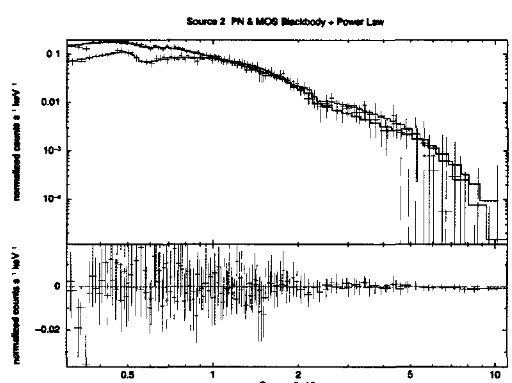

(e)

Figure C.4: **a)** Combined spectrum of source 2 w/o models. **b)**Absorbed power law. **c)**Mekal. **d)**Blackbody. **e)**Blackbody + Power Law.

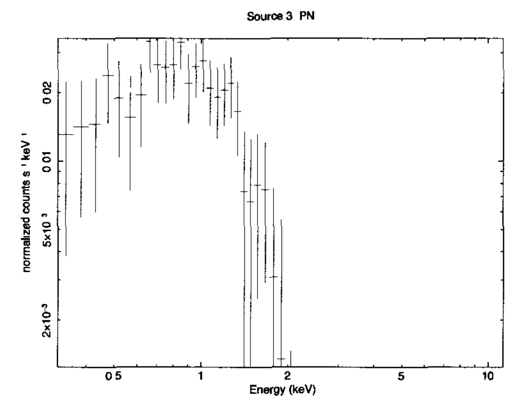

(a)

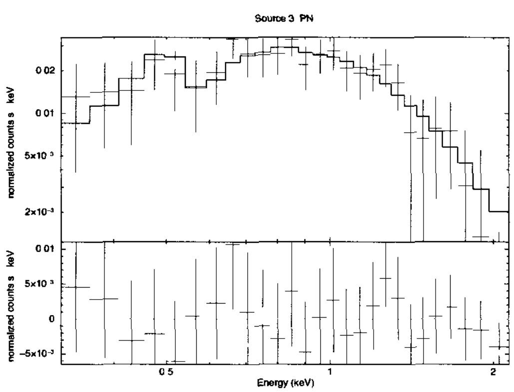

(b)

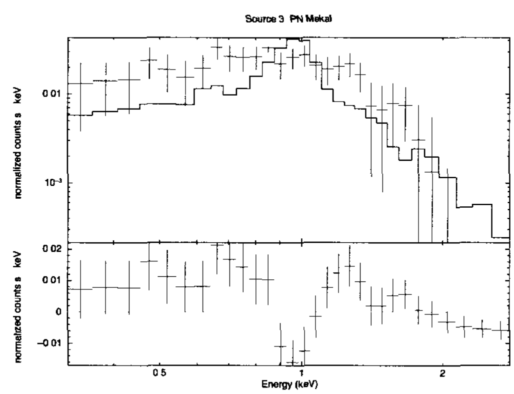

(c)

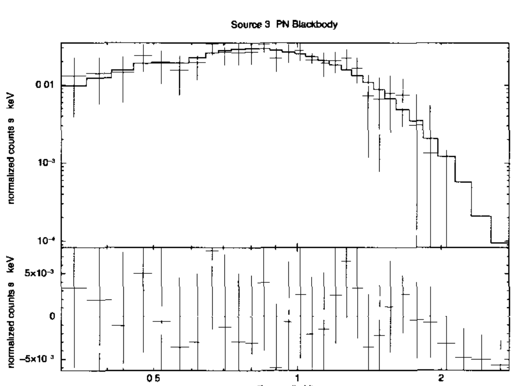

(d)

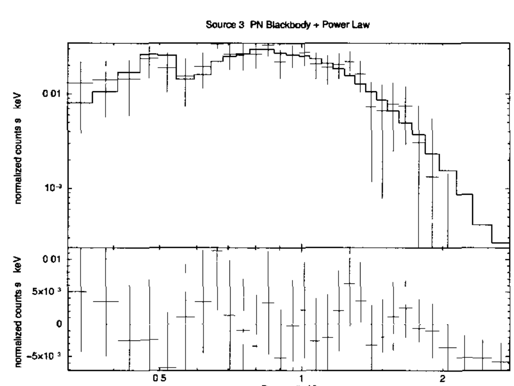

(e)

Figure C.5: **a)** pn spectrum of source 3 w/o models. **b)**Absorbed power law. **c)**Mekal. **d)**Blackbody. **e)**Blackbody + Power Law.

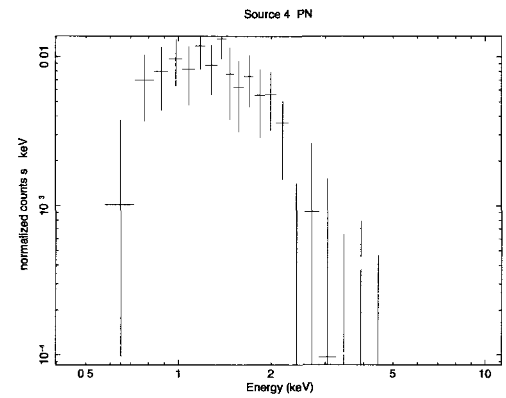

(a)

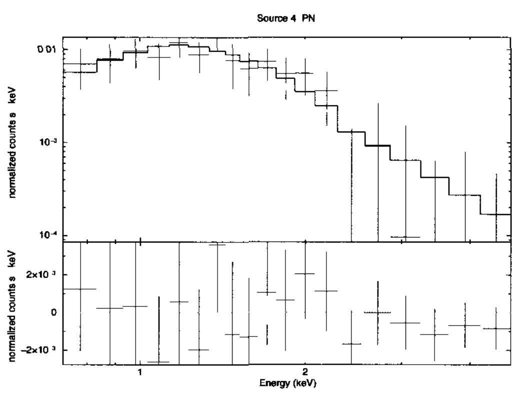

(b)

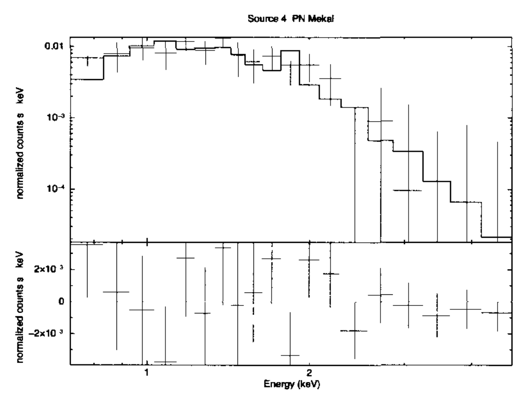

(c)

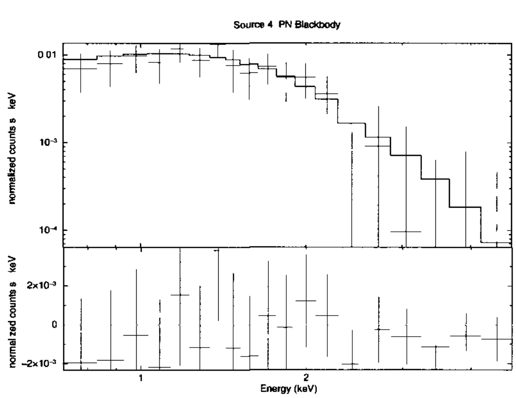

(d)

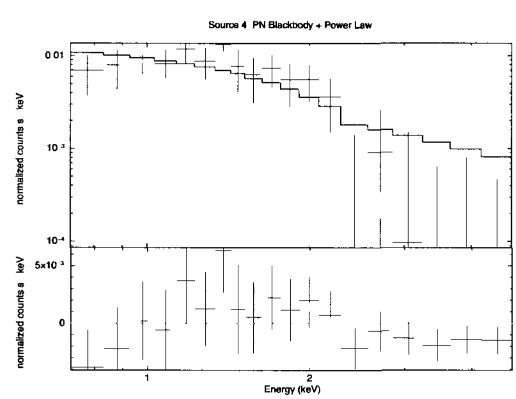

(e)

Figure C.6: **a)** pn spectrum of source 4 w/o models. **b)**Absorbed power law. **c)**Mekal. **d)**Blackbody. **e)**Blackbody + Power Law.

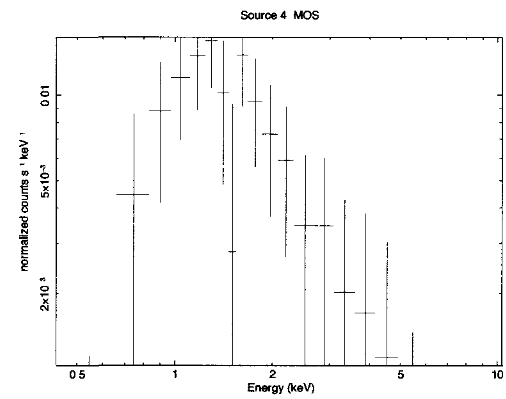

(a)

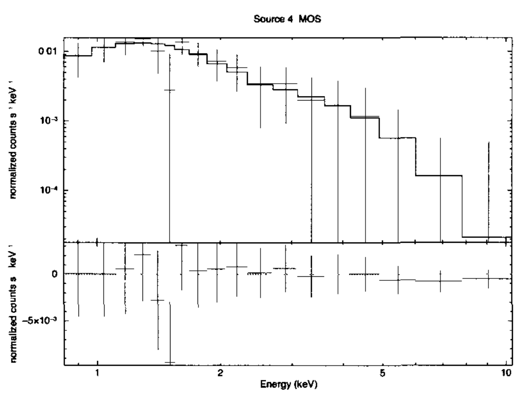

(b)

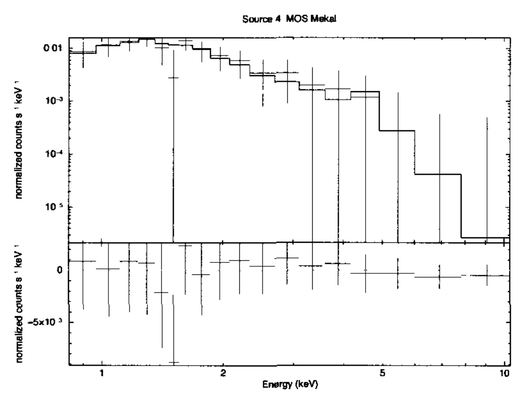

(c)

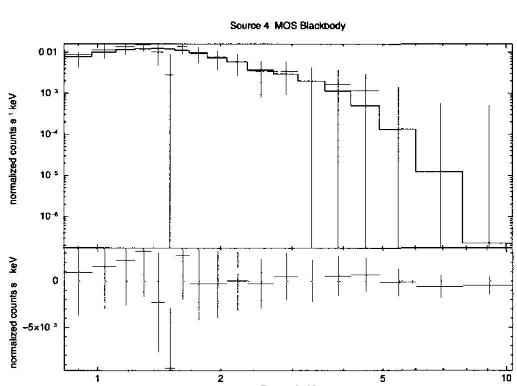

(d)

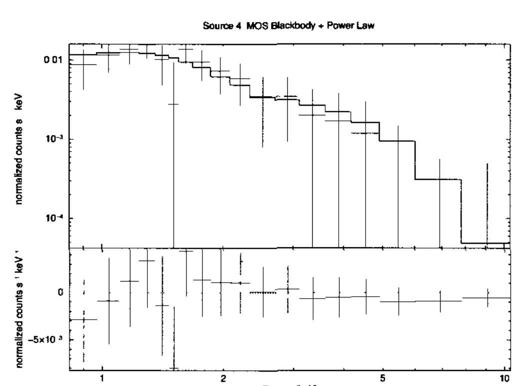

(e)

Figure C.7: **a)** MOS spectrum of source 4 w/o models. **b)**Absorbed power law. **c)**Mekal. **d)**Blackbody. **e)**Blackbody + Power Law.

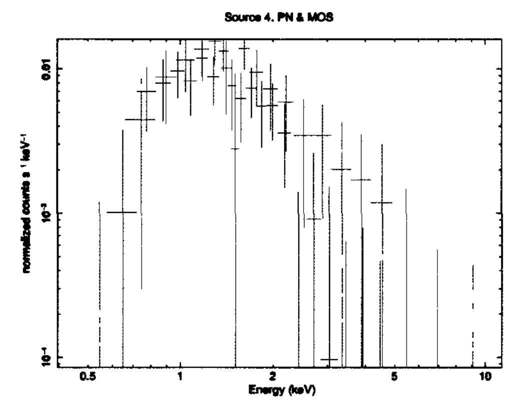

(a)

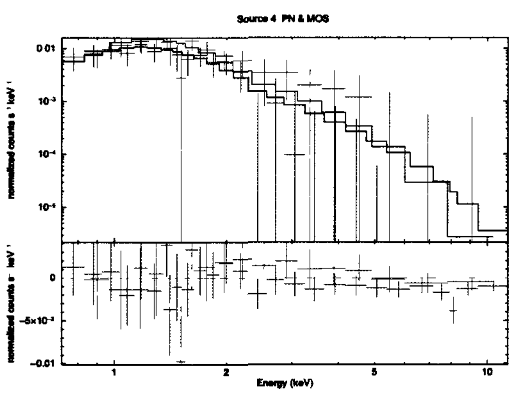

(b)

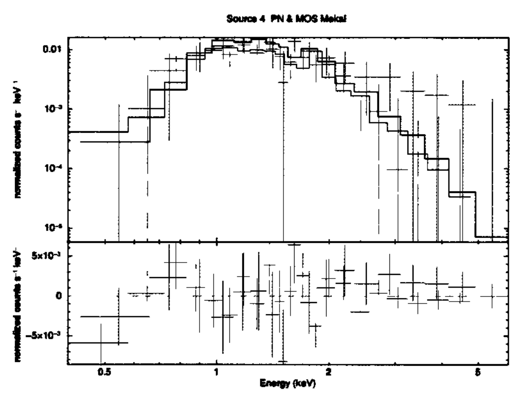

(c)

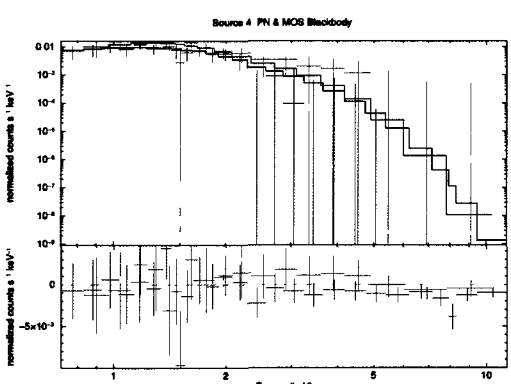

(d)

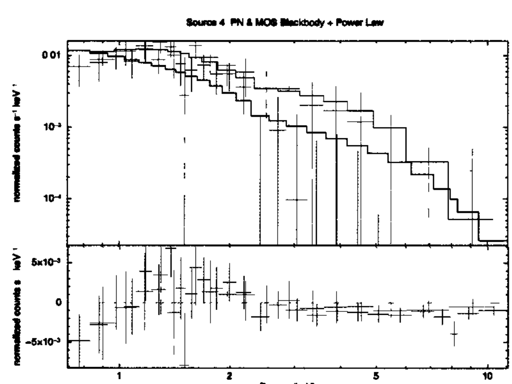

(e)

Figure C.8: **a)** pn and MOS spectra of source 4 w/o models. **b)**Absorbed power law. **c)**Mekal. **d)**Blackbody. **e)**Blackbody + Power Law.

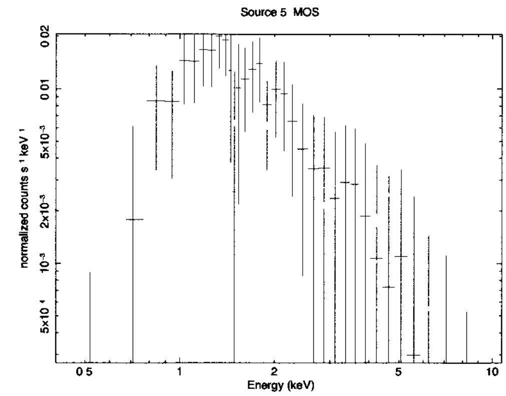

(a)

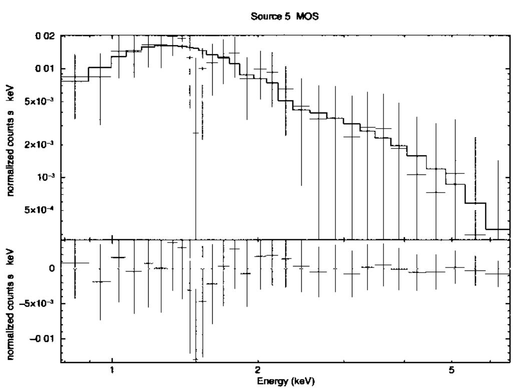

(b)

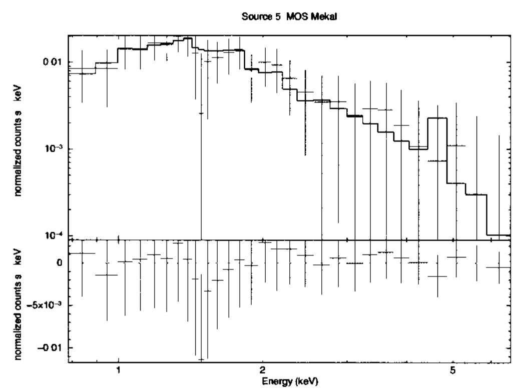

(c)

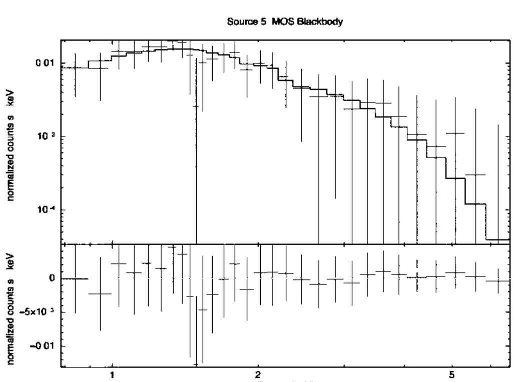

(d)

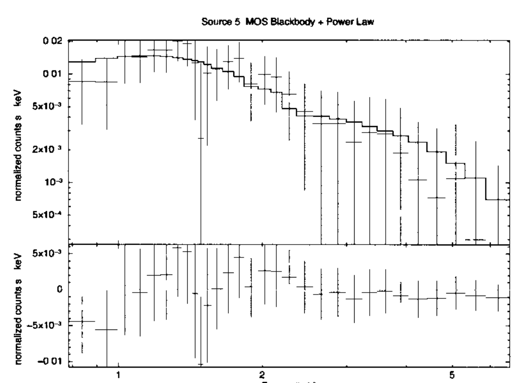

(e)

Figure C.9: **a)** MOS spectrum of source 5 w/o models. **b)**Absorbed power law. **c)**Mekal. **d)**Blackbody. **e)**Blackbody + Power Law.

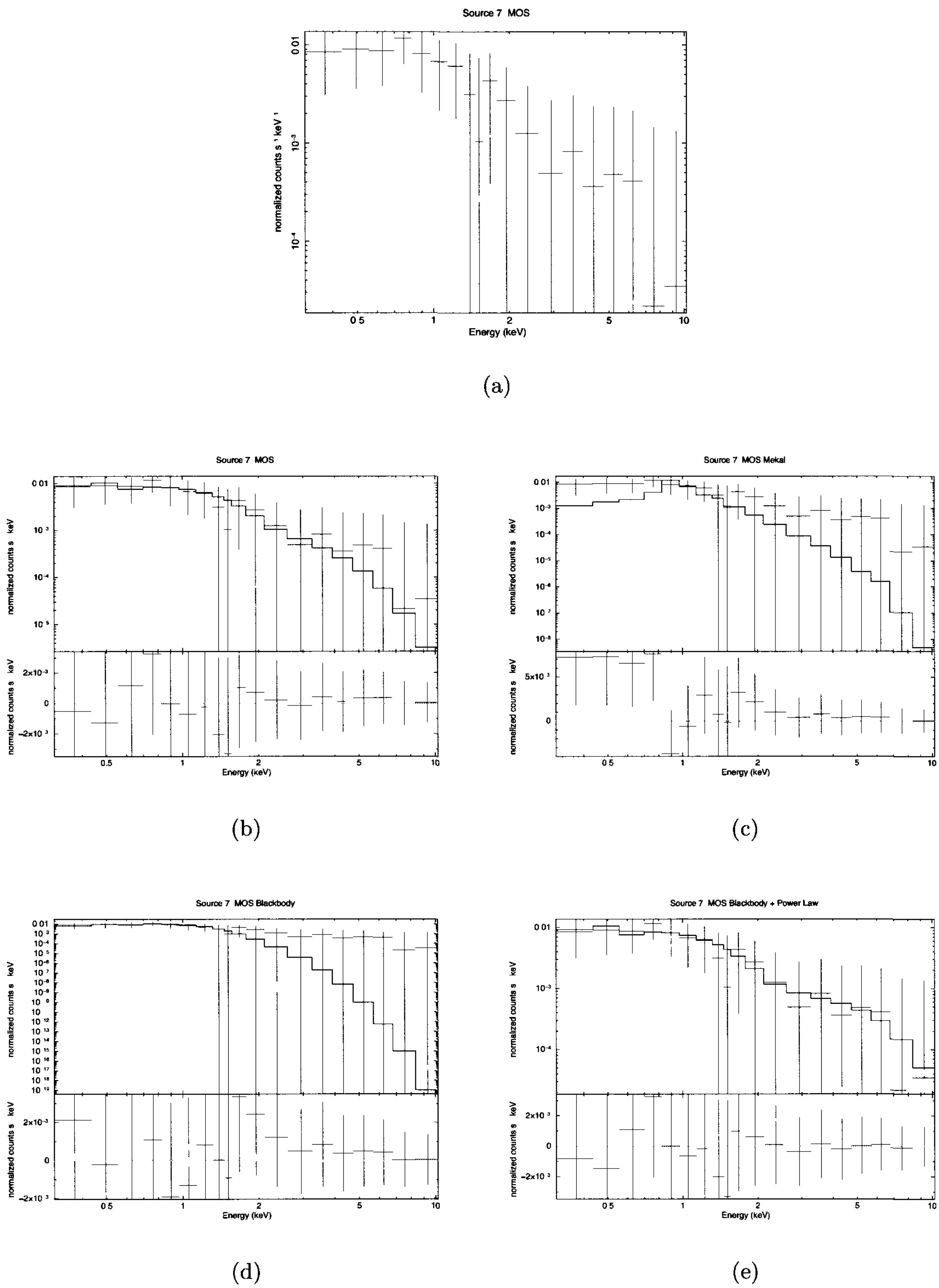

Figure C.10: **a)** MOS spectrum of source 7 w/o models. **b)**Absorbed power law. **c)**Mekal. **d)**Blackbody. **e)**Blackbody + Power Law.

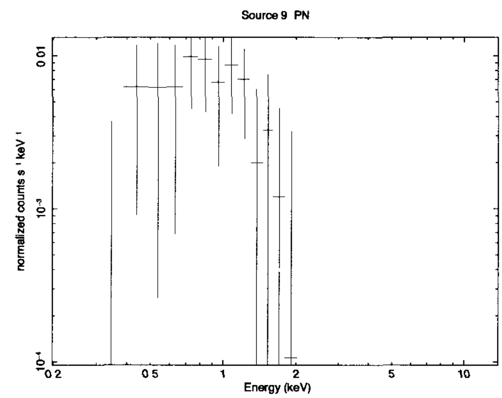

(a)

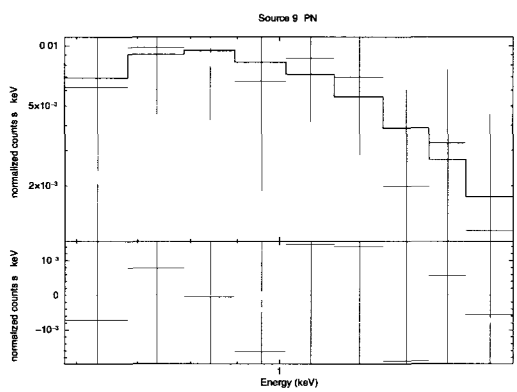

(b)

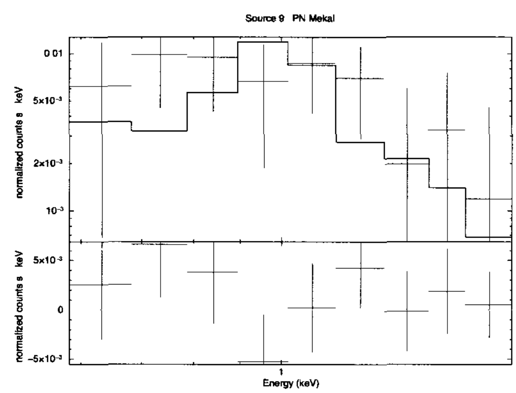

(c)

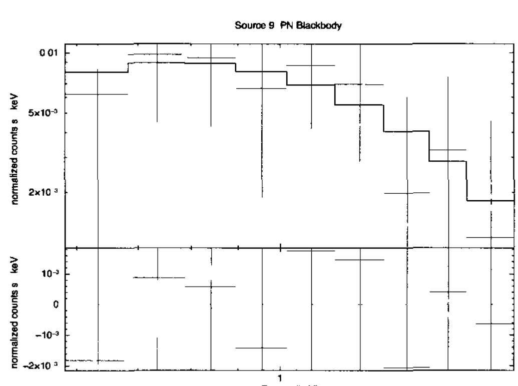

(d)

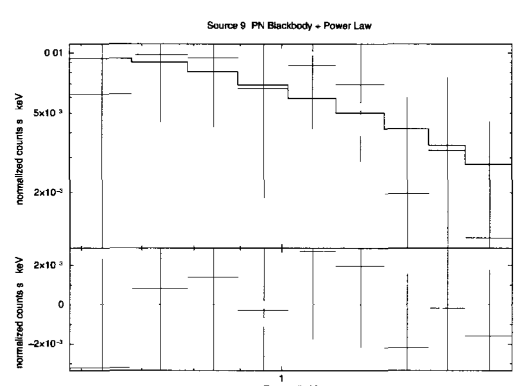

(e)

Figure C.11: **a)** pn spectrum of source 9 w/o models. **b)**Absorbed power law. **c)**Mekal. **d)**Blackbody. **e)**Blackbody + Power Law.

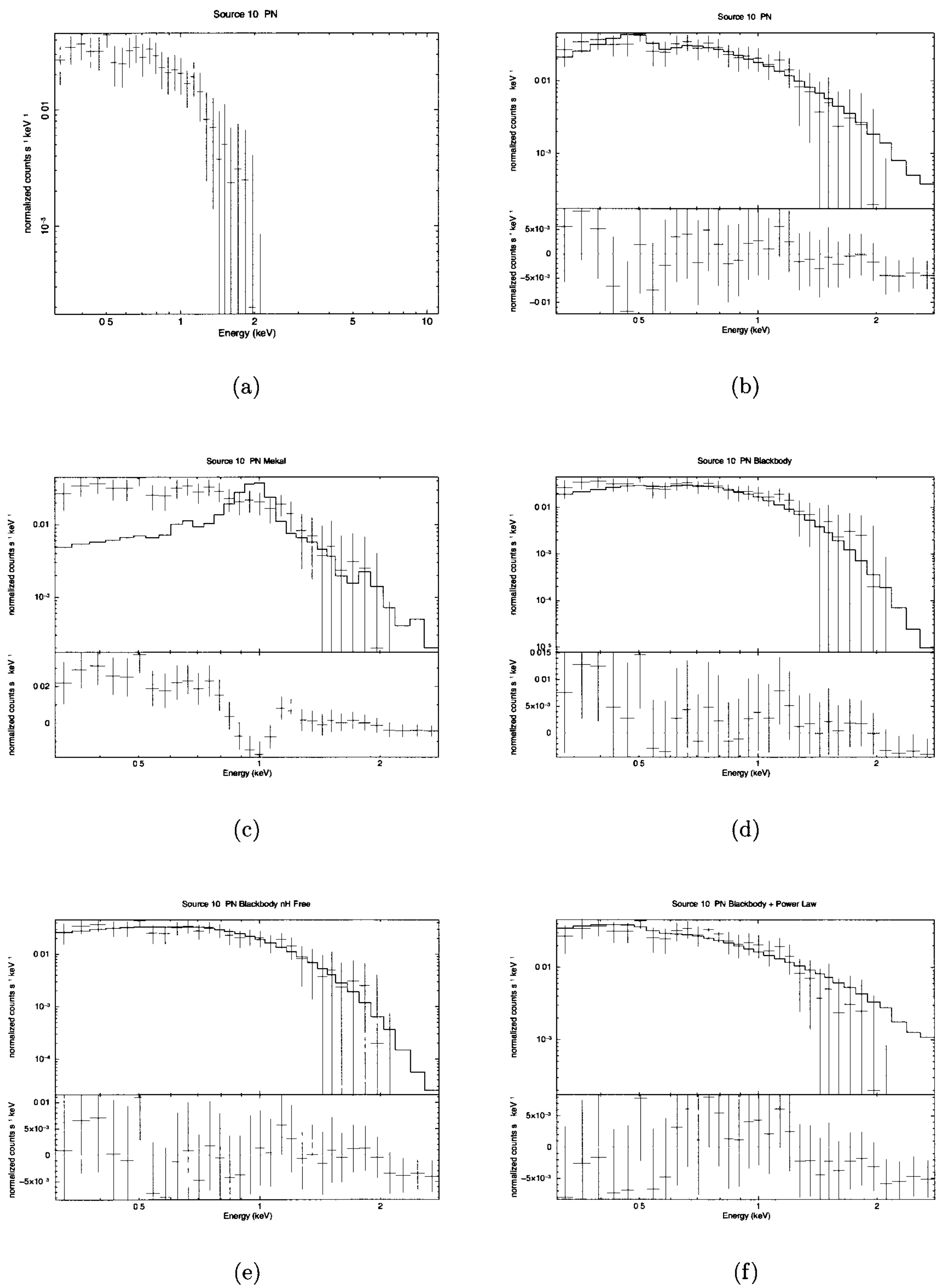

Figure C.12: **a)** pn spectrum of source 10 w/o models. **b)**Absorbed power law. **c)**Mekal. **d)**Blackbody. **e)**Blackbody with N_H is a free parameter. **f)**Blackbody + Power Law.

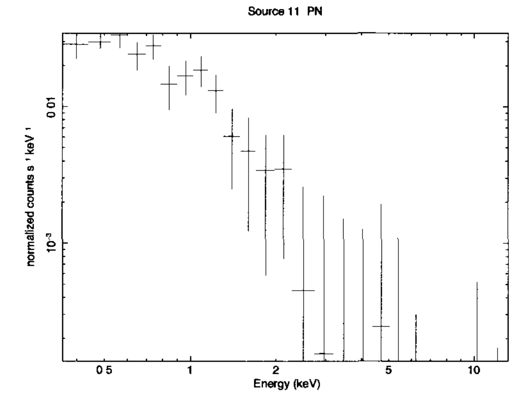

(a)

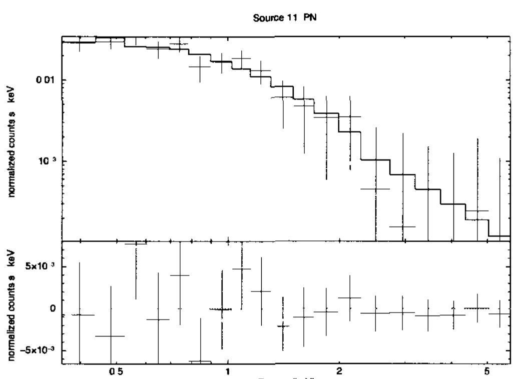

(b)

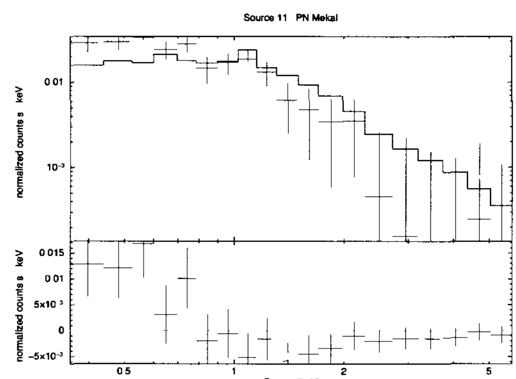

(c)

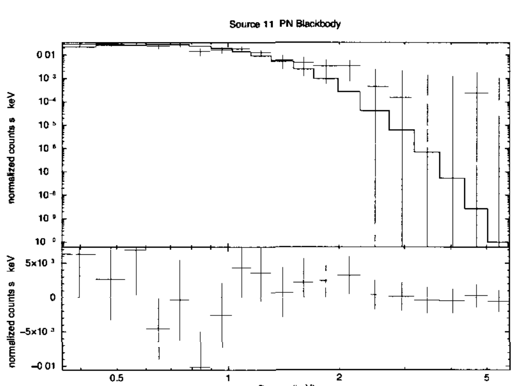

(d)

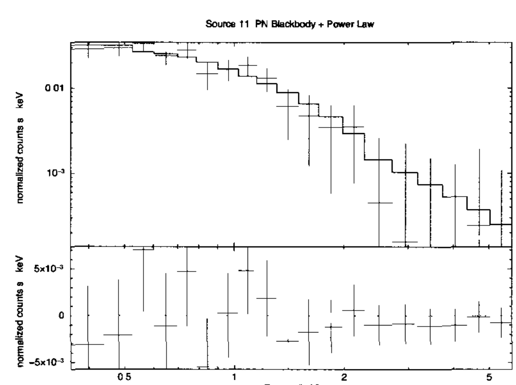

(e)

Figure C.13: **a)** pn spectrum of source 11 w/o models. **b)**Absorbed power law. **c)**Mekal. **d)**Blackbody. **e)**Blackbody + Power Law.

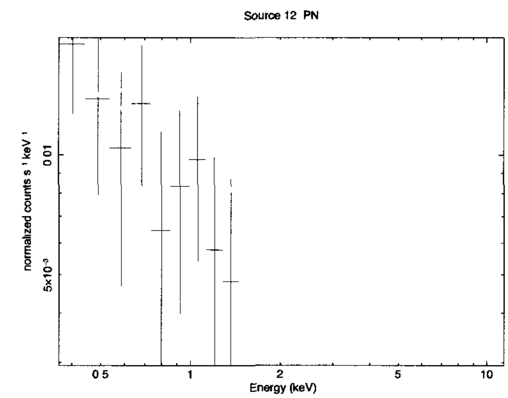

(a)

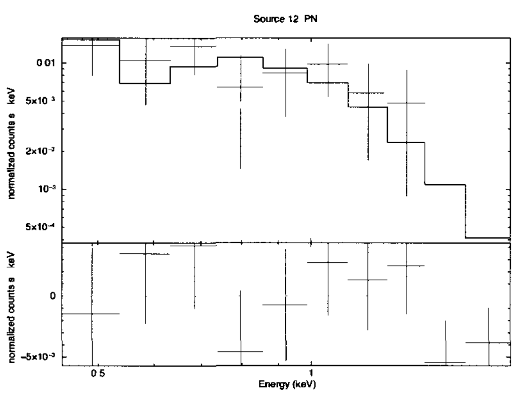

(b)

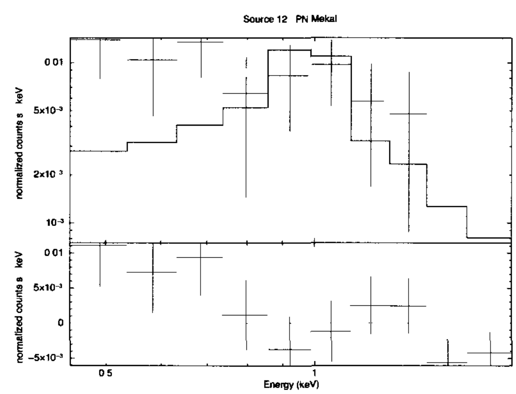

(c)

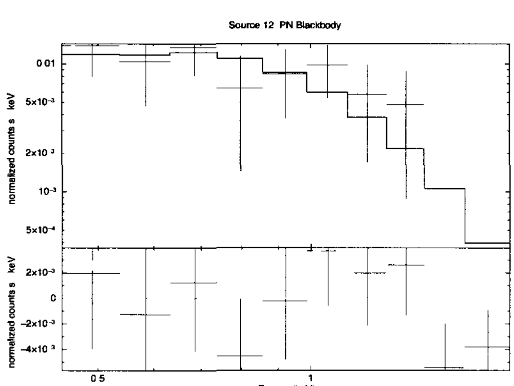

(d)

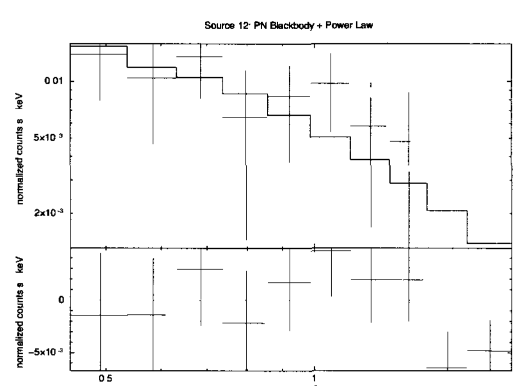

(e)

Figure C.14: **a)** pn spectrum of source 12 w/o models. **b)**Absorbed power law. **c)**Mekal. **d)**Blackbody. **e)**Blackbody + Power Law.

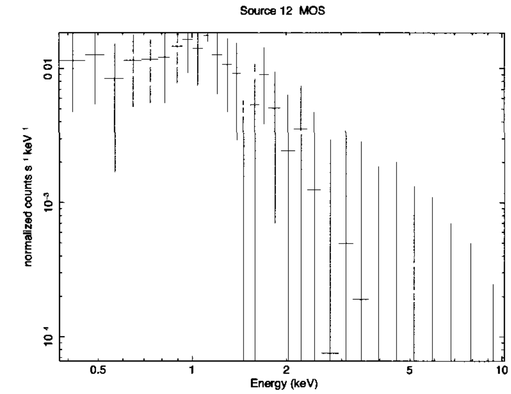

(a)

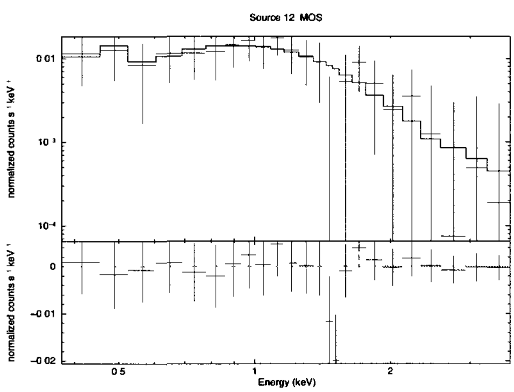

(b)

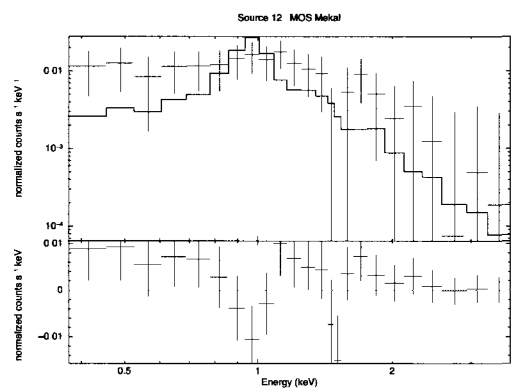

(c)

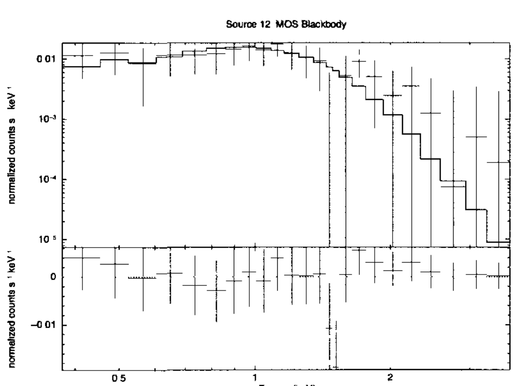

(d)

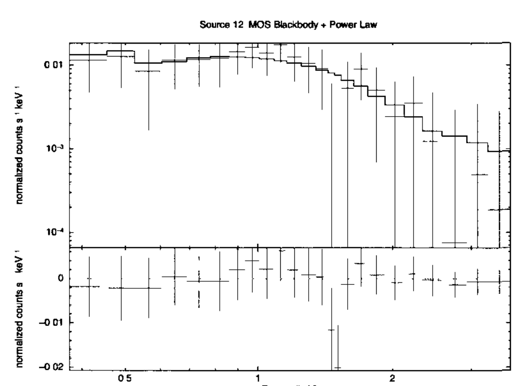

(e)

Figure C.15: **a)** pn spectrum of source 12 w/o models. **b)**Absorbed power law. **c)**Mekal. **d)**Blackbody. **e)**Blackbody + Power Law.

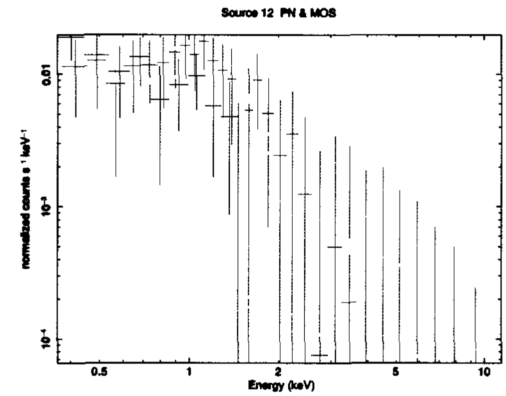

(a)

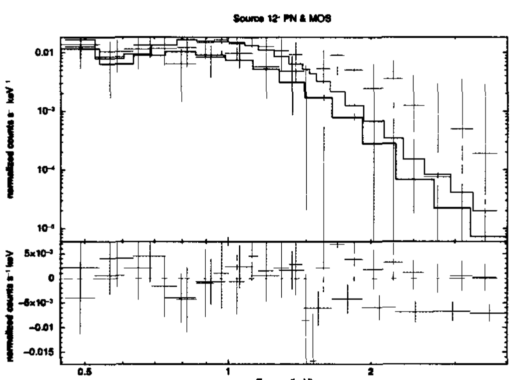

(b)

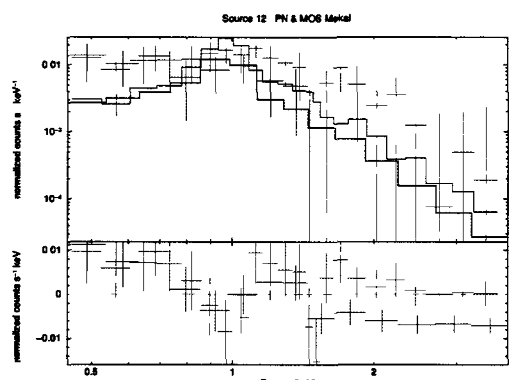

(c)

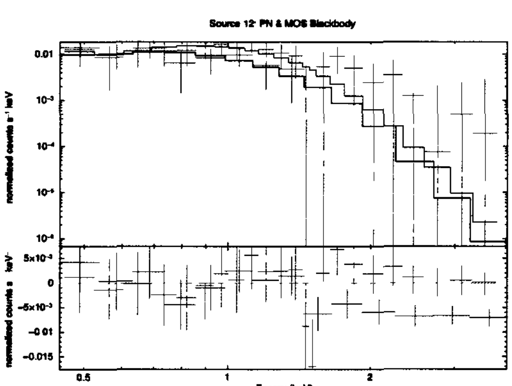

(d)

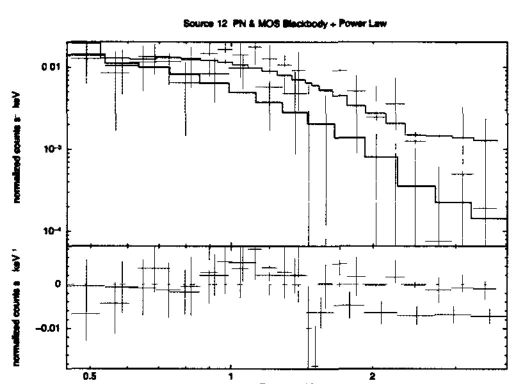

(e)

Figure C.16: **a)** pn and MOS spectrum of source 12 w/o models. **b)**Absorbed power law. **c)**Mekal. **d)**Blackbody. **e)**Blackbody + Power Law.

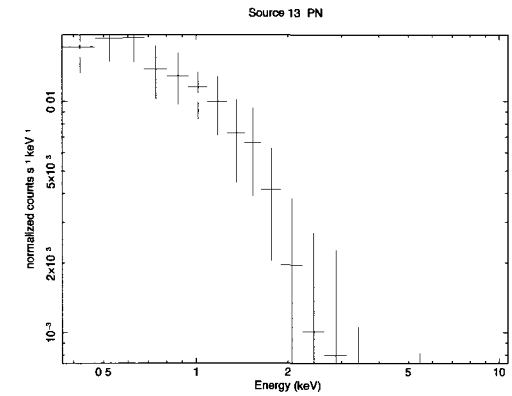

(a)

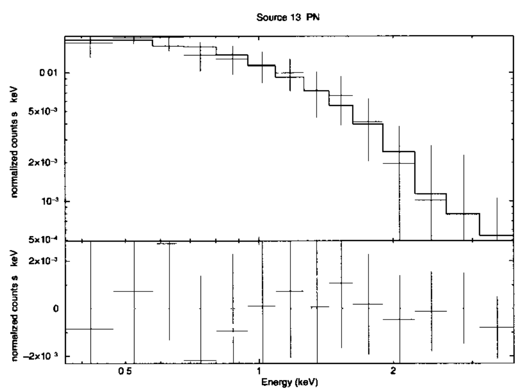

(b)

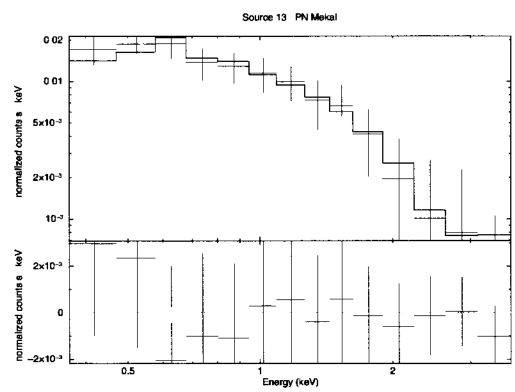

(c)

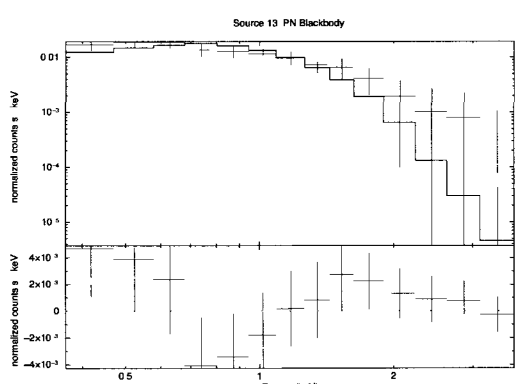

(d)

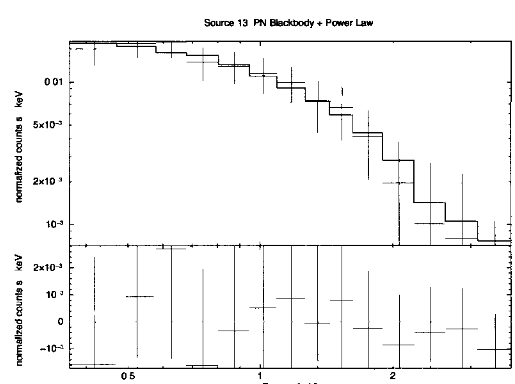

(e)

Figure C.17: **a)** pn spectrum of source 13 w/o models. **b)**Absorbed power law. **c)**Mekal. **d)**Blackbody. **e)**Blackbody + Power Law.

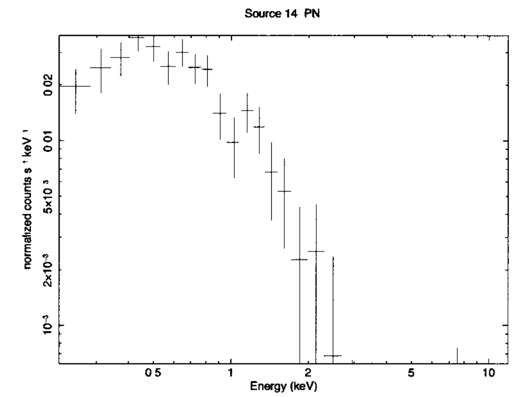

(a)

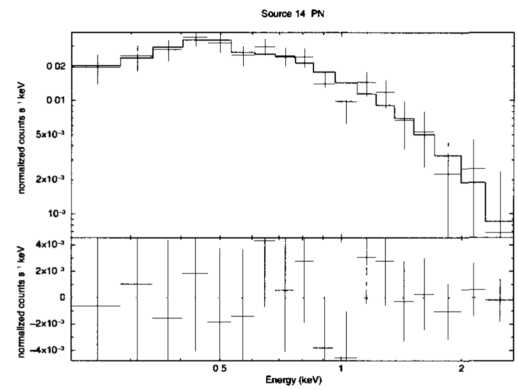

(b)

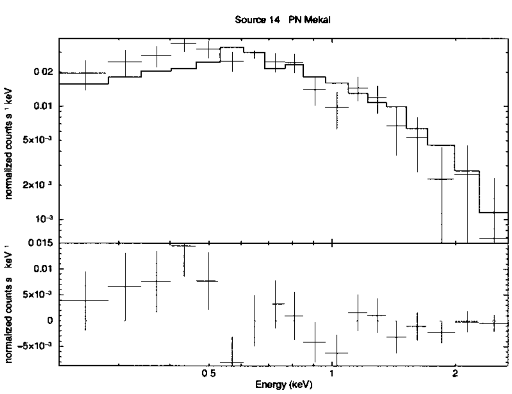

(c)

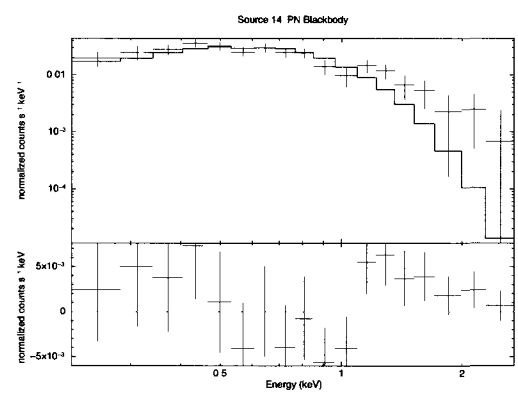

(d)

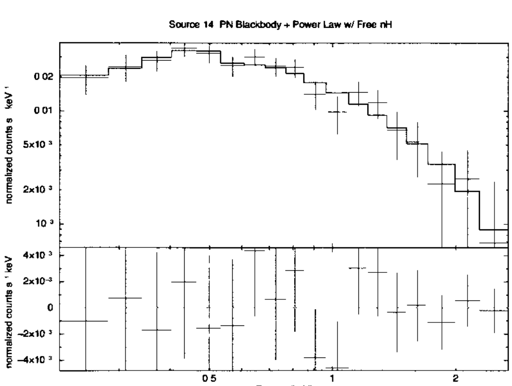

(e)

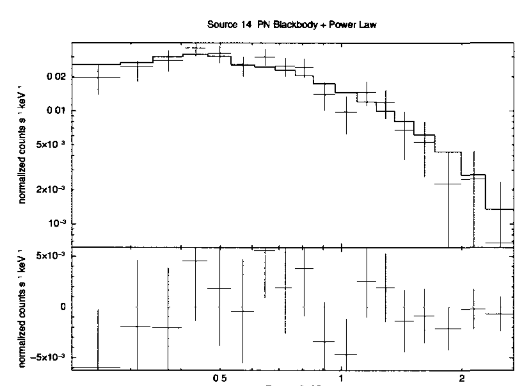

(f)

Figure C.18: **a)** pn spectrum of source 14 w/o models. **b)**Absorbed power law. **c)**Mekal. **d)**Blackbody. **e)**Blackbody when N_H is left as a free parameter. **f)**Blackbody + Power Law.

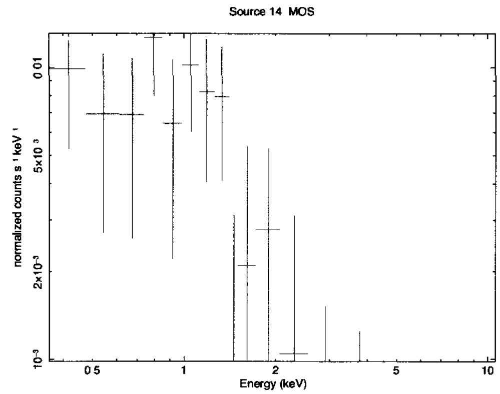

(a)

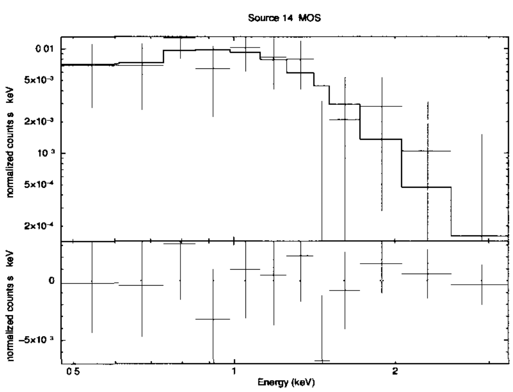

(b)

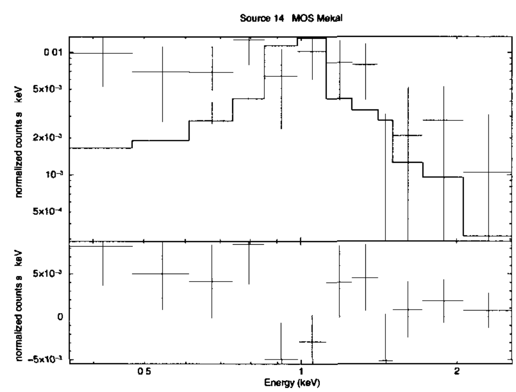

(c)

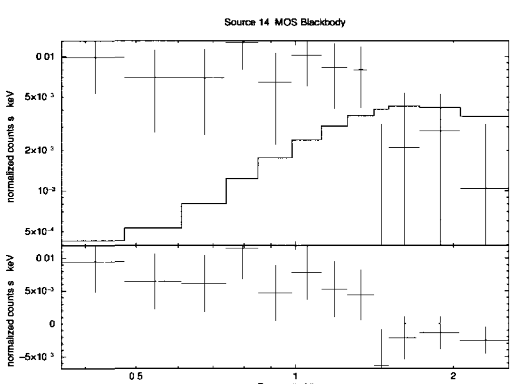

(d)

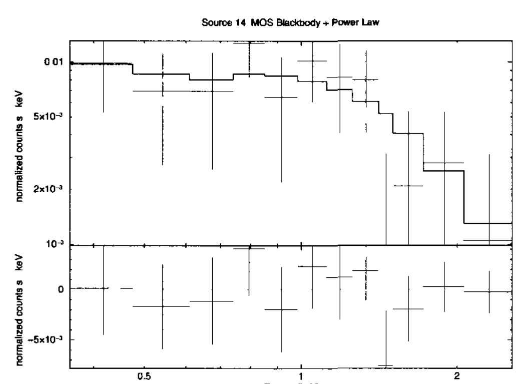

(e)

Figure C.19: **a)** pn spectrum of source 14 w/o models. **b)**Absorbed power law. **c)**Mekal. **d)**Blackbody. **e)**Blackbody + Power Law.

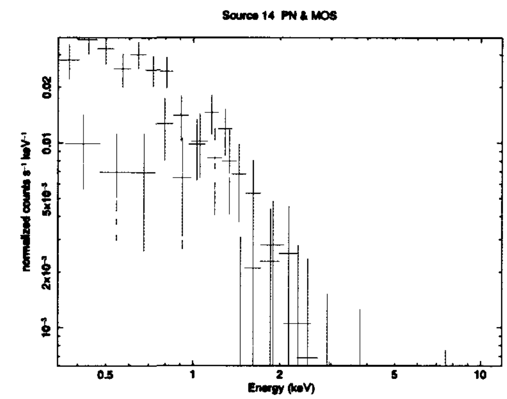

(a)

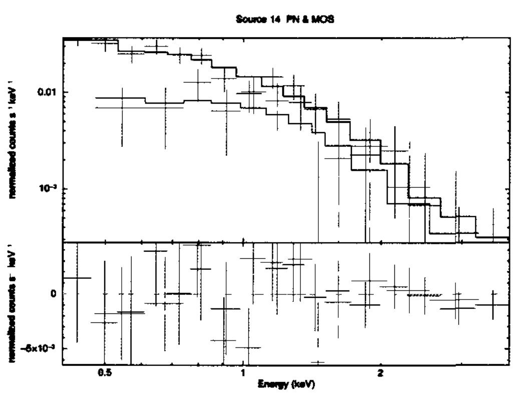

(b)

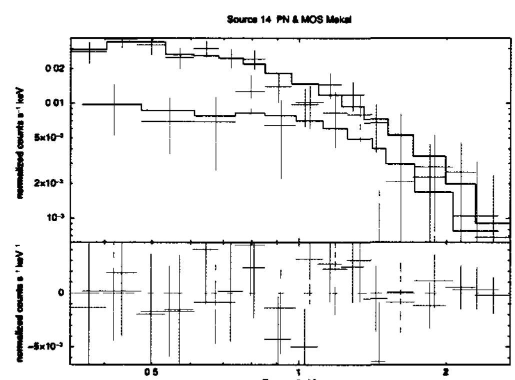

(c)

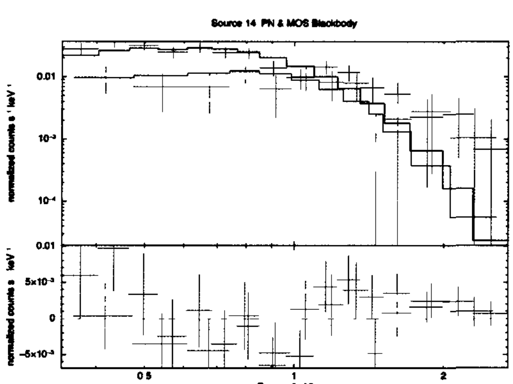

(d)

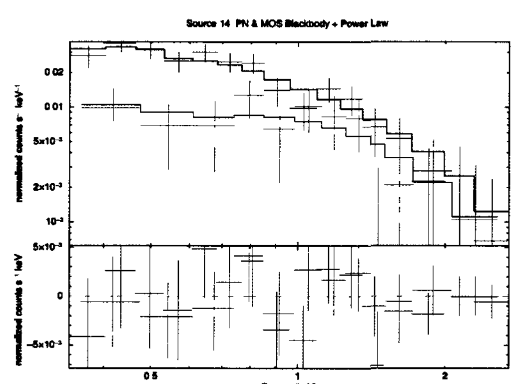

(e)

Figure C.20: **a)** pn spectrum of source 14 w/o models. **b)**Absorbed power law. **c)**Mekal. **d)**Blackbody. **e)**Blackbody + Power Law.

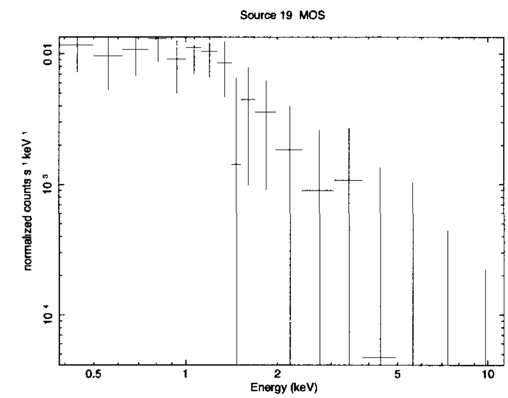

(a)

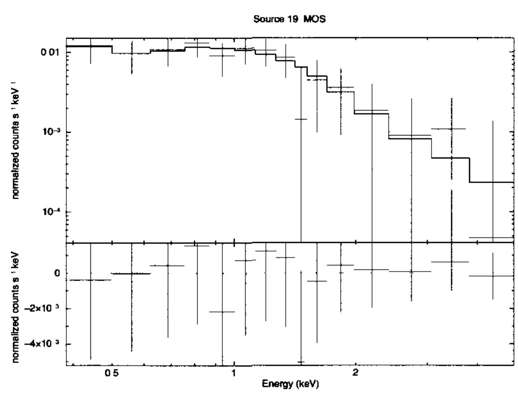

(b)

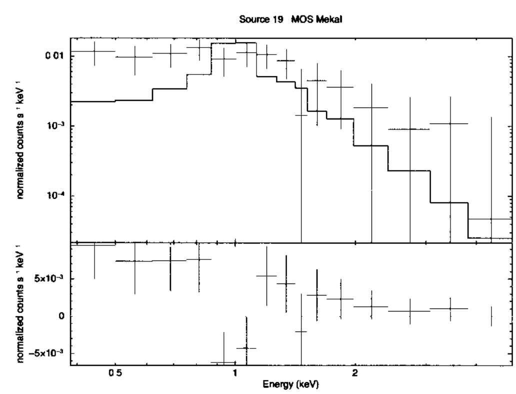

(c)

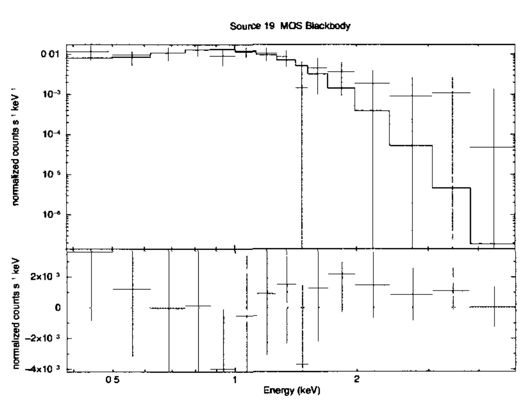

(d)

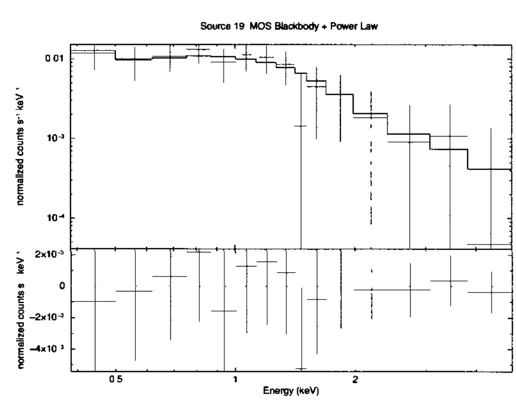

(e)

Figure C.21: **a)** pn spectrum of source 19 w/o models. **b)**Absorbed power law. **c)**Mekal. **d)**Blackbody. **e)**Blackbody + Power Law.

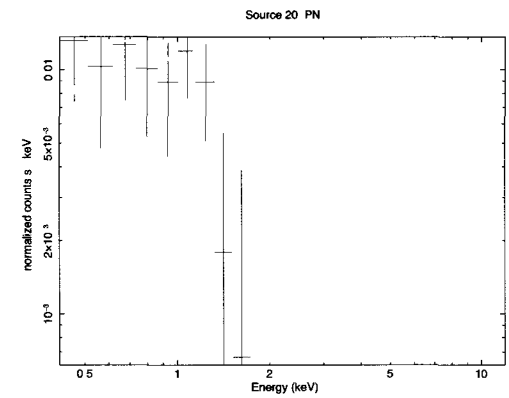

(a)

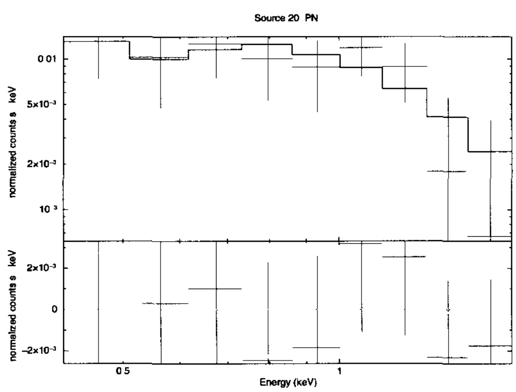

(b)

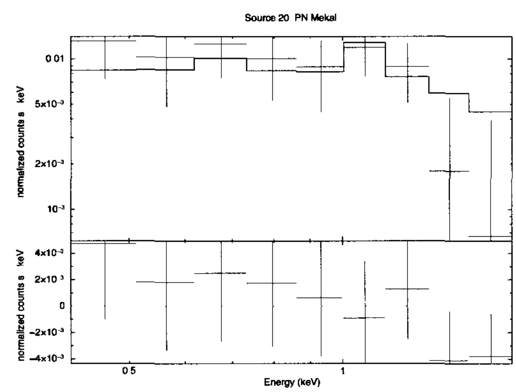

(c)

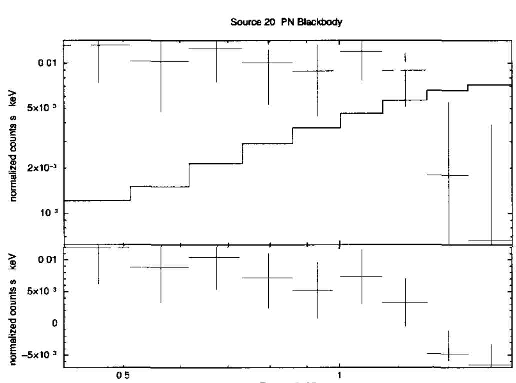

(d)

(e)

Figure C.22: **a)** pn spectrum of source 20 w/o models. **b)**Absorbed power law. **c)**Mekal. **d)**Blackbody. **e)**Blackbody + Power Law.

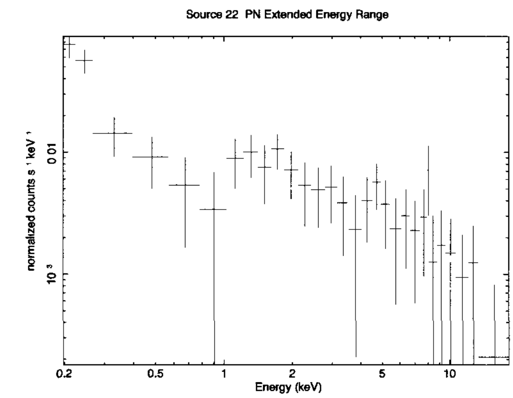

(a)

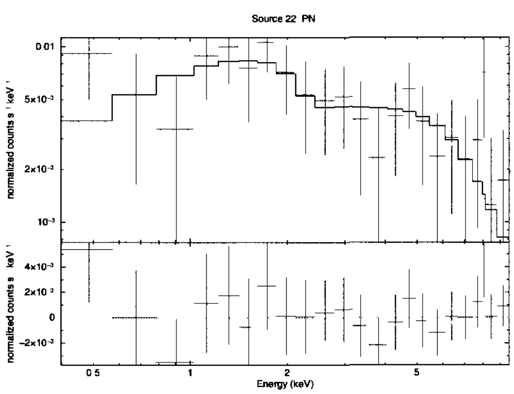

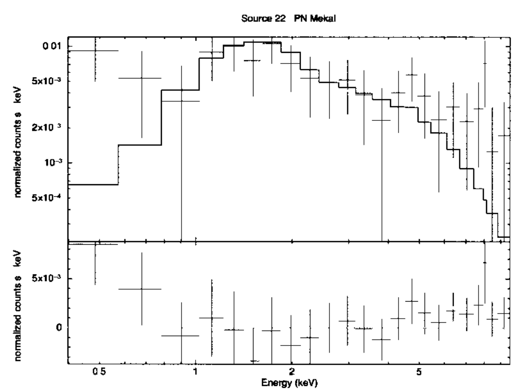

(b) (c)

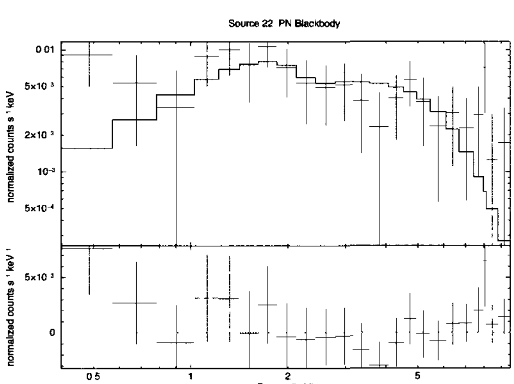

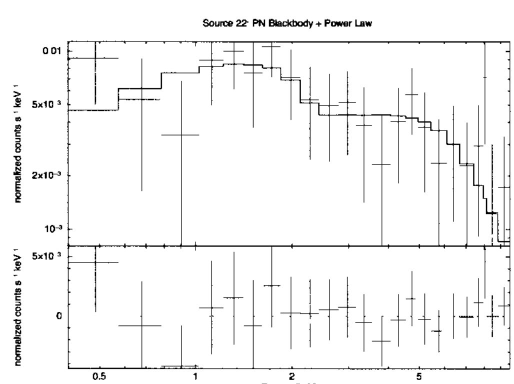

(d) (e)

Figure C.23: **a)** pn spectrum of source 22 w/o models with extended energy shown. **b)**Absorbed power law. **c)**Mekal. **d)**Blackbody. **e)**Blackbody + Power Law.

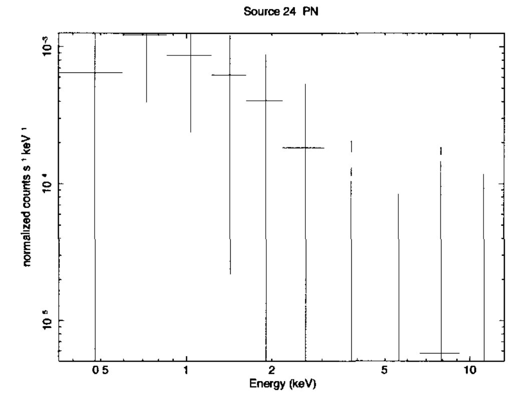

(a)

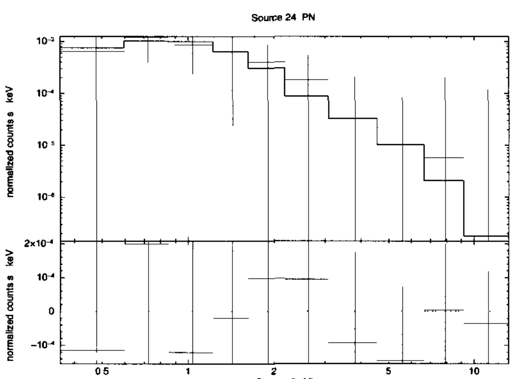

(b)

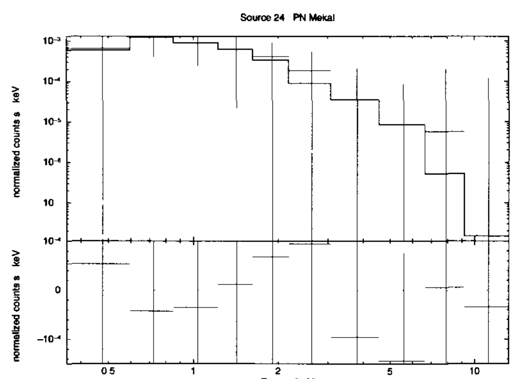

(c)

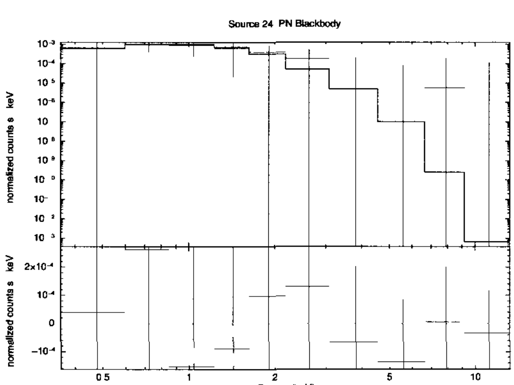

(d)

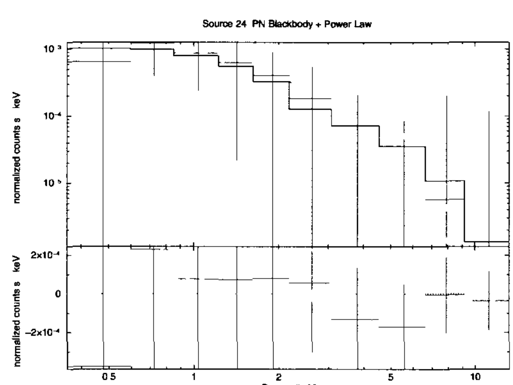

(e)

Figure C.24: **a)** pn spectrum of source 24 w/o models. **b)**Absorbed power law. **c)**Mekal. **d)**Blackbody. **e)**Blackbody + Power Law.

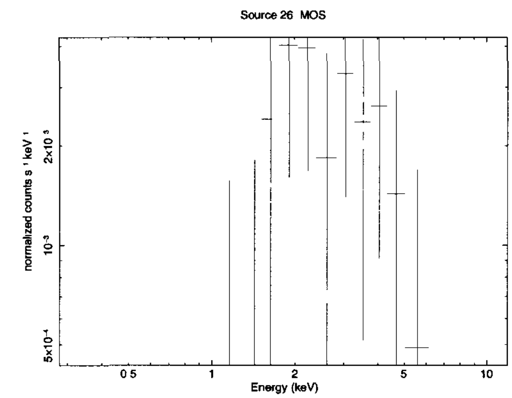

(a)

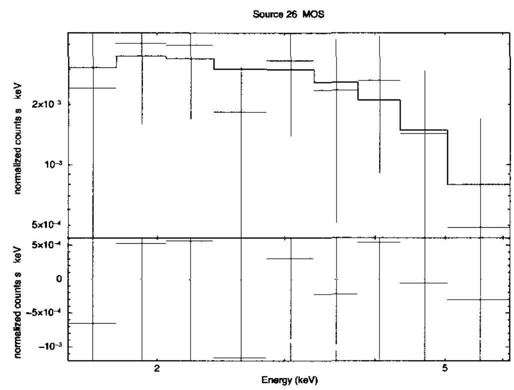

(b)

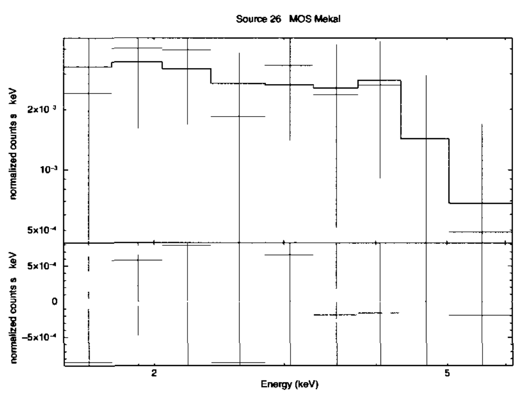

(c)

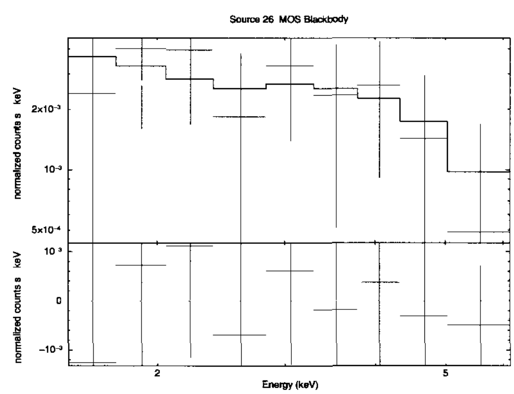

(d)

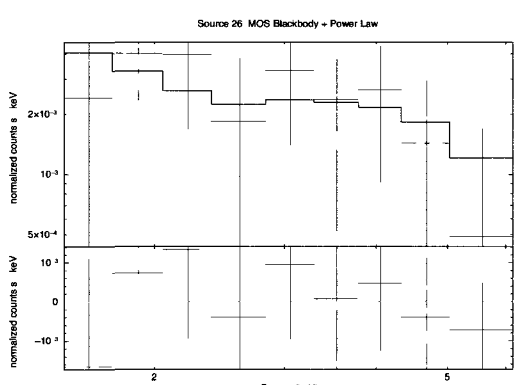

(e)

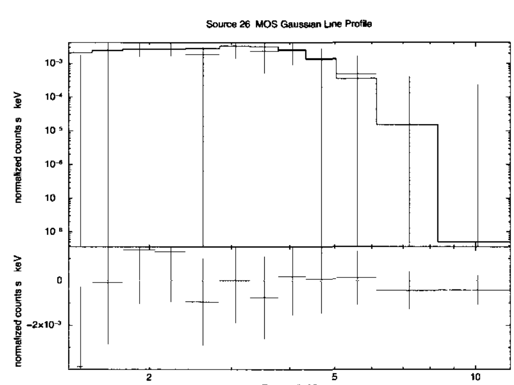

(f)

Figure C.25: **a)** pn spectrum of source 26 w/o models. **b)**Absorbed power law. **c)**Mekal. **d)**Blackbody. **e)**Blackbody + Power Law. **f)** Gaussian line profile.

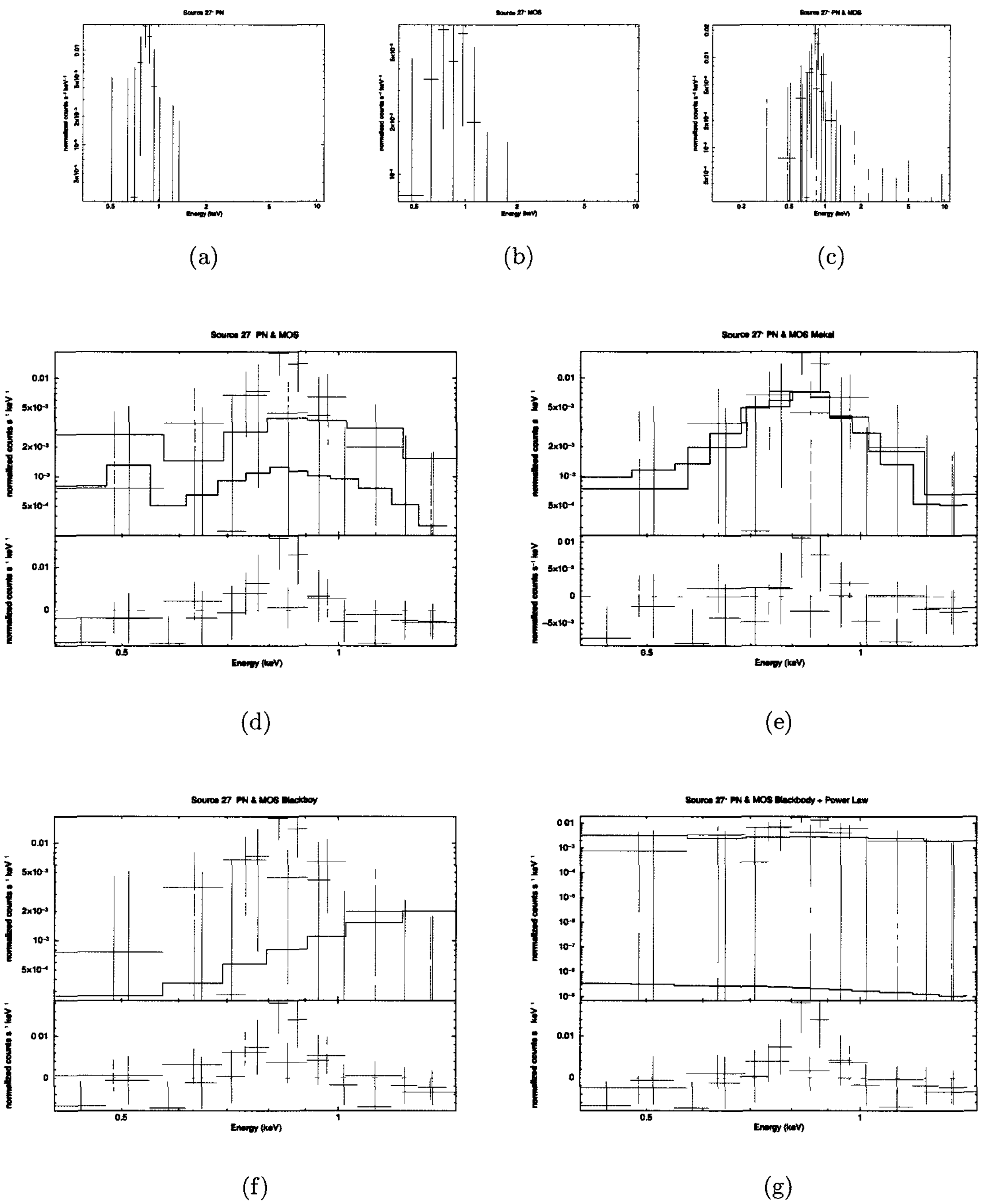

Figure C.26: **a)** pn spectrum of source 27 w/o models. **b)**pn spectrum of source 27 w/o models. **c)**Combined pn and MOS spectrum of source 27 w/o models.**d)**Absorbed power law. **e)**Mekal. **f)**Blackbody. **g)**Blackbody + Power Law.

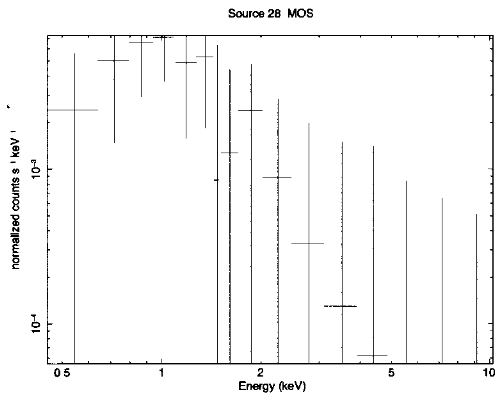

(a)

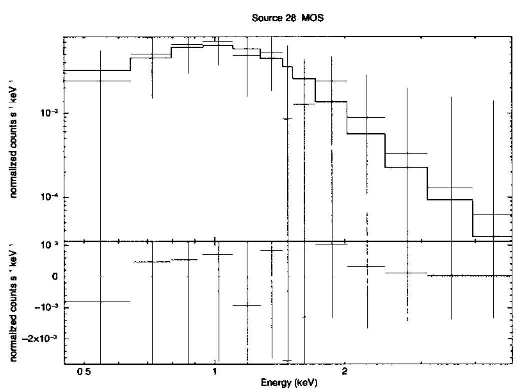

(b)

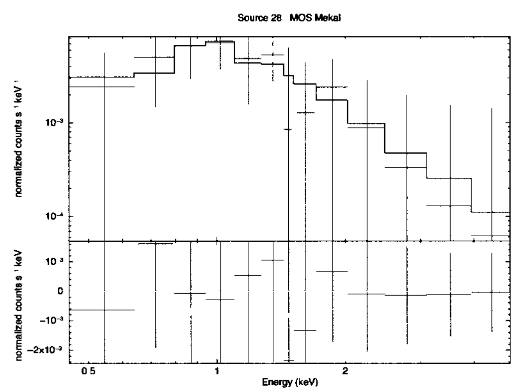

(c)

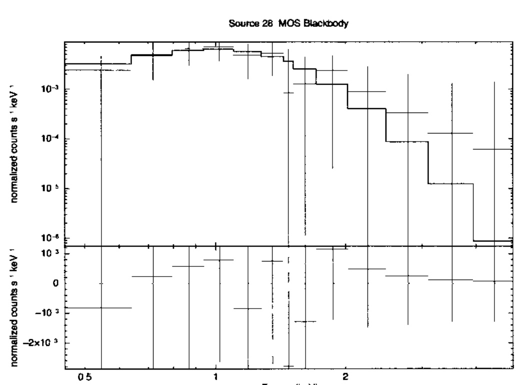

(d)

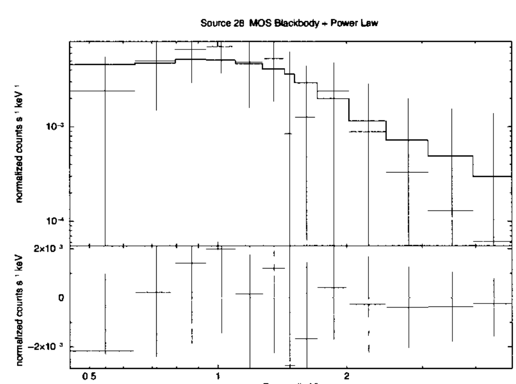

(e)

Figure C.27: **a)** pn spectrum of source 28 w/o models. **b)**Absorbed power law. **c)**Mekal. **d)**Blackbody. **e)**Blackbody + Power Law.

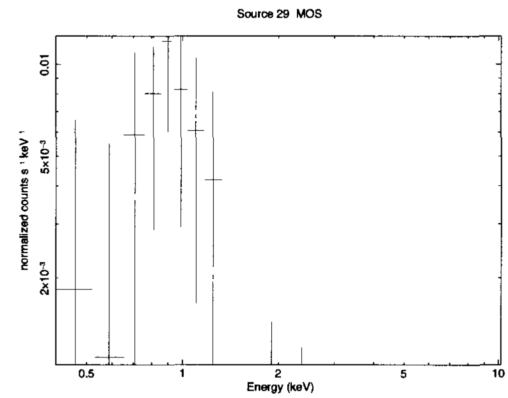

(a)

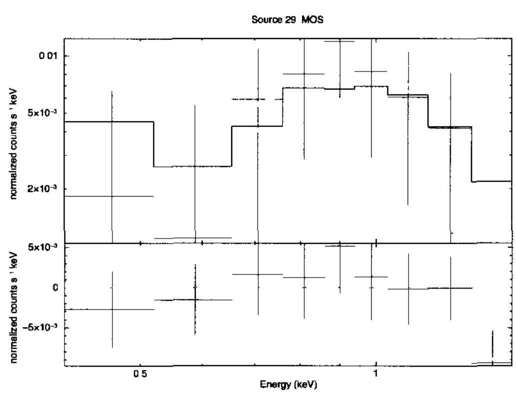

(b)

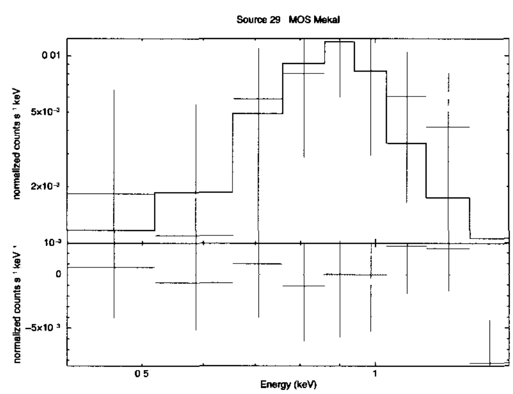

(c)

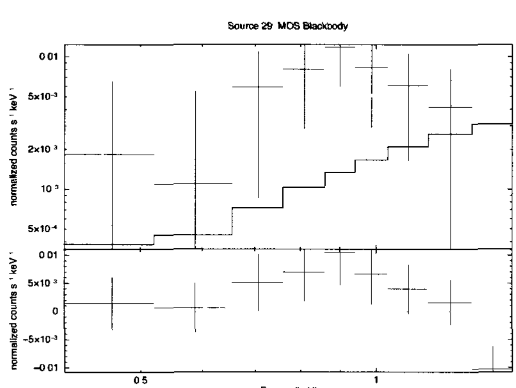

(d)

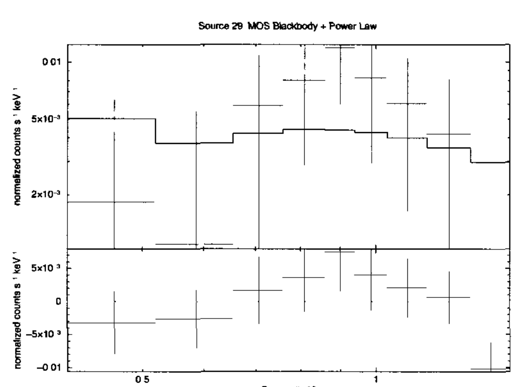

(e)

Figure C.28: **a)** pn spectrum of source 29 w/o models. **b)**Absorbed power law. **c)**Mekal. **d)**Blackbody. **e)**Blackbody + Power Law.

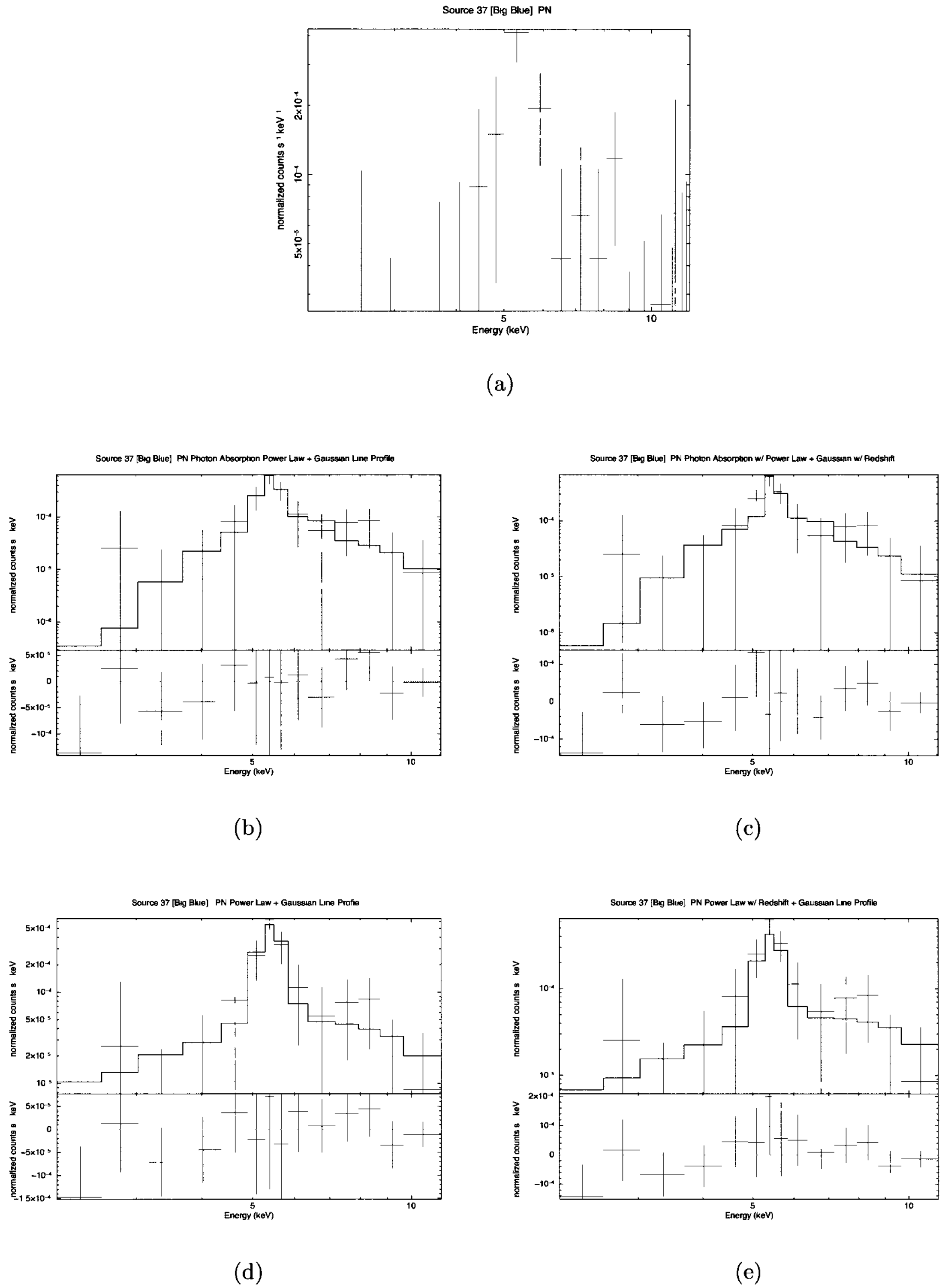

Figure C.29: **a)**pn spectrum of source 37 [Big Blue]. Model fits and residuals are shown for; **b)**Absorbed power law + Gaussian, **c)**Absorbed power law + Gaussian w/ redshift. **d)**Power law w/ redshift + Gaussian. **e)**Power law w/ redshift + Gaussian w/ redshift.

Appendix D

Acronyms

- AGN: Active Galactic Nuclei
- ARF: Ancillary Response File
- ASCA: Advanced Satellite for Cosmology and Astrophysics
- BLR: Broad Line Region
- CCD: Charged-Coupled Devices
- CCF: Current Calibration File
- CIF: Calibration index file
- CT: Compton Thick
- CTE: Charge Transfer Efficiency
- CTI: Charge Transfer Inefficiency
- CXRB: Cosmic X-ray Background
- EPIC: European Photon Imaging Camera
- ESA: European Space Agency
- FITS: Flexible Image Transport System
- FOV: field of view

- FWHM: Full Width Half Maximum
- GTI: Good Time Interval
- HEW: half energy width
- HMXB: High mass X-ray binary
- HR: hardness ratio
- LINER: Low-ionization nuclear emission line region
- MOS: Metal Oxide Semi-conductor CCD camera
- NLR: Narrow Line Region
- ODF: Observation Data Files
- OM: Optical Monitor
- OoT: Out-of-Time event
- PHA: Pulse Height Analyzer
- PI: Pulse-Invariant
- QE: Quantum Efficiency
- RGS: Reflection Grating Spectrometer
- RMF: Redistribution Matrix File
- SAS: Scientific Analysis System
- XMM: Multi-Mirror Mission
- XSA: XMM-Newton Science Archive